Skeletal-wide heterogeneity of cancellous bone and methods to assess *in vivo*

A Dissertation
SUBMITTED TO THE FACULTY OF THE
UNIVERSITY OF MINNESOTA
BY

Luke David Arentsen

IN PARTIAL FULFILMENT OF
THE REQUIREMENTS FOR THE DEGREE OF
DOCTOR OF PHILOSOPHY

[Adviser: Susanta Hui, PhD]

[June 2014]

Acknowledgments:

I would like to acknowledge my advisor, Susanta, who has spent countless hours teaching, guiding, and mentoring me to become more effective in the pursuit of science.

I would also like to thank members of Dr. Hui's laboratory, specifically Dr. Masashi Yagi and Dr. Yutaka Takahashi, for assisting with early morning analyses, late night experiments, and showing me the manifestation of passion for science.

I would also like to thank the participants of the clinical trials and imaging experiments for donating their time and bodies to further knowledge in this field.

I would finally like to thank my brothers and sister, Andrew, Timothy, and Melinda, for their constant assistance, encouragement, and counsel.

Dedication:

This dissertation is dedicated to Nicole, Lillian, Caleb, and my parents.

Table of Contents

List of Figures viii

List of Tables xiii

Chapter 1: Introduction 1

1.1. Rational for skeletal heterogeneity 2

1.2. Methods of assessment for murine and human skeleton 3

1.3. Importance of marrow fat assessment 6

1.4. Outline of this document 9

1.5. Scientific output in this dissertation 11

1.5.1. Journal Publications 11

1.5.2. Conference Presentations 12

Chapter 2: Characterization of micro-CT for the murine model and use on localized and whole-body imaging 16

2.1. Introduction 16

2.1.1. Motivation for whole-body imaging using micro-CT 16

2.1.2. Rationale for the characterization of rotating gantry micro-CT for *in vivo* imaging 17

2.2. Methods 20

2.2.1. Beam Geometry 23

2.2.2. Beam Energy 24

2.2.3. Localized *In Vivo* imaging 25

2.2.4. Methodology for whole-body imaging 28

2.2.4.1. Visualization 29

2.3. Results 32

2.3.1. Beam Geometry 32

2.3.2. Beam Energy 32

2.3.3. Localized *In Vivo* Model 34

2.3.4. Whole body imaging findings 36

2.4. Discussion 40

2.4.1. Localized *in vivo* 40

2.4.2. Whole-body imaging 42

2.4.3. Translation significance 43

2.4.4. Conclusion 44

2.5. Further direction 45

Chapter 3: Cancer therapy causes rapid and heterogeneous expansion of marrow fat and decreased bone mineral density 46

3.1. Introduction 46

3.2. Methods 48

3.2.1. Subjects 48

3.2.2. DECT and MR Imaging 49

3.2.3. Statistics 52

3.3. Results 53

3.4. Discussion 63

3.4.1. Conclusions 65

Chapter 4: Validation of Marrow fat assessment using noninvasive imaging with histologic examination of human bone samples 66

4.1. Introduction 66

4.2. Method and Materials 67

4.2.1. Subjects 67

4.2.2. Imaging 67

4.2.3. Excision, registration technique 68

4.2.4. Histology image tile procedure 70

4.3. Results 71

4.4. Discussion 72

4.4.1. Clinical implications 74

4.4.2. Limitations 74

4.4.3. Conclusion 75

Chapter 5: *In situ* assessment reveals skeletal-wide heterogeneity of human cancellous bone 76

5.1. Introduction 76

5.2. Methods 77

5.2.1. Subjects 77

5.2.2. Imaging 78

5.2.3. ROI analysis 79

5.2.4. Basis Material Composition 80

5.2.5. Statistics 81

5.3. Results 82

5.4. Discussion 86

5.4.1. Limitations 89

5.4.2. Bone Mineral Density Heterogeneity Index Model 89

5.4.3. Conclusion 93

Chapter 6: Conclusion 95

6.1. Summary and general conclusions 95

6.2. Potential applications 97

6.2.1. Murine Study 97

6.2.2. Human Study 98

Bibliography 100

7. Appendix 108

7.1. Further investigation into functional heterogeneity using Dual Isotope micro-PET/CT 108

7.2. Methods and Materials 109

7.3. Results 112

7.4. Discussion 117

7.5. Conclusions 119

LIST OF FIGURES

Figure 1-1. Representative images from clinical whole body scanners. A. DXA scan - notice 2D image superimposes sternum, ribs, and digestion organs over vertebral column. Subject is also post left hip replacement. B. CT scan – 3D imaging allows individual analysis of each skeletal site as well as separation of cancellous bone from cortical bone. 5

Figure 1-2. Diagrammatic representation of distribution of red and yellow marrow from birth to age 25 years. Taken from Kricun et al. [16]. 7

Figure 1-3. Difference in CT# for identical material using dual energy. 8

Figure 2-1. Phantom 1: 3D reconstruction of density phantom with 6 densities: 1.750 g/cm^3, 1.250 g/cm^3, 1.050 g/cm^3, 1.000 g/cm^3, and two air-equivalent densities. The surrounding Lucite material has a density of 1.040 g/cc. 22

Figure 2-2. Comparison of a region-of-interest of the 1000th slice. (Left) Original image (Center) Global Renyi Entropy (GREP) (Right) ALREP method. Note that the GREP method resulted in over-segmentation (shown by arrows), causing fine gaps (marrow) to be either filled in comparison to the original image. 30

Figure 2-3. Reconstruction of whole body mouse image acquisition. First visualization of high resolution (Isotropic pixel size = 9.19µm; > 6,300 slices) micro-CT dataset. 31

Figure 2-4. Difference in HU of Phantom 1 with change in Energy. Notice at lower energies the difference between low and high densities is greater. 33

Figure 2-5. Filtration effect for different densities. All curves produced with 80 kVp energy except for labeled 40 kVp. Notice as filtration thickness increases, discernment between water and 1.750 g/cm^3 density decreases. HU values for 1.750 g/cm^3 using 40 kVp remain relatively constant as thickness increases; however, exposure time increases. 34

Figure 2-6. Effect of isotropic pixel size on image clarity. All images were taken perpendicular to the femoral axis at 0.5mm from the growth plate using Siemens Inveon MicroCT. A. 9.19 µm, B. 18.39 µm, C. 36.78 µm, and D. 95.39 µm. Notice increased noise in A. but gross loss of detail with C and D. 35

Figure 2-7 Average value of the bone mineral density in mg/cc from the segmented region determined using ALREP and manual method. The ALREP method results are labeled as 15-1 ALREP, 15-4 ALREP and 15-5 ALREP and the data points are connected by

lines. The manual segmentation results are labeled as 15-1 manual, 15-4 manual and 15-5 manual and the data points are shown with markers. 37

Figure 2-8 Average and standard deviation plot of BMD obtained using ALREP. The average and the standard deviation are calculated across the three datasets. The centerline is the average BMD and the standard deviation flanks either side of the average. 39

Figure 2-9 Calibration curve for BMD. The HU of a phantom containing inserts for which the value of electron density was known was imaged and the curve was plotted. A straight line fit was then performed on the data points. The equation of the fitted line and its regression is shown in the plot. 39

Figure 2-10. When magnification decreases or binning increases, the spatial resolution will decrease. The dotted line represents a resolution threshold above which have been used to image trabecular bone in murine model [60, 61]. Magnification: High (3.3x), Medium (1.8x), Low (1.3x) 41

Figure 3-1. Dual energy spectrum used in Siemens SOMATOM ® dual source computed tomography scanner. The difference in energy can be utilized to identify material through basis material decomposition. Image taken from Johnson et al. [69]. 51

Figure 3-2. Correlation between DECT and WF-MRI marrow fat (MF) at L3, L4 and L5. A) A high correlation (r=0.77, 95% CI: 0.69, 0.83) in MF measurements (includes L3, L4, and L5) between the two imaging modalities was observed at baseline (triangle), 6 (circle) and 12 months (star) post treatment. B) Measurements of absolute change in MF from baseline to 12 months were highly correlated between the two imaging methods (r= 0.91, 95% CI: 0.84, 0.95). 55

Figure 3-3. Region Effects on marrow fat or MF measured by DECT (A) and MRI (B). The colored region of each boxplot represents the 1st and 3rd quartile range of observations, with a black line at the median. Whisker lines are placed at the 1.5 interquartile range of the lower and upper quartile and outliers are noted with open circles. A. DECT: Regions differed in mean MF at baseline. L3 and L4 were equivalent, and L5 was lower by 4% ($p<0.001$) and FN higher by 13% ($p<0.001$) relative to L3 and L4. MF increased over time at all sites measured ($p<0.001$), with an estimated mean change of 7% from baseline to 12 months for all regions. The degree of change in MF was similar among the four regions ($p=0.27$). B. MRI: Regions differed in mean MF at baseline. L3 and L4 were equivalent, L5 was higher by 5%, and FN was higher by 32% ($p<0.001$). MF increased over time at all sites measured ($p<0.002$), with an estimated mean change of 15% from baseline to 12 months for L3-L5. In contrast to DECT, the increase in FN MF was approximately half the increase of L3-L5 ($p=0.025$). 56

Figure 3-4. Absolute Percent Change in L4 and L5 Marrow Fat by Treatment. A & B: Based on dual energy computed tomography (DECT) imaging in 15 subjects from 0 to 12 months, L4 MF increased by 9% after radiation, 9% after chemotherapy, and 4% after oophorectomy ($p<0.032$). The increase in MF was larger for chemotherapy and radiation relative to oophorectomy (interaction $p=0.004$). From 0 to 12 months, L5 MF increased by 17% with radiation, 8% with chemotherapy and 4% with oophorectomy ($p<0.032$). The change varied based on treatment (time x treatment interaction $p<0.001$). C & D: By water- fat MRI imaging, L4 and L5 MF increased from 0 to 12 months. The change varied based on treatment (time x treatment interaction $p<0.001$). L4 MF increased by 19% after radiation, by 24% after chemotherapy, and by 6% after oophorectomy. Likewise, L5 MF by WF-MRI increased from 0 to 12 months. L5 MF increased by 32% after radiation, by 18% after chemotherapy, and by 6% after oophorectomy. 58

Figure 3-5. Marrow fat mapping of a representative patient using DECT and water-fatMRI. Spine marrow fat mapping: Longitudinal changes in marrow fat distribution in spine due to chemotherapy for a representative subject at a) baseline, B) 6 months and C) 12 months after treatment using DECT (top figure) and water-fat MRI (bottom figure). Changes in MF were visible within 6 months of treatment, and continued to increase at 12 months. 59

Figure 3-6. BMD changes measured by different techniques. A. DECT mcBMD by skeletal regions and time: Regions differed in mean mcBMD at baseline ($p<0.001$); L4 was higher by 12 mg/cm^3 and L5 by 25 mg/cm^3 relative to L3. mcBMD in all regions decreased over time ($p<0.02$), and change varied by region (time x region interaction $p=0.03$).The 12 month decrease in mcBMD was 7 mg/cm^3 at L3, 14 mg/cm^3 at L4, and 13 mg/cm^3 at L5. B. DECT mcBMD by treatment (at L4) and time: Mean mcBMD measured by DECT at L4 did not vary at baseline based on treatment ($p=0.42$). Chemotherapy decreased mcBMD by 23 mg/cm^3 ($p=0.01$) from 0 to 12 months. Radiation decreased mcBMD by 10 mg/cm^3 ($p=0.09$) from 0 to 12 months, and was lowest at 6 months. Oophorectomy decreased mcBMD by 8 mg/cm^3 from 0 to 12 months ($p=0.24$) and was lowest at 6 months. 60

Figure 3-7. Correlation of MF and mcBMD at L4 from different modalities measuring the same patient. The panel on the left shows absolute measurements at baseline. The panel on the right shows changes from baseline to 12 months. 62

Figure 4-1. Multi-Modality Co-registration between histologic examination and *in vivo* imaging. Two vertebral bodies analyzed: top row is representative case of lower marrow fat and bottom row is higher marrow fat. A. & B. axial section of whole vertebral body with H&E staining. Void spaces of adipocytes were contoured by threshold and artifacts were removed at the discretion of the investigator. C. & D. water-fat MRI images of lumbar vertebrae and example of ROI placement. E. & F. DECT

images reconstructed to highlight marrow fat intensities. For imaging modalities, red represents high marrow fat concentration. 69

Figure 4-2. Marrow fat estimation from histology and *in vivo* imaging modalities. A) 17 vertebral bodies were imaged with DECT and MRI and then processed for H&E examination. Results of the imaging are compared with histologic adipocyte volume per tissue volume. B) Correlation between the marrow fat estimation results from two non-invasive imaging techniques. 73

Figure 5-1. 23 Regions of Interest representing areas of analyzed cancellous bone with representative case for ROI Placement of L3 80

Figure 5-2. Cancellous Bone Mineral Density distribution for 23 skeletal sites (skull separately). 83

Figure 5-3. Average correlation between representative skeletal sites for marrow-corrected BMD. 84

Figure 5-4. Mean correlation in mcBMD between 23 skeletal sites. Correlation coefficient was calculated for the mcBMD of each individual site vs the 22 other sites. Averages for control subjects vs cancer subjects are compared. 85

Figure 5-5. The heterogeneity index is presented for each of 22 skeletal sites (excluding the skull). Results are the average marrow corrected bone mineral density values from ten control subjects. Interestingly, heterogeneity was similar in adjacent bones. Additionally, there was greater heterogeneity in the superior versus inferior (cervical versus lumbar) spine. Heterogeneity was also higher toward the skull and feet, and lower in the mid-body. 90

Figure 5-6. Prediction of marrow-corrected cancellous Bone Mineral Density (mcBMD) values from a single measured value. A) Application of the skeletal-wide estimated density distribution (SEDD) model. Using the relationship between the average cancellous mcBMDs from all clinical sites of control subjects, a model was developed to estimate mcBMD for the entire skeleton from just one site. All values were corrected for age and marrow composition. If given a measured (known mcBMD) value of any test site (Known location), mcBMD values of 22 skeletal sites can be estimated. B) 10 cancer-treated donors were imaged with whole-body DECT using the SEDD model. The measured mcBMD value of the L1 from 10 cancer treated donors was used to estimate the 21 other skeletal sites. Mean predicted (95% confidence level) and measured values (SD) are shown. Only the T2 and L1 had significant differences between measured and estimated mcBMD ($p < 0.1$, t-test). A high correlation was seen between the average predicted and measured values for the donors ($r = 0.95$). 92

Figure 7-1 (A) Shielding designed to deliver radiation to the hind limbs. (B) Schematic of the experimental design. Micro-PET/CT acquisition was performed serially with FDG and NaF before and after the radiation to the same mice. Mice were dissected on day 3 after the radiation. 110

Figure 7-2. FDG uptake before(A) and after radiation(B). NaF uptake before radiation(C) and after radiation(D). Constant maximum and minimum intensities are set in the images for each tracer. (E) FDG uptake before (blue bars, $p<0.0001$) and after (red bars, $p=0.0002$) radiation is significantly different among bone regions. (F) NaF uptake before (blue bars, $p<0.0001$) and after (red bars, $p=0.0003$) radiation is significantly different. Star(*) indicates irradiated bony region. 113

LIST OF TABLES

Table 2-1. Table of experimental parameters. Phantom 1: Density-equivalent material; Phantom 2: 7mL Water and 7mL Butanol tubes; and Phantom 3: A micro-CT wire phantom. All scans performed with manufacture-recommended calibrations. Exposure times are determined by peak within 75-85% CCD range……..18

Table 2-2. Results of four magnification and binning combinations. 10% MTF Spatial Resolution (lp/mm), Bone Mineral Density (BMD) estimation, Bone Volume to Total Volume ratio (BV/TV), Signal-to-Noise Ratio (SNR), and Edge definition indicate optimal setup at 3.3x magnification with a binning of 2 (18.39 µm isotropic pixel size). Sharpness describes ability to separate cancellous and cortical bone compartments by qualitative assessment. …… 26

Table 2-3 Comparing ALREP and manual method. 40

Table 3-1. Demographic Characteristics of Subjects. Data are summarized using the mean ± standard deviation. Chemotherapy was the principal treatment modality for ovarian cancer, radiation therapy was primarily used to treat endometrial cancer, and oophorectomy was performed in early stage ovarian and endometrial cancer patients who did not require subsequent radiation or chemotherapy. 54

Table 7-1. Estimated change due to radiation. FDG averaged over all regions is expected to decrease to 50% of its pre-radiation level. This effect varied by region, and was particularly low for the tibia, where post-radiation FDG was 32% of its pre-radiation level. The NaF level averaged over all regions is expected to increase by a factor of 2.2 following radiation. However, this increase varied by region, from a factor of 1.9 in the skull and mandible to a factor of 2.4 in the femur and tibia. The wide confidence intervals are the result of variable effects seen in different mice (see 7-3 C). 116

CHAPTER 1: **INTRODUCTION**

Fractures are the most common and most expensive of nonfatal fall-related injuries. According to the Center for Disease Control, the economic burden placed on the 2012 American healthcare system by fractures was $18.8 billion and is expected to increase to over $40 billion by 2020 [1]. Although women account for only 58% of individuals older than 65, they are 2.3 times more likely to experience a fracture and treatment is 2.8 times more expensive than men [2]. Interventions that can identify potential fractures will significantly reduce health care costs and improve quality of life for the increasing number of elderly individuals.

Osteoporosis is a skeletal disorder that results with a weakening of bones and increases the risk of fracture [3, 4]. The most common method of diagnosing osteoporosis is by measuring the bone mineral density (BMD) of a few critical skeletal sites, (i.e. femoral neck, distal radius, and 4 lumbar vertebra). A dual-energy x-ray absorptiometry (DXA) test is widely used to derive the areal BMD of individual skeletal sites and compare those values to the ideal BMD of a healthy 30-year-old adult. A diagnosis of osteoporosis is given if the BMD of any site is less than 2.5 standard deviations from this norm [5].

However, skeletal sites throughout the body have different rates of bone turnover causing some to decrease faster than others [6]. For decades, authors have theorized that the rate of bone mineral remodeling was determined by the proportion of surface area to bone volume present in each bone [7, 8]. Therefore, a sudden bone

afflicting stimulus would affect the cancellous BMD prior to the cortical bone. It is in these highly cancellous bone regions where fracture risk could be expected to occur. Therefore, a diagnosis of osteoporosis at one site may not correlate to another site. For example, Kanis et al. noted that in a 100 subject group, 14% were given a diagnosis of osteoporosis at either the distal radius or lumbar spine while only 3% were seen with a diagnosis at both sites [9].

1.1. Rational for skeletal heterogeneity

There are 206 bones in the average adult skeleton and each bone is unique in terms of function, structure, and composition. The minerals that constitute the osseous tissue of these bones are continually being remodeled; however, the rate at which different sites remodel may vary throughout the skeleton. Bergmann et al. attempted to assess the heterogeneity of skeletal-wide bone remodeling by measuring the concentrations of Calcium-47 throughout the whole body [10]. However, they were unable to separate adjacent skeletal regions due to technical limitations. Although some studies have suspected skeletal-wide inhomogeneity, none have separated cortical from cancellous BMD.

A suggested cause of differences in bone remodeling between skeletal sites was recently explained as an 'epigenetic postcode' [11]. This genetic sequence enables cells to retain their origin and/or body positioning information, which permits separate bone cell populations to be regulated autonomously. While the study only investigated

epigenetic postcode from two specific sites, it suggests an epigenetic postcode exists for each bone. If different skeletal sites remodel differently based on an epigenetic postcode, then measuring the cancellous tissue through bone mineral density (BMD) should be able to show the differences throughout the body.

In order to understand the range and depth of skeletal heterogeneity and the effects of cancer treatment, it is necessary to utilize different models of capturing natural bone heterogeneity. Several methods of assessment are needed which have been not been developed previously. By developing these modalities, we provide means to assess skeletal-wide heterogeneity in terms of bone mineral density, trabecular bone matrix characteristics, and bone marrow content. Pre-clinical models allow us to study mammals in a controlled environment while mimicking treatment effects and investigating responses longitudinally. With clinical trials, we can verify pre-clinical results and draw conclusions regarding treatment intervention and the impact on skeletal heterogeneity.

1.2. Methods of assessment for murine and human skeleton

Recent technological advancements in *in vivo* imaging for the pre-clinical model has made longitudinal studies of the murine skeleton possible. For this work we used the Siemens Inveon® PET/CT. Although this is a commercially available machine, there have been few publications on its utility or characterization. Therefore, work needed to

be done to identify strengths of the machine as well as find optimal configurations for our longitudinal studies with the mouse model.

As mentioned above, DXA is the most common modality used for assessing bone health in the general human population. However, it has several limitations which make DXA's use over the whole body inaccurate and misrepresentative. First, DXA calculates the areal BMD of individual skeletal sites using two dimensional imaging, see Figure 1-1a. Two dimensional imaging cannot separate skeletal sites that overlap each other or extra osseous tissue. Therefore, bones of the thoracic spine may overlap with the sternum or ribs or contents in the digestive system. Second, it superimposes the dense outer cortical bone and the porous internal cancellous bone. This can mask the true condition of cancellous bone. Finally, marrow composition can vary the density of the whole bone from site to site causing differences between bones. Therefore, a technique is needed that can separate cortical bone from cancellous bone throughout the whole skeleton. Although conventional (i.e. single-energy) computed tomography (CT) (Figure 1-1b) can produce 3D images, it cannot differentiate different bone marrow compositions.

However, current methods of quantifying marrow fat (e.g. transiliac biopsy) are inaccurate, invasive, and not-repeatable or, as previously mentioned, and use MRI which is expensive and has limited availability. Therefore, it would be optimal to employ a technique that could utilize CT modalities, which are already commonly employed in cancer treatment centers, to monitor bone marrow health.

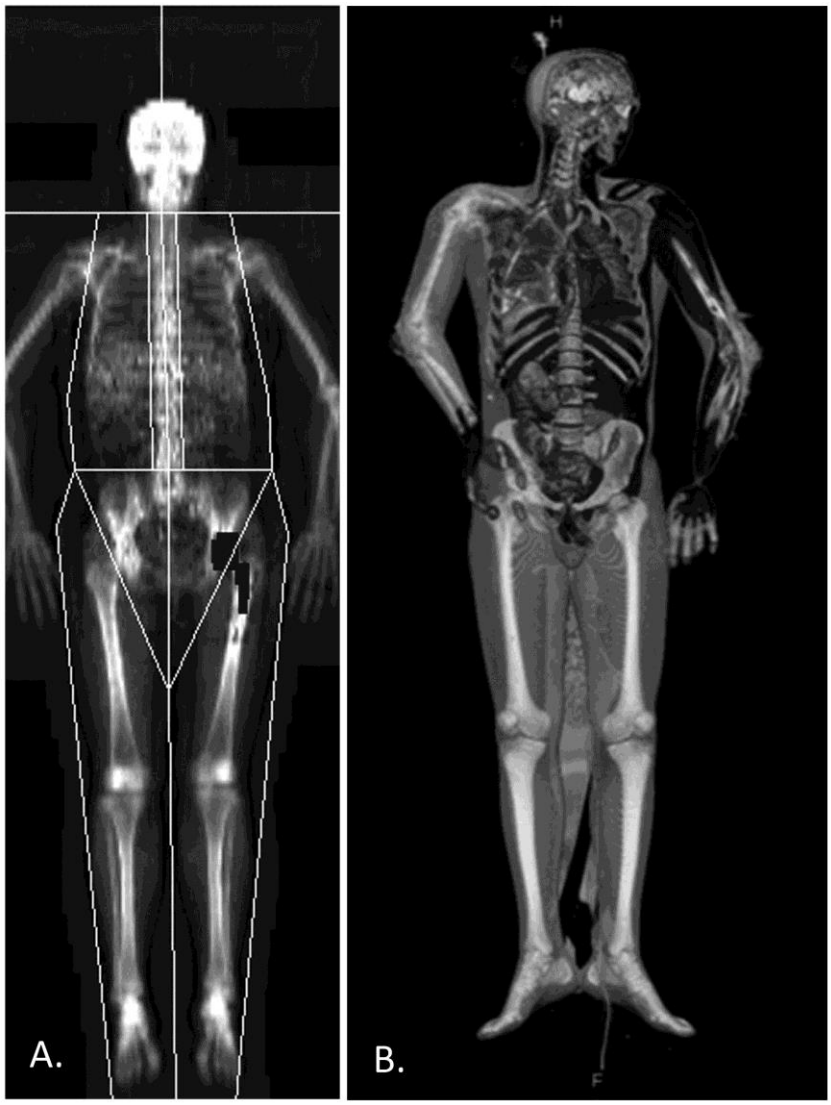

Figure 1-1. Representative images from clinical whole body scanners. A. DXA scan - notice 2D image superimposes sternum, ribs, and digestion organs over vertebral column. Subject is also post left hip replacement. B. CT scan – 3D imaging allows individual analysis of each skeletal site as well as separation of cancellous bone from cortical bone.

Water-fat MRI (wfMRI) could also measure volumetric marrow composition [12].

However, MRI use is limited in cancer patients after diagnosis, perhaps due to its high

cost and/or limited availability in some locations. Newly developed technology has reduced the radiation dose to patients and improved imaging quality of DECT [13]. Thus, DECT is frequently performed to diagnose and monitor cancer.

However, DECT has never been used to assess the entire mammal skeleton, much less that of a human. If the entire body can be imaged volumetrically and corrected for marrow content, it would be possible to quantify accurate BMD for all skeletal sites. This would be the first step in finding correlations between an individual skeletal site parameters and fracture incidence.

1.3. Importance of marrow fat assessment

Bone marrow occupies the space between the trabecular bone matrix and represents 80% of cancellous bone. Red marrow is more hematopoietically active and denser than yellow marrow (1.030 and 0.980 g/cm^3, respectively). The conversion of bone marrow from red marrow to yellow marrow is well known to occur as one ages and can undergo reconversion to red marrow during times of physiologic stress [14-16] (Figure 1-2). Thus, the physical density of marrow can vary depending on the concentration of red and yellow marrow [17, 18].

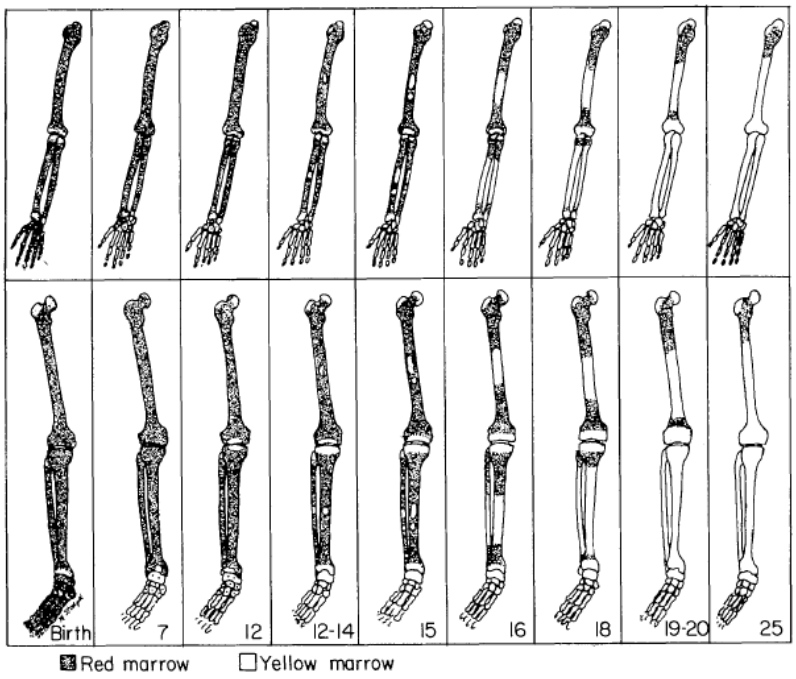

Figure 1-2. Diagrammatic representation of distribution of red and yellow marrow from birth to age 25 years. Taken from Kricun et al. [16].

Although this change is normal as one ages, increased marrow fat can affect the observed BMD of common clinical tools (i.e. DXA). As Blake et al. has demonstrated, the observed difference in density between 100% yellow marrow and 0% yellow marrow for DXA BMD was estimated to be 0.14g/cm^2 for women [19]. This difference may seem insignificant, however, it should be concerning since trabecular bone varies by a small range, 1.0 – 1.2 g/cm^3 [20]. Therefore, changes in marrow composition may confound true changes in cancellous BMD if the two types of marrow are not distinguished [21]. Dual energy CT (DECT) uses differential attenuation from two energies for marrow

correction [22], see Figure 1-3. Details of the dual energy decomposition model will be described in Chapter 3.

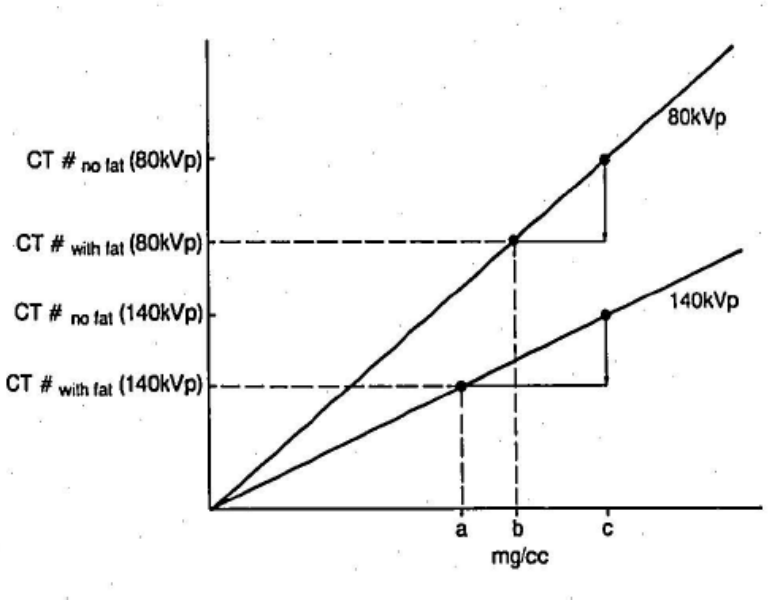

Figure 1-3. Difference in CT# for identical material using dual energy.

It has been shown that increased marrow fat, even when age-corrected, is highly associated with osteoporosis [23, 24]. Yellow marrow fat cells (i.e. adipocytes) are derived from mesenchymal stem cells (MSC) which are non-hematopoietic, pluripotent marrow progenitor cells. These cells can differentiate primarily into either osteoblasts or adipocytes. Under the influence of radiotherapy or chemotherapy, MSC demonstrate enhanced commitment to adipogenesis [25, 26], resulting in reduced osteogenic potential [27] and increased MF.

Increased marrow fat at certain locations is becoming an important biomarker for bone health. Schellinger et al. has also shown that the ratio of marrow fat to BMD

significantly increases the ability to assess the weakening of bone compared to either individually ($p = 0.02$) [28]. Cytotoxic treatments such as therapeutic radiation or chemotherapy can increase the risk of osteoporosis with one of the first signs being increased marrow fat [29, 30]. Cancer treatment induces large changes in marrow composition [31-33].

1.4. Outline of this document

This dissertation follows this outline:

Chapter 2 introduces the modality of micro-Computed Tomography (μCT) and the work done to characterize the machine for assessment of trabecular bone in the murine model. Trabecular bone is studied specifically to describe localized parameters and also to assess the heterogeneity of bone mineral density throughout the entire skeleton. The ideal parameters needed to be identified for imaging the trabecular bone while preventing an excessive radiation dose for μCT. With this optimization, it is possible to quantify trabecular parameters and monitor changes longitudinally. Future work is highlighted and describes the potential of dual isotope micro-PET/CT to identify longitudinal changes due to cytotoxic treatment in both calcified bone tissue and bone marrow. This can be performed in order to assess changes in both compartments throughout the entire skeleton.

The work described in Chapter 3 assesses longitudinal changes in bone health due to cancer treatment in the human body. 29 women were enrolled in a clinical trial

which followed them for 1 year after diagnosis of a cancer of the reproductive system (i.e. ovarian, endometrial, or cervical cancer). Treatment for all women included bilateral salpingo-oophorectomy; however, 17 were further treated with chemotherapy and/or localized radiation therapy. Several imaging modalities were used to assess skeletal health including dual energy absorptiometry (DXA), dual energy computed tomography (DECT), and water-fat magnetic resonance imaging (wfMRI). Results with both DECT and wfMRI show an increase in marrow fat production for patients who underwent chemotherapy and radiation compared to those who underwent oophorectomy alone.

The data presented in Chapter 4 offers a validation of *in vivo* clinical imaging by correlating the modalities of wfMRI and DECT with co-registered histologic analysis. Recently expired human donors were imaged with both modalities and the lumbar spinal column was excised. The midsections of 21 vertebral bodies were processed for H&E histology. The ratio of adipose tissue to total tissue volume in the histologic slides is compared to the signal fat fraction intensities of both imaging modalities. A good correlation ($r > 0.75$) for both wfMRI and DECT is seen when they were compared with each other and with results from histology.

Chapter 5 describes the first assessment of the entire human body using dual energy CT for cancellous bone heterogeneity. 10 control and 10 cancer-treated donors are examined with DECT shortly after death and imaged from head to toe. 23 major trabecular bone sites are examined and marrow-corrected BMD (mcBMD) values are

compared across the entire skeleton. Trabecular bone is shown to vary from site to site showing heterogeneity throughout the entire body. Correlations between the mcBMD of different skeletal sites show that some sites can be used as a better estimate of trabecular mcBMD than others. However, cancer treatment disrupts these relationships as seen by a loss of average correlation between skeletal sites.

Chapter 6 lists general conclusions and summaries are given from this dissertation. Future research that could be performed following this work is discussed for both clinical and pre-clinical studies.

1.5. Scientific output in this dissertation

1.5.1. Journal Publications

a) **Arentsen, L.**, Hui, S. (2013). Characterization of Rotating Gantry microCT configuration for the *In Vivo* Evaluation of Murine Trabecular Bone. *Microscopy & Microanalysis*.

b) Bolan, P., **Arentsen, L.**, Sueblinvong, T., Zhang, Y., Moeller, S., Carter, J., Downs, L., Ghebre, R., Yee, D., Froelich, J., & Hui, S. (2013). Water-Fat MR Imaging for Assessing Changes in Bone Marrow Composition due to Radiation and chemotherapy in Gynecologic Cancer patients. *Journal of Magnetic Resonance Imaging*.

c) Chityala, R., Pudipeddi, S., **Arentsen, L.,** Hui, S. (2012). Segmentation and Visualization of a Large, High-Resolution Micro-CT Data of Mice. *Journal of Digital Imaging*, 1-7.

d) Yagi, M., **Arentsen, L.,** Shanley, R., Sharkey, L., Kidder, L., White, M., Ogawa, K., Rosen, C., Yee, D., Hui, S. (2014). A dual isotope hybrid whole body micro-PET/CT system reveals functional heterogeneity and early local and systemic changes following targeted radiation to the murine caudal skeleton. *Calcified Tissue International*.

e) **Arentsen, L.,** Yagi, M., Takahashi, Y., Shanley, R., Hansen, K., McArthur, A., Yee, D., Hui, S. *In Situ* assessment reveals skeletal-wide heterogeneity of human cancellous bone using dual energy computed tomography. Submitted to *Osteoporosis International*.

f) **Arentsen, L.,** Yagi, M., Takahashi, Y., White, M., Bolan, P., Hui, S. Validation of marrow fat assessment using noninvasive imaging with histologic examination of human bone samples. Submitted to *Bone.*

1.5.2. Conference Presentations

a) Yagi, M., **Arentsen, L.,** Takahashi, Y., Sharkey, L., Koizumi, M., Xian, C., Rosen, C., Yee, D., Hui, S. (December 2013). A Dual isotope hybrid μCT-PET system reveals functional heterogeneity of bone lining cells and longitudinal changes in marrow from local radiation and chemotherapy. Presented at 99thAnnual Radiologic Society of North America Meeting: Chicago, IL. Available at http://rsna2013.rsna.org/program/?PAGE=1# (SSQ12-06). Accessed June 13th, 2014.

b) **Arentsen, L.,** Brown, K., Bolan, P., Thanasak Sueblinvong, Shanley, R., Ghebre, RG., Minenko, AG., Grammens, G., Lee, C., Yan Zhang, Le, C., Froelich, J., Downs, L., Yee, L., Hui, S. (October 2013). Multimodality Imaging to measure and map treatment effect on marrow fat distribution and it's relation with BMD: Results of a pilot study in cancer survivors. Presented at 35th Annual American Society of Bone and Mineral Research meeting, Baltimore, MD. Abstract in J Bone Miner Res 28 (Suppl 1). Available at http://www.asbmr.org/education/AbstractDetail?aid=8812c94a-30d8-4b58-91a4-8fd63c8f03c5. Accessed June 13th, 2014.

c) Yagi, M., **Arentsen, L.,** Takahashi, Y., Sharkey, L., Koizumi, M., Xian, C., Rosen, C., Yee, D., Hui, S. (October 2013). A Dual isotope hybrid μCT-PET System Reveals Functional heterogeneity of bone lining cells and longitudinal Changes in Marrow from Local radiation and chemotherapy. Presented at 35th Annual American Society of Bone and Mineral Research meeting: Baltimore, MD. Abstract in J Bone Miner Res 28 (Suppl 1). Available at http://www.asbmr.org/education/AbstractDetail?aid=3828c732-3919-4b9d-8e9c-42370a777a74. Accessed June 13th, 2014.

d) Hui, S., **Arentsen, L.,** Sueblinvong, T., Downs, L., Potter, D., Grammens, G., Ghebre, R., Allen, S., Minenko, A., Zhang, Y., Le, C., Froelich, J., Jackson, G., Bhattacharyya, M., Yee, D. (October 2013). A Novel 41Ca Assay to measure short and long-term mineral kinetics in patients undergoing cancer therapy. Presented

at 35th Annual American Society of Bone and Mineral Research meeting: Baltimore, MD. Abstract in J Bone Miner Res 28 (Suppl 1). Available at http://www.asbmr.org/education/AbstractDetail?aid=4eb83fcc-01bf-4a88-b685-950fc4a5e360. Accessed June 13th, 2014.

e) **Arentsen, L.,** Hui, S. (October 2013). Multimodality imaging to measure and map treatment effect on marrow fat distribution and it's relation with BMD. Presented at 4th Annual Masonic Cancer Center research Symposium: Minneapolis, MN.

f) **Arentsen, L.,** Brown, K., Bolan, P., Thanasak Sueblinvong, Shanley, R., Ghebre, RG., Minenko, AG., Grammens, G., Lee, C., Yan Zhang, Le, C., Froelich, J., Downs, L., Yee, L., Hui, S. (September 2013). Multimodality Imaging to measure and map treatment effect on marrow fat distribution and it's relation with BMD: Results of a pilot study in cancer survivors. Presented at Annual Clinical and Translational Science Institute Meeting, Minneapolis, MN.

g) Yagi. M., **Arentsen, L.**, Hui, S. (August 2013). Early Time effect of local radiation on entire normal bone marrow. Presented at 55th Annual American Association of Physicists in Medicine Meeting: Indianapolis, IN.

h) Yagi. M., **Arentsen, L.,** Takahashi, Y., Sharkey, L., Koizumi, M., Xian, C., Yee, D., Hui, S. (May 2013). Assessment of functional heterogeneity and longitudinal effect of local radiation and chemotherapy on entire skeletal bone and marrow using dual isotope hybrid μCT-PET system. Presented at 2nd Joint Meeting of the

International bone and Mineral society and the Japanese Society for Bone and Mineral Research (IBMS-JSBMR 2013): Kobe, Japan.

i) Hui, S., Bolan, P., **Arentsen, L.,** Sueblinvong, T., Downs. L., Ghebre, R., Froelich, J., Yee, D. (September 2012). Water-Fat MR Imaging for Assessing Therapy-Induced Bone Marrow Damage in Gynecological cancers. Presented at Annual Clinical and Translational Science Institute Meeting: Minneapolis, MN.

j) **Arentsen, L.**, Hui, S. (July 2012). Characterization of Rotating-Stage microCT for the analysis of trabecular bone in mice. Presented at 54th Annual American Association of Physicists in Medicine Meeting: Charlotte, NC.

k) **Arentsen, L.**, Hui, S. (April 2012). Characterization of Rotating-Stage microCT for the analysis of trabecular bone in mice. Presented at North Central Chapter AAPM Semi-annual Meeting (NCCAAPM): Minneapolis, MN.

l) **Arentsen, L.**, Coghill, K., Fairchild, G., Hui, S. (October 2011). Investigation of skeletal heterogeneity & impact on cancer treatment. Presented at North Central Chapter AAPM Semi-annual Meeting (NCCAAPM): Wisconsin Dells, WI.

m) **Arentsen, L.**, Hui, S. (April 2011). Tracking treatment induced changes in bone and marrow using Dual Energy QCT. North Central Chapter AAPM Semi-annual Meeting (NCCAAPM): Rochester, MN.

CHAPTER 2: **CHARACTERIZATION OF MICRO-CT FOR THE MURINE MODEL AND USE ON LOCALIZED AND WHOLE-BODY IMAGING**

2.1. Introduction

2.1.1. Motivation for whole-body imaging using micro-CT

With increased cancer survivorship [34], there is an increased and unmet need to evaluate treatment-related skeletal damage, including the understanding of mechanisms of damage that will lead to preventive strategies. Over the years, Micro-computed tomography, or micro-CT, has been used for studying bone loss in mice [5-7]. Although it is typically used for single micron-level resolution for individual excised bones, it can also be used on anesthetized animals. This would reduce the number of mice needed since each mouse could be used as its own control in a longitudinal study. The imaging setup for harvested bone is similar to full animal imaging. But, certain precautions need to be considered [8] in full animal imaging. As we've shown previously, the dose to the live animal has to be increased as the resolution increases. This puts a limit on the resolution, especially when one attempts to image the entire skeleton.

Despite these constraints, full animal imaging has been conducted and described in historical literature [11-12]. Granton et al. [13] have demonstrated rapid imaging of rats using cone-beam micro-CT to measure non-invasively whole-body adipose tissue volume (ATV), lean tissue volume (LTV), skeletal tissue volume (STV), and bone mineral

content (BMC). Although the whole body was imaged, their resolution was 486 x 160 x 880, much smaller compared to our data set of 2048 x 2048 x 6300, a difference of two orders of magnitude. Such large datasets present problems in computation and visualization since the file sizes are so large (i.e. approximately 60 GB).

Although the results presented here are for imaging of sacrificed mice, the protocol is being developed with in-vivo imaging of live animals in mind.

2.1.2. Rationale for the characterization of rotating gantry micro-CT for *in vivo* imaging

Micro-CT has become a useful imaging modality for investigations in a multitude of disciplines. Areas of application can range from material science [35] to the study of human pathologies in small animal models [36]. Micro-CT is desirable to illustrate small animal anatomy because of its non-destructive acquisition [37, 38]. There currently exist two main configurations for commercially available micro-CT systems: a fixed source and detector combination with a rotating sample or a fixed sample with a rotating source and detector[39]. The latter is preferable for *in vivo* imaging since the specimen can be affixed to the sample holder in a horizontal position. Before whole body imaging can be performed, micro-CT must first be characterized in order to assess both regional changes in cancellous bone and skeletal changes.

It has been shown that slight physical parameter changes of the micro-CT can drastically affect the resulting image quality [40, 41]. When high-resolution images are needed for the analysis of detailed anatomy (e.g., trabecular bone) physical parameters

must be precisely appointed. It is even more crucial to establish these parameters when investigating changes to live specimens over time. Images must be taken with limited dose and a short acquisition time to minimize the amount of anesthesia required.

The goal of this work is to characterize the rotating gantry micro-CT modality for *in vivo* small animal trabecular bone imaging and use it to assess BMD throughout the entire murine skeleton. This is done using the physical parameters of magnification, binning, filtration thickness, peak energy, and soft tissue thickness.

Table 2-1 summarizes the physical parameters that are tested to characterize the rotating gantry μCT.

	Magnification	Binning	Energy (kVp)	Filter Thickness (mmAl)	Phantom
Magnification	1.3x, 1.8x, 3.3x	2	80	0.5	3
Binning	3.3x	1, 2, 4	80	0.5	3
Peak Energy	3.3x	2	80, 70, 60, 50, 40	0.5	1
Filtration	3.3x	2	80, 40	0.0, 0.5, 1.0, 1.5	1
Tissue thickness	3.3x	2	80, 40	0.5	2

Table 2-1. Table of experimental parameters. Phantom 1: Density-equivalent material; Phantom 2: 7mL Water and 7mL Butanol tubes; and Phantom 3: A micro-CT wire phantom. All scans performed with manufacture-recommended calibrations. Exposure times are determined by peak within 75-85% CCD range

Experiments involve altering the beam geometry and quantization, through magnification and binning, and the average energy through filtration and peak energy. In general, physical magnification is varied for the rotating gantry μCT configuration by changing the distances between the x-ray source and the sample being imaged. Binning is the averaging of local voxels into one 'super voxel'.

The energy of the acquisition beam can be directly modified by altering the electric potential, i.e. peak energy (kVp) across the source. When filtration is added to a polychromatic radiation beam, the probability of a photoelectric interactions increases by $1/E^3$ (where E is the energy of the incident photon). In other words, adding filtration attenuates lower energy photons more resulting in a higher average energy beam [42, 43]. Similarly, increasing the thickness of the surrounding tissue will preferentially attenuate more of the radiation beam's lower energy photons. Reducing lower energy photons in the acquisition beam is beneficial to *in vivo* experiments because lower energy photons are mostly attenuated by the specimen and only increase absorbed dose [44]. As well, without low energy photon attenuation many artifacts such as cupping, streaks, and flair artifacts that prevent accurate BMD estimation would occur [45].

Similar to beam filtration, increasing the thickness surrounding a ROI causes more low energy photons to be attenuated before reaching the detector. To reduce the standard deviation of regions of interest, it is preferable to scan anatomy with less tissue thickness such as the distal humerus or proximal tibia. These locations are

imaged best when the appendage is stretched from underneath the body to beside the head or tail. This will reduce the amount of tissue surrounding the region of interest as seen by a decreasing standard deviation.

In longitudinal studies, a small animal may undergo body mass changes that can increase the tissue surrounding regions of interest such as bone [46]. Also, at different skeletal locations between different species of small animals, the surrounding tissue can be quite different. Thus, more tissue implies an increased amount of absorption of lower energy photons. The beam parameters were selected from guidelines for micro-CT imaging set forth by Bouxsein et al. [47]. Different parameter combinations are measured in terms of Hounsfield Units for a uniform region of interest (ROI).

Image acquisitions of the left distal femur of mice are taken to assess the effects these physical parameters have on dose, scan time, and trabecular microstructure estimation. The objective is to describe the optimal rotating gantry micro-CT acquisition protocol for imaging microscopic skeletal anatomy of mice *in vivo*.

2.2. Methods

This study utilized a commercially available Siemens Inveon Micro-CT (Siemens Medical Solutions USA Inc. Molecular Imaging, USA). The system was equipped with a 165 mm detector with a field of 4,064 x 4,064 pixels and a dynamic range of 67dB for Bin1 to 84dB for Bin4. A description of binning is provided below. Recent publications have assessed the physical parameters of the Inveon micro-PET and micro-SPECT modalities [48]. However, after reviewing the published literature, no characterization

of the Inveon MM µCT modality for the *in vivo* examination of mouse trabecular bone could be found.

Hounsfield Unit (HU) values for different density equivalent materials were evaluated using the Inveon Research Workstation (IRW) Version 3.0 (Siemens Molecular imaging, Germany) and ImageJ Version 1.44 [49]. All scanning protocols employed the maximum current available, 500 µA. Exposure time was modified according to the recommendations of the manufacturer. To keep the experiment constant, each scanning protocol captures 180 images over a single 360 degree rotation. Manufacture-recommended calibrations were implemented for every scanning protocol. These included the center-offset calibration and the HU scale calibration. The HU calibration was performed whenever a change in parameters affects the geometrical magnification, x-ray voltage, or x-ray filter thickness. The reconstruction protocols for all parameter tests employed the same Shepp-Logan reconstruction filter as well as utilizing the Bilinear Interpolation method. A polynomial-based soft tissue beam hardening correction employing coefficient values commonly used for scanning the average mouse was also used for reconstructing all images.

Three types of calibration phantoms were used to characterize the Inveon micro-CT.

- Phantom 1: A Siemens-provided density equivalent cylinder made of Lucite that has six holes drilled axially as seen in Figure 2-1. Rods of different densities were inserted into 4 of the hollow cylinders to represent the typical

density diversity found in the bone and soft tissue of small animals [50]. The densities include: 1.750 g/cm^3, 1.250 g/cm^3, 1.050 g/cm^3, and 1.000 g/cm^3 with the other two holes empty to simulate an air-equivalent density. The surrounding lucite has a density of 1.040 g/cm^3.

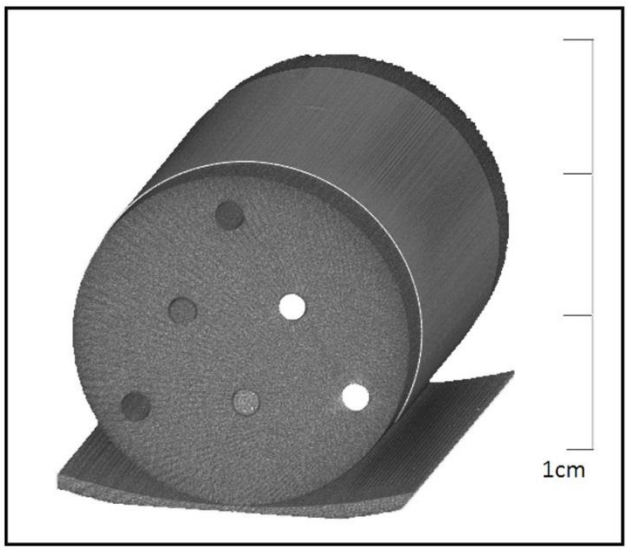

Figure 2-1. Phantom 1: 3D reconstruction of density phantom with 6 densities: 1.750 g/cm^3, 1.250 g/cm^3, 1.050 g/cm^3, 1.000 g/cm^3, and two air-equivalent densities. The surrounding Lucite material has a density of 1.040 g/cc.

- Phantom 2: Two 7 mL polyethylene tubes scanned individually; one filled with Type 1 deionized water (1.00 g/cm^3) and the other with laboratory grade butanol (0.781 g/cm^3). The liquids can be used to theoretically approximate the average density of the two types of bone marrow (1.030 g/cm^3 for red marrow and 0.98 g/cm^3 for yellow marrow).
- Phantom 3: A micro-CT wire phantom produced by Quality Assurance in Radiology and Medicine (QRM) GmbH (Moehrendorf, Germany) was scanned

to determine spatial resolution (line pairs/mm). A 10 μm tungsten wire is suspended in air along the central axis of a sturdy resin cylinder. They cylinder was scanned along the central axis of the micro-CT rotating gantry. After a line spread function was integrated from a small region of interest surrounding the wire, the 10% Modulation Transfer Function (MTF) was assessed similar to previous work [51].

2.2.1. Beam Geometry

Three Source-to-Axis Distances (SAD) and Source-to-Detector Distances (SDD) were used to alter magnification of the system. This changed the resolution of the images as quantified by a change in effective pixel size. The magnification was altered from 3.3x (100.8 mm SAD, 333.8 mm SDD) for high magnification, to 1.8x (183.6 mm SAD, 320.5 mm SDD), and 1.3x (263.6 mm SAD, 336 mm SDD) for medium and low resolution, respectively. The scan protocols were set up in series so that no external intervention would alter the position or orientation of Phantom 3 in between magnification changes. The three options for the Inveon MM μCT scanner are no binning, or Bin1, a binning of 2, or of 4. Bin2 is the average of 4 neighboring voxels into 1 voxel while bin4 takes the average of 16 neighboring voxels. The images for Phantom 3 were taken at 80 kVp energy with a 0.5 mmAl filter and a magnification of 100 mm SAD. The detector consists of pixels that are spaced 32 μm apart and when using 80 kVp and 500 μA a nominal focal-spot size of approximately 60 μm is produced. MTF

measurements were performed for the nine parameter combinations and the spatial resolution at 10% was evaluated [52].

2.2.2. Beam Energy

To characterize the effect of the x-ray beam's peak energy, five different kVp acquisition beams were used to image Phantom 1. The beams ranged from an electric potential of 40 kVp to 80 kVp at increments of 10 kVp. All five beams had a 0.5 mmAl filter, a current of 500 μA, and a binning of 2. The acquisition time was increased as peak kilovoltage decreased. For example, exposure time ranged from 750 msec to 3,000 msec for 80 and 40 kVp, respectively. The ROIs used to analyze each density cylinder of Phantom 1 were equal in dimensions with a volume of 1.5 mm^3.

Four filter thicknesses were investigated: 0.0 mmAl (no filtration), 0.5 mmAl, 1.0 mmAl, and 1.5 mmAl. The Inveon MM μCT does have a built in Beryllium window that is 0.254 mm thick; however it afforded a negligible intrinsic beam hardening effect. Image acquisitions at 40 and 80 kVp, bin2, and 100 mm SAD were performed at four filtration thicknesses to scan Phantom 1.

To assess the effect of beam hardening caused by tissue increase, three sheets of Superflab bolus material (Radiation Products Design, INC. Minnesota, USA) were used: no bolus, 2 mm bolus, and 5 mm. Each sheet was cut so that it could wrap around a Phantom 2 tube without overlap. This arrangement allows for a beam hardening test

due to the beam attenuation in tissue. All scans were performed using identical acquisition and reconstruction protocols.

2.2.3. Localized *In Vivo* imaging

Four healthy, adult mice were affixed to a carbon fiber loading plank in the prone position. The left leg was stretched inferiorly so that the femoral axis was approximately aligned to the axis of the rotating gantry. The left, distal femur was examined for trabecular bone microstructure using the 3D Analysis Tool on the IRW system. The analysis volume was held constant between 0.3 mm and 1.0 mm from the growth plate in the femoral metaphysis. Previous studies have used this ROI to examine trabecular bone changes in small animal studies [53]. To qualitatively evaluate image quality, each mouse was scanned at one of four binning and magnification combinations to represent the range available on a typical rotating gantry micro-CT (Table 2-2). The total exposure time was about 34 seconds for low resolution images and increased to over 126 seconds for high resolution images. This was due to the increased exposure time per projection required to increase the photon count for the detector. The difference in acquisition time for Table 2-2 was due to the warm up calibration that should be performed before every acquisition with higher resolution images taking 2.6 times longer. This increases the detector reliability and can be performed immediately prior to *in vivo* studies (i.e. before placement of animal specimen).

Isotropic Pixel Size (µm)	9.19	18.4	36.78	95.4
Magnification	3.3x	3.3x	3.3x	1.3x
Binning	1	2	4	4
10% MTF (line pair/mm)	11.76	8.85	4.36	2.51
BMD estimation (mg/cc)	1585	1556	1443	1384
BV/TV estimation (%)	9%	16%	19%	43%
SNR (Mean/SD)	1.66	4.21	6.93	19.2
Acquisition Time (min:sec)	13:26	10:24	5:19	5:17
Radiation Dose (cGy)	125.7	117.3	31.9	†4.0
Total Exposure Time (s)	126	139	36.0	34.2

Table 2-2. Results of four magnification and binning combinations. 10% MTF Spatial Resolution (lp/mm), Bone Mineral Density (BMD) estimation, Bone Volume to Total Volume ratio (BV/TV), Signal-to-Noise Ratio (SNR), and Edge definition indicate optimal setup at 3.3x magnification with a binning of 2 (18.39 µm isotropic pixel size).

The amount of radiation absorbed is also a criterion for assessing optimal scanning parameters when imaging *in vivo* samples. Dose to the specimen due to CT exposure is influenced by resolution, beam energy, and SNR. As Equation 2-1 shows, increasing the SNR will cause an increase in dose while resolution and slice thickness have an inverse effect on dose.

$$D = a\left(\frac{s^2}{e^3 b}\right)$$

Equation 2-1. Estimating patient dose where D is dose, *a* is a constant, *s* is the SNR, *e* is the spatial resolution, and *b* is the slice thickness.

Dose can also be assessed by examining the coefficient of variation in the linear attenuation coefficient of a material as developed by Ford et al. [54], specifically relating the effect of altering the voxel size as seen in Equation 2-2.

$$\frac{\sigma}{\mu} \propto \frac{1}{\Delta x^2 \sqrt{D}}$$

Equation 2-2. Fractional coefficient of variation relative to the linear attenuation coefficient of water, $\frac{\sigma}{\mu}$. Δx is isotropic voxel spacing and D is dose.

They propose that to keep the coefficient of variation (i.e. image quality) constant but decrease the isotropic pixel size from 90 to 9µm, the dose will need increase by 10^4. Combining signals from neighboring CCD detector elements increases the slice thickness, thus decreasing the dose. The decrease in SNR due to increasing magnification is explained by beam divergence. As the number of detector CCD elements increases to accommodate a magnified image, more photons are required for them to activate. As Thurner et al. has described, binning will also reduce the noise of the image [55]. Another effect of binning is reduced acquisition and exposure times since it requires less photon interactions. Acquisition time, or the time taken from initiation of the protocol to the last projection image prior to reconstruction, also decreases as pixels are binned together. It is important to reduce the acquisition time to as small as possible to minimize the time for the animal to twitch and to limit the amount of anesthesia.

To accurately assess the radiation dose to the bone, an incision was made on the left leg of four mice. Micro-TLDs (Radiation Products Design, Inc., Albertville, MN, USA), sealed in plastic to protect from bodily fluids, were used to measure dose due to imaging parameters. Two micro-TLDs were then inserted anterior and posterior to the

femur to assess an average dose to bone. The incision was then stitched back together using 6-0 surgical thread. The same four magnification and binning protocols were used to scan the mice to assess the changes the protocols have on dose absorption. An 80 kVp beam with 0.5 mmAl filter was held constant for all scans while exposure time was modified according to manufacturer recommendations. After 24 hours post imaging, the microTLDs were read on a Harshaw TLD Model 5000 reader (Thermo Fisher Scientific, Inc., Waltham, MA, USA).

2.2.4. Methodology for whole-body imaging

Three healthy Balb/C mice of approximately 15 weeks in age were sacrificed using gas asphyxiation and placed in a 4^0C refrigerator for 4 to 30 hours. Individually, each mouse was removed from the refrigerator and affixed to a thin, concave, carbonate plank in a prone position. The arms were stretched superior and legs stretched inferior. Effort was placed in ensuring that the spine was centered and as straight as possible throughout the whole body. The plank with mouse was inserted into the micro-CT loading bay. Scout views were taken to verify correct position and selection of scan distance.

An x-ray technique of 80 kVp energy, 500 μA current, and an exposure time of 750 ms were used to image each mouse. The micro-CT scanner was set to a 3.3x magnification. The reconstructed image slices were 2048 x 2048 pixels (37.66 mm x 37.66 mm) in the trans-axial dimension. The dataset was comprised of more than 6,000

axial slices with a total length of 113 mm. Four different couch positions were needed in order to scan the entire 20-gram carcass. At a projection angular interval of 2 degrees, four rotations produced 720 projection images. Axial overlap of 20% was stitched together for each rotation to make the final image.

The Hounsfield unit (HU) was calibrated using a 50 mL centrifuge tube filled with de-ionized water, using the scanning setting that was the same as the mouse scan. The Hounsfield unit was calculated using equation:

$$HU = \frac{(\mu - \mu_{water})}{\mu_{water}} * 1000 \qquad \text{(Equation 2-3)}$$

where μ is the attenuation coefficient.

For calibrating BMD, Phantom 1 was scanned with the same protocol as the mice scans. The image of the bars was reconstructed and calibrated to HU. The resulting HU values for each bar were then used to determine the HU-to-BMD conversion formula [Figure 2-9].

2.2.4.1. Visualization

The first step in determining the BMD was to segment the bone from the rest of the mice data [Figure 2-2]. Since there are large numbers of slices, the Renyi entropy method was used for segmentation. The algorithm was implemented in Matlab R2011a from Mathworks Inc. Adaptive local Renyi entropy (ALREP) method was employed by Ravishankar Chityala, PhD of the Minnesota Supercomputing Institute [56, 57]. The process is described below.

For each image

a) Perform Global Renyi entropy and determine the threshold (also called global renyi threshold).
b) Divide the image in to multiple blocks
c) For each block, determine if there are significant number of pixels in that block that have pixel values greater than the global renyi threshold.
d) In each of the block that was marked as containing significant number of pixels, perform local Renyi Entropy based thresholding.
e) Assemble the individual blocks to obtain the complete segmented image.
f) Determine the BMD value for the segmented regions using the relationship established by the method described in the previous section.

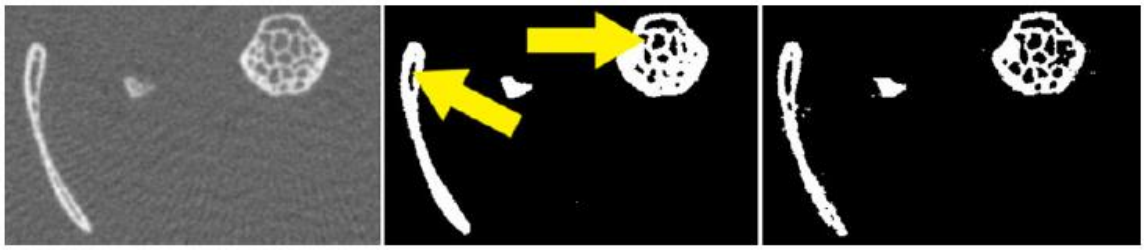

Figure 2-2. Comparison of a region-of-interest of the 1000th slice. (Left) Original image (Center) Global Renyi Entropy (GREP) (Right) ALREP method. Note that the GREP method resulted in over-segmentation (shown by arrows), causing fine gaps (marrow) to be either filled in comparison to the original image.

Manual segmentation was performed to compare the quality of the segmented results from ALREP. For each data set, 60 slices (approximately 10% of the slices) were considered. These slices were segmented by manually thresholding using Avizo [58]. The threshold was chosen such that the bone region was completely segmented. BMD of the segmented region was calculated by implementing the calibration equation derived from Phantom 1. This program identified only the regions corresponding to the bone in the original slice data using the bone location in the manually segmented images. The mean value of BMD in the bone region was then calculated.

Avizo was used for visualization. Since the server had large memory, the entire dataset (50GB in size, approximately) was read completely to memory to perform iso-surface rendering [Figure 2-3].

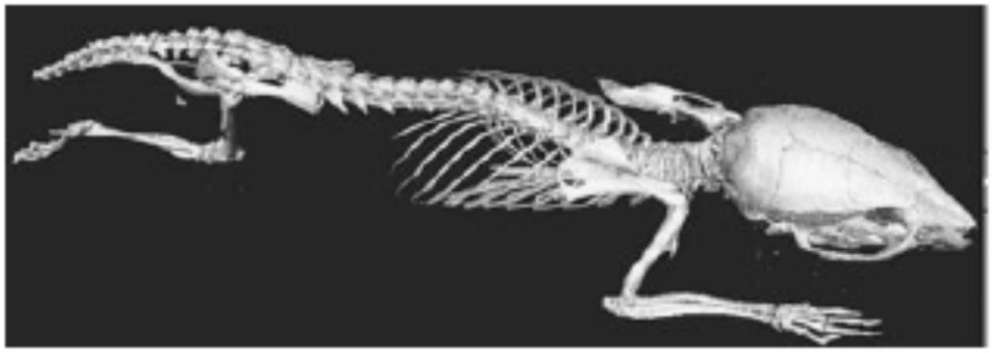

Figure 2-3. Reconstruction of whole body mouse image acquisition. First visualization of high resolution (Isotropic pixel size = 9.19µm; > 6,300 slices) micro-CT dataset.

2.3. Results

2.3.1. Beam Geometry

The physical parameters used to alter spatial resolution were binning and magnification. They can alter isotropic, or nominal, pixel sizes from 9.19µm for a bin1 and 1.3x to 95µm using Bin4 with 3.3x magnification. The 10% MTF spatial resolution at the 9.19µm isotropic pixel size resulted with 11.8 lp/mm and with 2.5 lp/mm at 95 µm. As magnification increased, the spatial resolution increased if binning was held at 2. For 3.3x, 1.8x, and 1.3x the 10% MTF were 8.9 lp/mm, 5.3 lp/mm, and 3.4 lp/mm, respectively. As the magnification decreased the Signal-to-Noise Ratio (SNR) increased as well. With all other variables remaining constant, the SNR increased from 4.2 at 1.3x to 9.0 and 13.0 at 1.8x and 3.3x, respectively.

The standard deviation of pixel values drastically decreased as binning increased from 724 HU at bin1 to 260 HU at bin2 at 1.750 g/cm^3 equivalent density material. Scan time took as long as 13.4 min at Bin1 to 10.4 min to 5.3 min at Bin2 and Bin4, respectively. For image sets with equivalent axial and transaxial lengths, the file sizes decrease in size from 2.35 GB to 296 MB to 40 MB for Bin1, Bin2, and Bin4 respectively.

2.3.2. Beam Energy

Figure 2-4 shows that as peak energy increases, HU values for 1.750 g/cm^3 equivalent material decreases at a rate of nearly -290 HU/kVp.

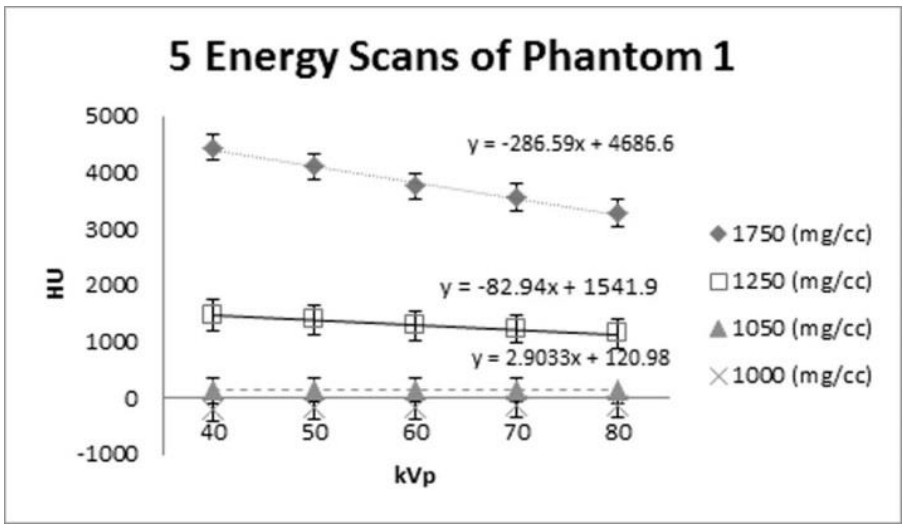

Figure 2-4. Difference in HU of Phantom 1 with change in Energy. Notice at lower energies the difference between low and high densities is greater.

At 1.250 g/cm^3 the HU values decreased as energy increased but at a lesser rate, -83 HU/kVp. Similarly, it is shown in Figure 2-5 that as beam filtration increased the difference in HU between water and bone-equivalent densities (e.g. 1.750 g/cm^3) decreased. The effect was not as noticeable when the energy of the beam was decreased to 40 kVp. The standard deviation of pixel values between different energies or filtrations remained constant. Therefore, SNR decreased when the peak energy or the filtration thickness increased.

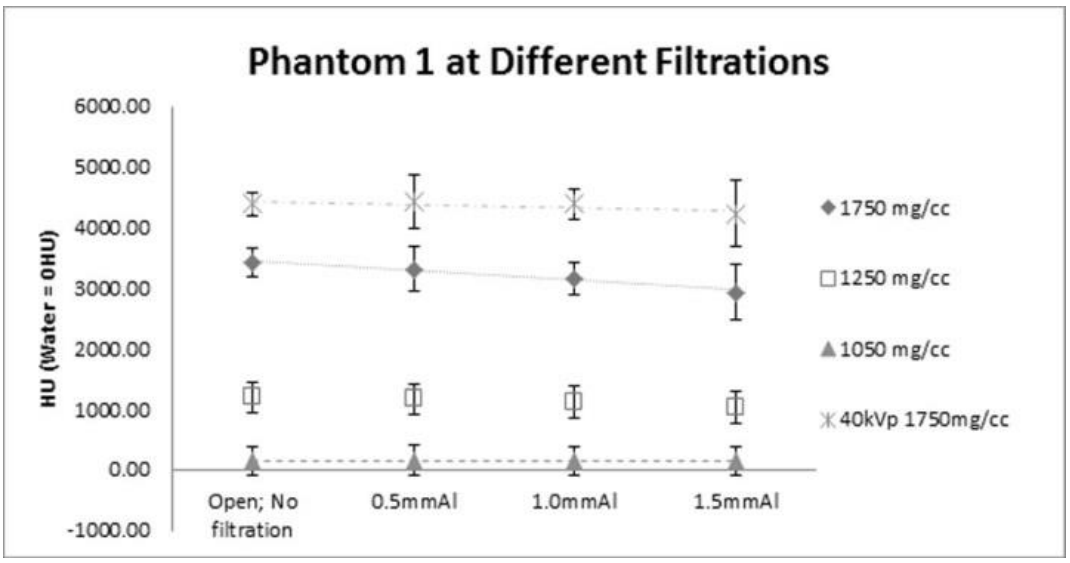

Figure 2-5. Filtration effect for different densities. All curves produced with 80 kVp energy except for labeled 40 kVp. Notice as filtration thickness increases, discernment between water and 1.750 g/cm^3 density decreases. HU values for 1.750 g/cm^3 using 40 kVp remain relatively constant as thickness increases; however, exposure time increases.

Under identical acquisition parameters, increasing the sample thickness caused increased pixel value standard deviation at the center for both liquid compositions in Phantom 2. The minimum standard deviation, 161 HU, was observed when no bolus surrounded Phantom 2. Standard deviation increased to 200.1 HU and 231.6 HU after a 2 mm and 5 mm sample thickness was added, respectively. The average HU value for water and butanol remained constant for all tissue thickness escalations.

2.3.3. Localized *In Vivo* Model

Scanning the *in vivo* models at four different binning and magnifications changes the isotropic pixel sizes to 9.19 µm, 18.39 µm, 36.78 µm, and 95.39 µm as presented in Table 2-2. As spatial resolution increased, or the nominal pixel size decreased, the Bone

Volume to Total Volume ratio (BV/TV) estimation increased. This trend of increasing BV/TV with decreasing resolution was observed in other *in vivo* studies[59]. Conversely, Bone Mineral Density (BMD) estimation and absorbed dose decreased when spatial resolution was decreased. Figure 2-6 shows image cross-sections that were taken in the plane perpendicular to the axis of the femur at 0.5mm superior to the distal growth plate in the femoral metaphysis.

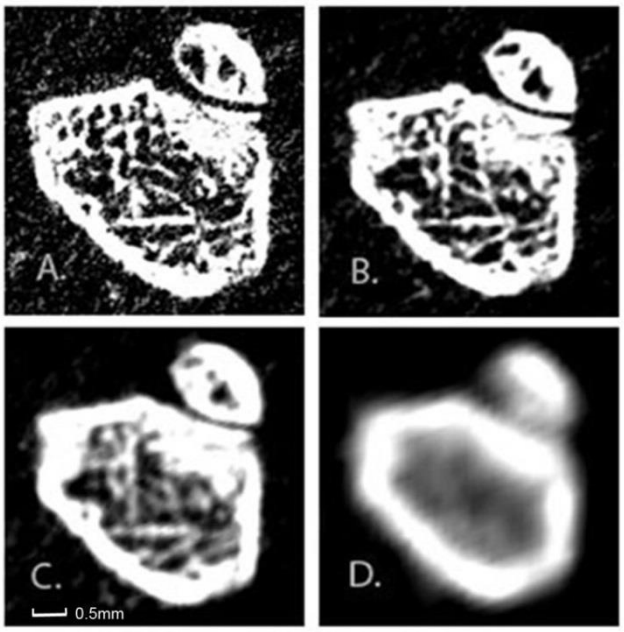

Figure 2-6. Effect of isotropic pixel size on image clarity. All images were taken perpendicular to the femoral axis at 0.5mm from the growth plate using Siemens Inveon MicroCT. A. 9.19 µm, B. 18.39 µm, C. 36.78 µm, and D. 95.39 µm. Notice increased noise in A. but gross loss of detail with C and D.

Although the image appears clearest at 9.19 µm and blurriest at 95 µm nominal pixel size the SNR increased from 2 to 19, respectively. As seen in Table 2-2, a decrease in absorbed dose from approximately 125 cGy to 4 cGy was witnessed when resolution

decreases for high resolution to low resolution scans, respectively, with a correlation of $r = 0.973$.

2.3.4. Whole body imaging findings

The left panel of Figure 2-2 is the 1000^{th} slice of a mice data set. The image has been cropped and contrast enhanced to show only the region of data containing the mice. The results of ALREP are shown in the right panel of Figure 2-2. The sizes of the segmented objects from ALREP very similar to the original data.

The average BMD value in the ALREP segmented bone region was determined and is plotted for all slices in Figure 2-7. The plot contains the results for three different mice titled 15-1, 15-4 and 15-5. The mean value of BMD for the manually segmented data for all three cases is also plotted on the same figure. The BMD for the ALREP is plotted with lines while the manually segmented values are plotted with markers at each data point. The x-axis is arranged so that the lower numbers are the head and the higher numbers are the tail of the mice. The labels for various regions are also marked in the figure. It can be seen that the three curves corresponding to the three mice follow similar pattern but with different values for each slice.

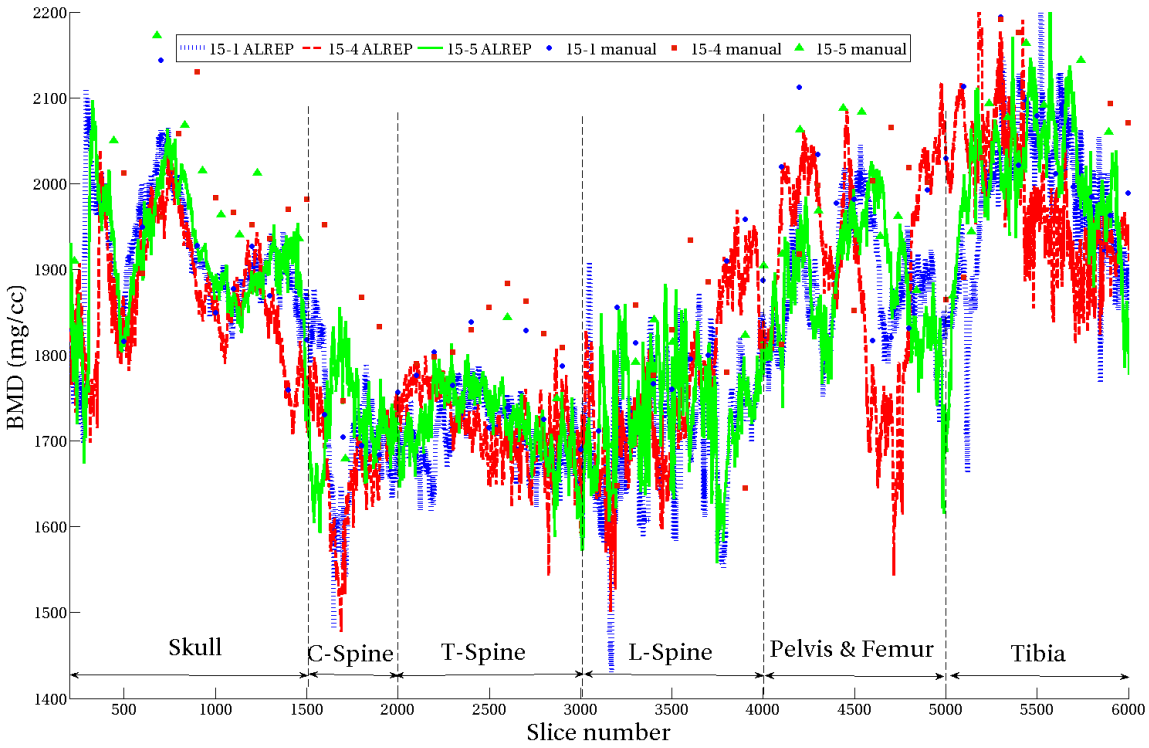

Figure 2-7 Average value of the bone mineral density in mg/cc from the segmented region determined using ALREP and manual method. The ALREP method results are labeled as 15-1 ALREP, 15-4 ALREP and 15-5 ALREP and the data points are connected by lines. The manual segmentation results are labeled as 15-1 manual, 15-4 manual and 15-5 manual and the data points are shown with markers.

In order to visualize the variation in BMD for the same slice across three mice, an average and standard deviation plot was created and is shown in Figure 2-8. The average and standard deviation of BMD was calculated across three mice for each slice using ALREP. For a given slice (a vertical line in the plot), the centerline is the average BMD value and the standard deviation of BMD flanks either side of the filled area. This plot provides a window to the variation of BMD across three mice for the same slice or anatomy. As in Figure 2-7, the lower numbers for the x-axis correspond to the head of

the mice while the higher numbers correspond to the tail of the mice. The labels for various regions are also marked in the figure.

The BMD calibration was performed based on the process described in section 2.2.4 and the results are presented in Figure 2-9. The fitted curve has the following equation:

$$BMD = 0.2241 * HU + 1018.40 \qquad \text{(Equation 2-4)}$$

The regression coefficient for the fit was 0.99831. The segmented pixel values (in HU) were processed using the above equation to obtain the corresponding BMD value.

The results are summarized in Table 2-3. The processing time for 6300 slices was 150 minutes on a dualcore 2.6 GHz processor and 4 GB of RAM. Although manual segmentation was performed only for 60 slices, it took 1 minute to process one slice. Hence for 6300 slices, it would have consumed around 6300 minutes or 4.4 days. Thus, the ALREP method has a speedup of more than 40 times compared to manual segmentation. Also, manual segmentation of such large data set would result in significant human error and hence is not a feasible long-term solution.

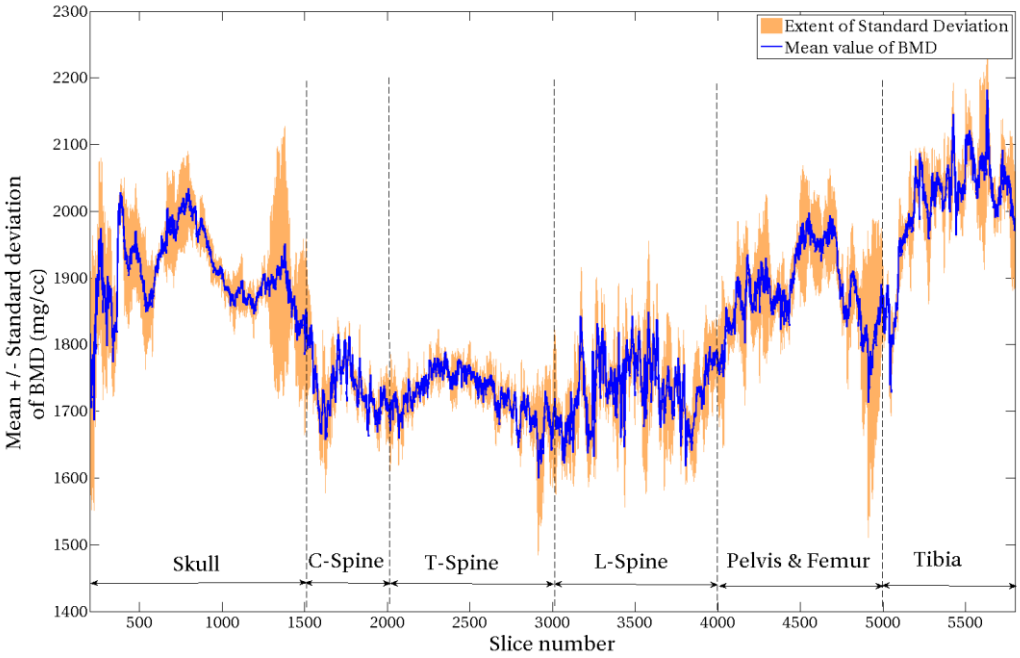

Figure 2-8 Average and standard deviation plot of BMD obtained using ALREP. The average and the standard deviation are calculated across the three datasets. The centerline is the average BMD and the standard deviation flanks either side of the average.

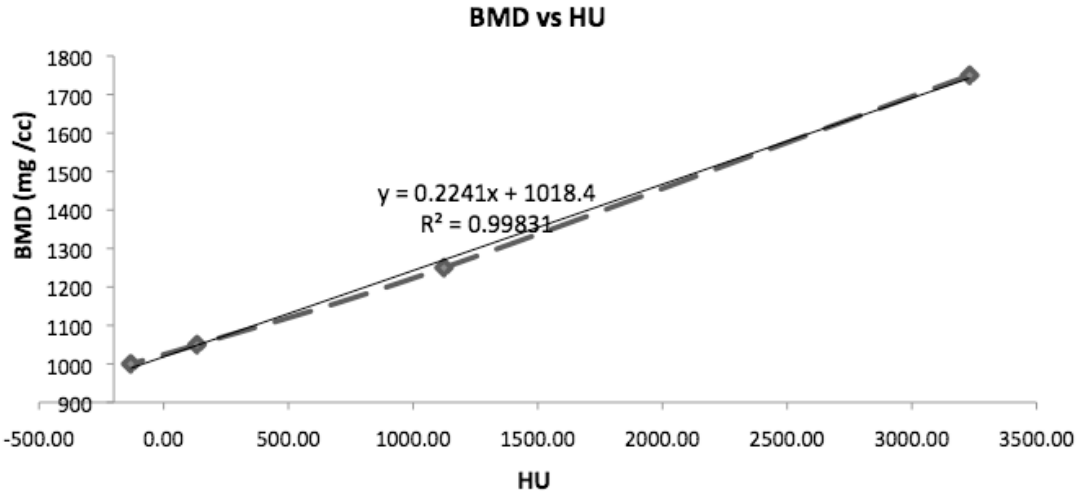

Figure 2-9 Calibration curve for BMD. The HU of a phantom containing inserts for which the value of electron density was known was imaged and the curve was plotted. A straight line fit was then performed on the data points. The equation of the fitted line and its regression is shown in the plot.

Table 2-3 Comparing ALREP and manual method.

	ALREP segmentation	**Manual segmentation**
Processing time	150 minutes	6300 minutes or 4.4 days
Speedup compared to manual segmentation	42 times	-
Accuracy	Accurate segmentation due to local thresholding	Over-segmentation due to use of a single threshold

2.4. Discussion

2.4.1. Localized *in vivo*

Five parameters are examined to investigate the effects of magnification, binning, peak kilovoltage, beam filtration, and tissue thickness. Results were assessed by their effect on resolution, SNR, and absorbed dose. Different magnification and binning settings can be combined to produce image sets with different resolutions. Figure 2-10 demonstrates different spatial resolutions that can be achieved by the Inveon MM micro-CT while also providing a threshold of a 60µm effective pixel size.

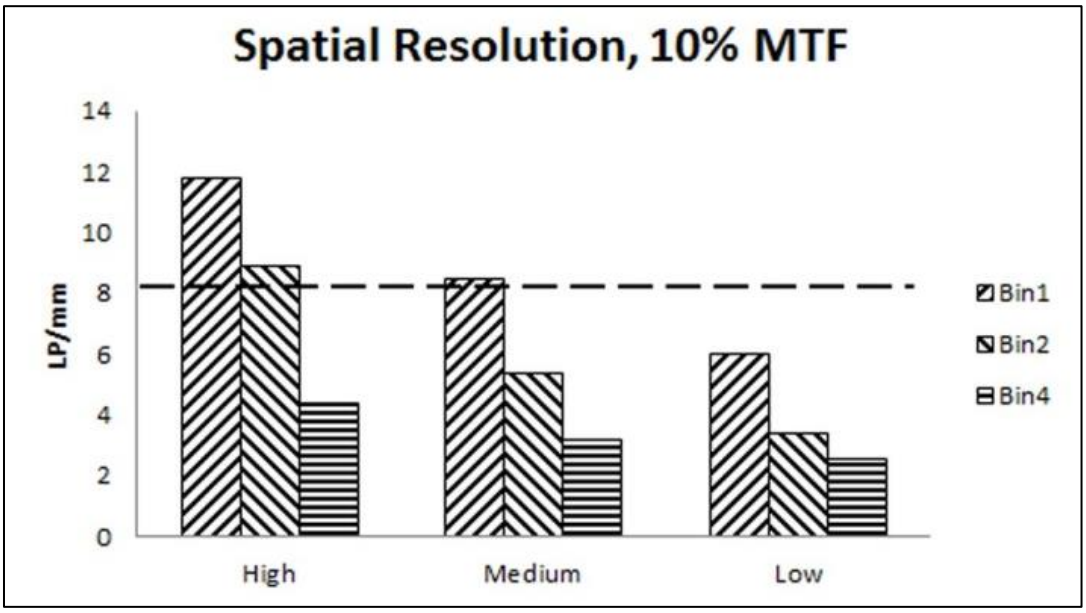

Figure 2-10. When magnification decreases or binning increases, the spatial resolution will decrease. The dotted line represents a resolution threshold above which have been used to image trabecular bone in murine model [60, 61]. Magnification: High (3.3x), Medium (1.8x), Low (1.3x)

Pixel sizes below 60 µm have been used to provide images capable of analyzing trabecular bone microarchitecture in a mouse model [59-61]. For the Inveon MM µCT, a binning of 4, no matter the magnification, cannot produce a spatial resolution below this threshold. Similarly, a magnification smaller than 1.8x does not produce an effective pixel size that can be used to image murine trabecular bone. Therefore, imaging protocols using rotating-gantry µCT must have a binning less than 4 and a magnification greater than 1.8x to optimally image the trabecular bone of a murine model.

The apparent HU variations due to changes in beam energy seen at higher density material can be explained by the linear attenuation coefficient. When the average energy increases, either by higher peak energy or increased filtration, the material's attenuation coefficient is reduced. Hounsfield Units are directly proportional to the linear attenuation (Equation 2-5).

$$HU = \frac{\mu(x)_E - \mu(H2O)}{\mu(H20)}$$

Equation 2-5. HU calculation where $\mu(x)_E$ and μ(H2O) refer to the linear attenuation coefficient of a material and water respectively at a known energy.

Therefore, as energy increases, the densities approach the density of water, the HU values decrease as energy increases.

2.4.2. Whole-body imaging

A system for segmenting and visualizing large micro-CT data set of mice was presented. The data set is of size 2048 x 2048 x 6300 pixels and around 50GB in size. Since the data set is large, it presents considerable challenge. The data was segmented to obtain the bone using Adaptive Local Renyi Entropy (ALREP). Manual segmentation was performed to study the effectiveness of ALREP. The manual method of segmentation took 6300 minutes (approx.) for 6300 slices, while the automated method took only 150 minutes, 40 times faster than manual process. Since a typical desktop does not have the capability to read and render large datasets, a new high-end

visualization system was used. VirtualGL and Avizo were used for visualization at 12 frames per second on a 1 Gbits per second network.

Step c in ALREP method is used to determine if a given block of the image has a significant number of pixels. The image was divided into 16 blocks along x and 16 blocks along the y-direction. Each block thus has a size of 128 x 128 = 16384 pixels. For the analysis, a region was assumed as significant if it had at least 20 pixels with values greater than the global renyi threshold. The 20-pixel value is significantly lower than the number of pixels in a block. Hence increasing the number from 20 will not make a big change in the block significance process.

2.4.3. Translation significance

This method can potentially be implemented to study the longitudinal effects of cancer treatment on the entire skeleton thereby simulating recently developed preclinical [16] and clinical models [17] of cancer survivors' bone health. Employing diagnostic CT using quantitative computed tomography in a clinical model, we have demonstrated that patients with ovarian or endometrial cancer experience an accelerated and distinct pattern of bone loss from systemic chemotherapy vs. local pelvic radiation. Many radiotherapy patients (e.g., head and neck or cervical cancers) undergo multiple whole-body PET-CT scans. These CT scans may be used to generate regional as well as complete skeletal BMD distribution, thereby providing important

information on the heterogeneity of treatment effects following radiation, chemotherapeutic, or a combination of treatment modalities.

2.4.4. Conclusion

To properly analyze the trabecular bone in mice it is necessary to use parameters that will acquire images with both an acceptable resolution and Signal to Noise Ratio (SNR). For live imaging, there is also a priority to reduce absorbed radiation dose and shorten the acquisition time. To assist with dose reduction and increase SNR, the sample should be positioned so as to reduce as much extra tissue as possible from the field of view.

In conclusion, the optimal imaging parameters for a rotating gantry micro-CT in the assessment of trabecular bone in mice are an 80 kVp beam with a 0.5 mmAl filter and magnification of 3.3x with binning of 2. These parameters result in an isotropic pixel size of 18.39 µm that has an acceptable SNR of 4.21 and a spatial resolution of 8.9 lp/mm. The 80 kVp energy and 0.5 mmAl filter make the beam optimal by the attenuation of low energy photons to reduce dose and moderate the acquisition time. This configuration provides quality images that are sufficient for examining longitudinal changes in the trabecular bone of mice. Future work can be done to assess changes in the trabecular bone of mice related to cytotoxic interventions (e.g., radiation induced bone loss).

We have developed a method to automatically segment the bone and study its mineral density. We have demonstrated using a large data set of size greater than 50GB that segmentation can be obtained within 150 minutes. This method has been shown to be considerably faster than manual segmentation. We also demonstrated the use of specialized hardware and software for visualization of these data sets.

2.5. Further direction

Further work is described in the supplemental data at the end of this dissertation. Studies were performed to measure functional heterogeneity of the murine skeletal system and response to chemotherapy and localized radiation exposure. Mice were longitudinally examined using micro-CT and micro-PET using dual isotope to measure changes to the calcified tissue as well as active bone marrow.

CHAPTER 3: **CANCER THERAPY CAUSES RAPID AND HETEROGENEOUS EXPANSION OF MARROW FAT AND DECREASED BONE MINERAL DENSITY**

3.1. Introduction

Cancer survivors experience a greater risk of fracture compared to the general population [62-66]. However, the effect of cancer treatment, especially the relationship between marrow fat (MF) and bone mineral density (BMD), are not well known. Mesenchymal stem cells (MSC) are non-hematopoietic, pluripotent marrow progenitor cells which give rise primarily to osteoblasts and adipocytes. Under the influence of radiotherapy or chemotherapy, MSC demonstrate enhanced commitment to adipogenesis [25, 26], resulting in reduced osteogenic potential [27] and increased MF, a major source of serum adiponectin. However, changes in MF are not readily detected by a traditional dual-emission X-ray absorptiometry (DXA) scan, since DXA only calculates average BMD by superimposing cortical and cancellous BMD. We demonstrated that radiation-induced increases in MF were not reflected in equivalent loss of cancellous bone in ovariectomized compared with intact mice [67].

Changes in marrow composition can alter determination of BMD as mentioned in Section 1.3. The physical density of red marrow is approximately 1.20 g/cm^3 compared with that of yellow marrow (0.98 g/cm^3). Since cancellous bone is composed mostly of marrow (~80%), changes in marrow composition may confound true changes in cancellous BMD if the two types of marrow are not distinguished. Dual energy CT

(DECT) uses differential attenuation from two energies for marrow correction [22], but has never been translated into osteoporosis clinical care. This may be due to the high radiation dose exposure from multiple CT scans using older scanners, or because age-related osteoporosis typically results in only modest changes in marrow composition. In contrast, cancer treatment induces large changes in marrow composition [31-33]. Moreover, water-fat MRI (wfMRI) could also measure volumetric marrow composition [12]. However, MRI use is limited in cancer patients after diagnosis, perhaps due to its high cost and/or limited availability in some locations. Newly developed technology has reduced the radiation dose to patients and improved imaging quality of DECT [13]. Thus, DECT is frequently performed to diagnose and monitor cancer. We hypothesized that DECT and wfMRI could reliably measure changes in MF associated with cancer treatments.

Our overall goal is to develop clinically useful biomarkers to predict, measure, and monitor cancer-therapy induced bone loss, thereby individualizing therapy to decrease bone morbidity and ultimately enhancing quality of life for cancer survivors. The aims of this pilot study were therefore to 1) assess the ability of DECT to quantify the effects of cancer treatments on MF and marrow corrected BMD (mcBMD), 2) compare information collected by DECT to that collected by WF-MRI and DXA, and 3) explore whether serum adiponectin reflected changes in MF associated with cancer treatments.

3.2. Methods

3.2.1. Subjects

Women older than 18 years old with newly diagnosed ovarian and endometrial cancer who planned to receive chemotherapy or radiation therapy following oophorectomy were eligible for the study. Twelve women with early stage ovarian or endometrial cancer who underwent surgical oophorectomy but not adjuvant chemotherapy or radiation therapy served as the control group. We excluded women with osteoporosis, hyperparathyroidism and those who had received chemotherapy, radiation or hormonal therapy within the prior year. The study was approved by the University of Minnesota Institutional Review Board (#0906M67981) and complies with the World Medical Association Declaration of Helsinki — Ethical Principles for Medical Research Involving Human Subjects.

Twenty-nine patients were recruited for this study. Ovarian cancer patients (n=11) were treated with carboplatin and paclitaxel 175 mg/m^2 every 21 days for ≥6 cycles. Endometrial cancer patients (n=6) were primarily treated using external beam radiation therapy (EBRT) to the pelvis (median dose, 45-50 cGy in 25-28 fractions) and additional radiation at the vaginal surface using high dose rate (HDR) brachytherapy. The radiation window encompassed the pelvis up to ~L5.

Venous blood samples were collected at 0, 6 and 12 months, serum was extracted and stored at -80^{0}C until analysis. Serum adiponectin was measured using a human ELISA kit (R&D Systems Inc., Minneapolis, MN, USA); the lower limit of detection

was 0.246 ng/mL and intra and inter-assay coefficients of variation were 2.5-4.7% and <7%, respectively. Serum resistin was measured using a human ELISA kit (B-Bridge International, Mountain View, CA, USA); the lower limit of detection was 0.2 ng/mL and intra and inter-assay coefficients of variation were <5% and <6%, respectively.

3.2.2. DECT and MR Imaging

DECT scanning (Somatom Definition Flash, Siemens, Germany) was performed at 140 and 80 kVp energy in single scan. Fifteen subjects were imaged at baseline, 6 and 12 months after treatment. A CT calibration phantom (Mindways Software, Austin, TX) commonly used for bone densitometry was positioned under each patient and spanned the scanned volume which extended from L3 through the right femoral neck. QCT Pro (Mindways Software, Austin, TX) was used to derive single-energy (140 kVp) volumetric BMD estimates. DXA (GE Healthcare Lunar Prodigy, Madison, WI) was also performed at 0 and 12 months.

On the same day as DECT imaging, 15 subjects also underwent wfMRI scans at 0, 6 and 12 months using a 3 T Siemens TRIO scanner (TIM Trio, Siemens, Erlangen, Germany). Images were obtained at L1-L5 and the right femoral neck. Detail on the wfMRI method is given elsewhere [12]. Briefly, three consecutive 3D images were acquired with TR=9 ms, TE=2, 3, and 4 ms, parallel imaging acceleration 3x2, and nominal resolution of 1.1 x 1.1 x 2.45 mm. The WF reconstruction was performed using

the method of Berglund et al. (20). The 3D fat fraction image was calculated as MF = fat/(fat+water) and exported in DICOM format for analysis.

For DECT, two different energy CT spectrums (Figure 3-1) can be used for basis material composition estimates [68]. Average basis material composition ($\rho_{H2O}, \rho_{K2HPO4}$) was estimated for an ROI placed within matching regions of in CT data sets acquired at 80 kVp and 140 kVp using the following equations:

$$\rho_{H2O} = \frac{1}{D} \cdot [\beta_{K2HPO4,140} \cdot (CT_{80} - C_{80}) - \beta_{K2HPO4,80} \cdot (CT_{140} - C_{140})] \quad \text{(Equation 3-1)}$$

$$\rho_{K2HPO4} = \frac{1}{D} \cdot [\beta_{H2O,80} \cdot (CT_{140} - C_{140}) - \beta_{H2O,140} \cdot (CT_{80} - C_{80})] \quad \text{(Equation 3-2)}$$

$$D = \beta_{H2O,80} \cdot \beta_{K2HPO4,140} - \beta_{H2O,140} \cdot \beta_{K2HPO4,80} \quad \text{(Equation 3-3)}$$

where CT_{80} and CT_{140} are the average CT values within the defined ROIs and $\beta_{H2O,80}$, $\beta_{H2O,140}$, $\beta_{K2HPO4,80}$, $\beta_{K2HPO4,140}$ are calibration slopes determined from CT calibration phantom measurements.

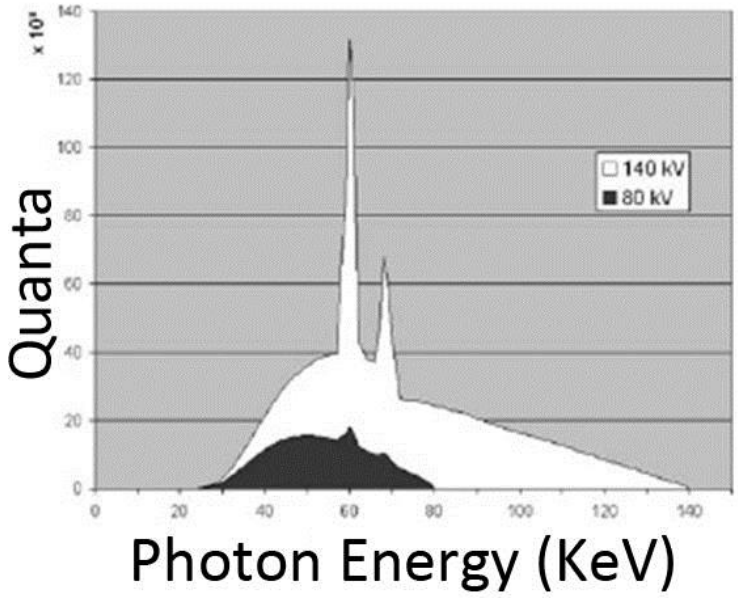

Figure 3-1. Dual energy spectrum used in Siemens SOMATOM ® dual source computed tomography scanner. The difference in energy can be utilized to identify material through basis material decomposition. Image taken from Johnson et al. [69].

This can be used to assess bone ROIs relative to the manufacturer-reported basis material compositions for the CT calibration phantom[17]. These basis material compositions were interpreted relative to water and a theoretical prediction of the basis material composition of yellow marrow obtained from energy-dependent mass attenuation coefficients calculated using an openly available tool (XCOM) [69, 70], atomic composition data from ICRU Publication 46 and a density of 0.93 g/cm^3 [71]. Patient measurements were projected onto the line in the basis material space connecting the basis material composition of yellow marrow and that of water using a minimum distance projection, P, parameterized such that the position P=100% corresponded to yellow marrow and the position P=0% corresponded to water. The

DECT-derived estimate of MF was calculated using: MF = 0.348 * P + 85.7%. We performed linear transformation of these DECT fat-fraction estimates to the MRI fat-fraction scale, taking into account average mcBMD among the study subjects. The transformation did not impact measurement correlation, supporting its use in detection of longitudinal changes in fat fraction.

3.2.3. Statistics

Statistical models were used to evaluate mcBMD and MF trends over time by treatment, skeletal region, and imaging modality. Graphical methods such as scatterplots and boxplots identified important relationships, such as measurement distributions and within-patient correlation over time, which informed analysis methods. Linear regression was used to estimate the functional relationship between DECT and WF-MRI MF measurements. Differences in MF or mcBMD based on treatment or skeletal region were analyzed using generalized estimating equations (GEE*) models [72], with each model employing one outcome measured by a single imaging modality. Each model had main effects for age, time (0, 6 and 12 months) and treatment (or region), an interaction effect of time and treatment (or region) and modeled within-subject correlation using an exchangeable structure. Wilcoxon signed rank tests were applied to evaluate changes over time for individual factor levels, such as a particular treatment or skeletal region. Region models included all patients who received oophorectomy, radiation, or chemotherapy, and treatment models use measurements

fixed at a single region, either L4 or L5. Reported p-values were not adjusted for multiple testing. Unless otherwise stated, results are in terms of the mean or difference in means between groups or times, and differences are given in absolute, not relative, units. All analyses were performed using R version 2.10.1.

3.3. Results

Table 3-1 summarizes demographic characteristics of all subjects. One patient died during the study and thus, results are reported for sixteen subjects with paired data. MF was higher by (estimated change ± standard error) 0.32 ± 0.12 absolute percentage points for each additional year of age ($p=0.005$). Likewise, mcBMD was lower by 1.1 ± 0.3 mg/cm3 for each additional year of age ($p<0.001$).

	Treatment modalities (cancer type)		
Variable	**Chemotherapy**	**Radiation Therapy**	**Oophorectomy**
Sample Size	11	6	12
Age, years	55 ± 17	52 ± 7	53 ± 6
Body Mass Index, kg/m^2	27 ± 5	32 ± 6	35 ± 6
DXA % Fat at baseline	42 ± 8	46 ± 7	48 ± 6
DXA % Fat at 12 months	43 ± 7	44 ± 10	49 ± 5

Table 3-1. Demographic Characteristics of Subjects. Data are summarized using the mean ± standard deviation. Chemotherapy was the principal treatment modality for ovarian cancer, radiation therapy was primarily used to treat endometrial cancer, and oophorectomy was performed in early stage ovarian and endometrial cancer patients who did not require subsequent radiation or chemotherapy.

We observed a high overall correlation (r = 0.77, 95% CI: 0.69, 0.83) between DECT and WF-MRI based MF quantification at L3, L4, and L5 for 15 subjects (Figure 3-2) with r = 0.80 (95% CI: 0.65, 0.89) at baseline; r = 0.68 (95% CI: 0.47, 0.81) at 6 months; r = 0.66 (95% CI: 0.44, 0.80) at 12 months. Likewise, changes in MF from 0 to 12 months were highly correlated by both imaging methods (r = 0.91, 95% CI: 0.84, 0.95).

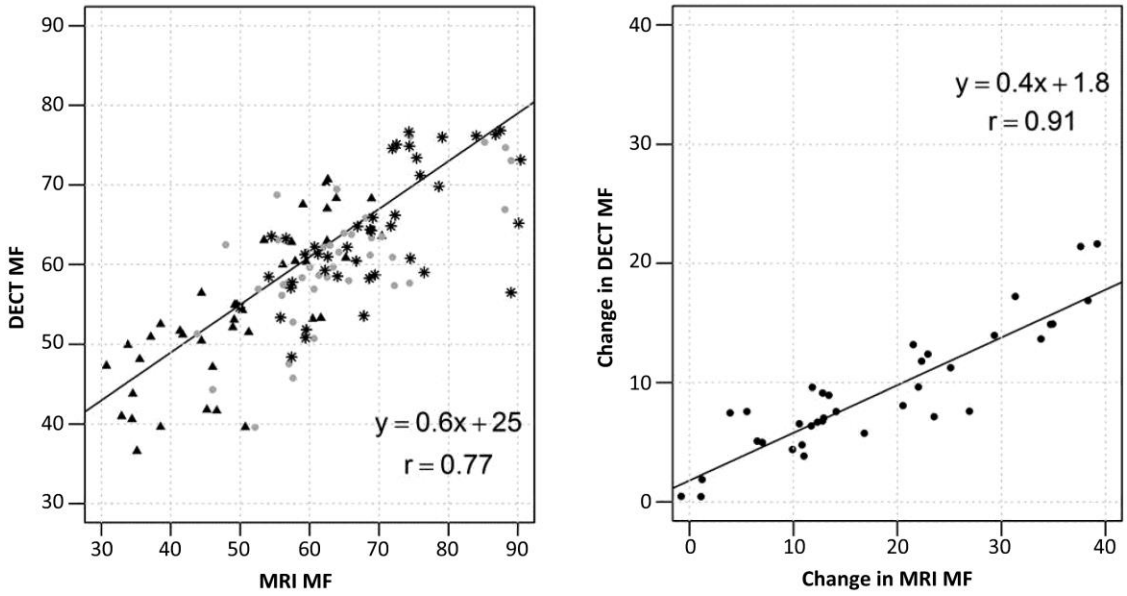

Figure 3-2. Correlation between DECT and WF-MRI marrow fat (MF) at L3, L4 and L5. A) A high correlation (r=0.77, 95% CI: 0.69, 0.83) in MF measurements (includes L3, L4, and L5) between the two imaging modalities was observed at baseline (triangle), 6 (circle) and 12 months (star) post treatment. B) Measurements of absolute change in MF from baseline to 12 months were highly correlated between the two imaging methods (r= 0.91, 95% CI: 0.84, 0.95)**.**

Figure 3-3 shows the effect of all treatments on individual skeletal regions. At baseline, absolute percent difference in MF by DECT (Figure 3-3A) varied. MF in L3 and L4 were equivalent, whereas L5 MF was lower by 4% ($p<0.001$) and FN MF was higher by 13% ($p<0.001$), relative to L3 and L4. MF increased in all regions over time ($p<0.001$), with an estimated mean change of 7% from baseline to 12 months. The degree of change was similar among the four regions imaged ($p=0.27$). Using WF-MRI (Figure 3-3B), MF also increased in all four regions over time ($p<0.002$). L3-L5 MF increased by

15% from baseline to 12 months. The increase in FN MF was approximately half the increase of L3-L5 (p=0.025).

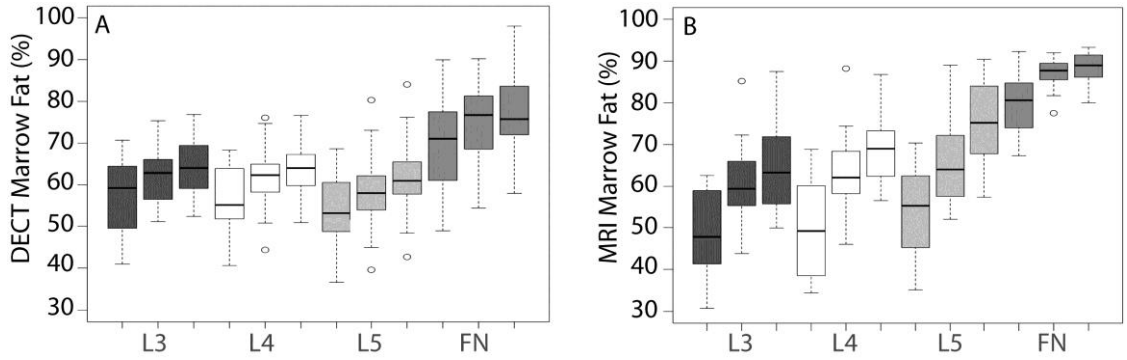

Figure 3-3. Region Effects on marrow fat or MF measured by DECT (A) and MRI (B). The colored region of each boxplot represents the 1st and 3rd quartile range of observations, with a black line at the median. Whisker lines are placed at the 1.5 interquartile range of the lower and upper quartile and outliers are noted with open circles. A. DECT: Regions differed in mean MF at baseline. L3 and L4 were equivalent, and L5 was lower by 4% (p<0.001) and FN higher by 13% (p<0.001) relative to L3 and L4. MF increased over time at all sites measured (p<0.001), with an estimated mean change of 7% from baseline to 12 months for all regions. The degree of change in MF was similar among the four regions (p=0.27). B. MRI: Regions differed in mean MF at baseline. L3 and L4 were equivalent, L5 was higher by 5%, and FN was higher by 32% (p<0.001). MF increased over time at all sites measured (p<0.002), with an estimated mean change of 15% from baseline to 12 months for L3-L5. In contrast to DECT, the increase in FN MF was approximately half the increase of L3-L5 (p=0.025).

We next measured absolute percent change in MF at L4 and L5 after oophorectomy, radiation, and chemotherapy using DECT and WF-MRI (Figure 3-4). The majority of radiation treatment was localized to tissues overlying the L5 vertebral body. L4 MF by DECT increased by 9% after radiation, 9% after chemotherapy, and 4% after oophorectomy (p<0.032). The degree of increase in MF was larger for chemotherapy and radiation relative to oophorectomy (interaction p=0.004). Changes in L5 MF by

DECT (Figure 3-4B) were similar to those seen in L4, although the radiation group had a larger increase in MF at L5. From 0 to 12 months, L5 MF increased by 17% with radiation, 8% with chemotherapy and 4% with oophorectomy ($p<0.032$). The increase in L5 MF was greater for radiation and chemotherapy, relative to oophorectomy (interaction $p<0.001$). Likewise, increased L4 and L5 MF from 0 to 12 months was observed by WF-MRI (Figure 3-4C and D). Changes in L4 MF varied by treatment (interaction $p<0.001$), with smallest increases following oophorectomy (6%) compared to chemotherapy (24%) or radiation (19%).

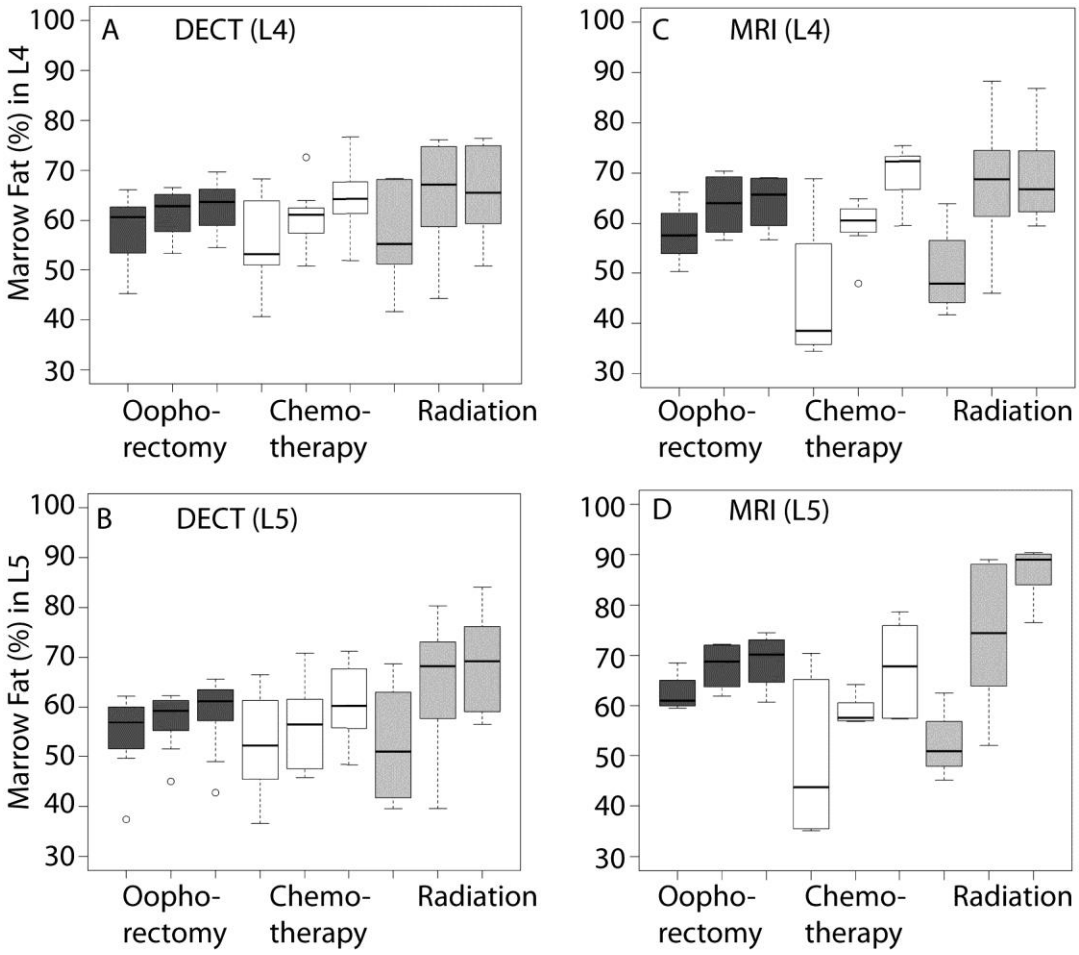

Figure 3-4. Absolute Percent Change in L4 and L5 Marrow Fat by Treatment. A & B: Based on dual energy computed tomography (DECT) imaging in 15 subjects from 0 to 12 months, L4 MF increased by 9% after radiation, 9% after chemotherapy, and 4% after oophorectomy ($p<0.032$). The increase in MF was larger for chemotherapy and radiation relative to oophorectomy (interaction $p=0.004$). From 0 to 12 months, L5 MF increased by 17% with radiation, 8% with chemotherapy and 4% with oophorectomy ($p<0.032$). The change varied based on treatment (time x treatment interaction $p<0.001$). C & D: By water- fat MRI imaging, L4 and L5 MF increased from 0 to 12 months. The change varied based on treatment (time x treatment interaction $p<0.001$). L4 MF increased by 19% after radiation, by 24% after chemotherapy, and by 6% after oophorectomy. Likewise, L5 MF by WF-MRI increased from 0 to 12 months. L5 MF increased by 32% after radiation, by 18% after chemotherapy, and by 6% after oophorectomy.

Mapping of MF distribution was developed using DECT and WF-MRI. Figure 3-5 is a representative figure showing longitudinal changes in MF distribution in the spine associated with chemotherapy. An increase in MF throughout all marrow regions were observed at both 6 and 12 months, long after treatment completion, suggesting systemic and sustained increases in MF resulting from chemotherapy.

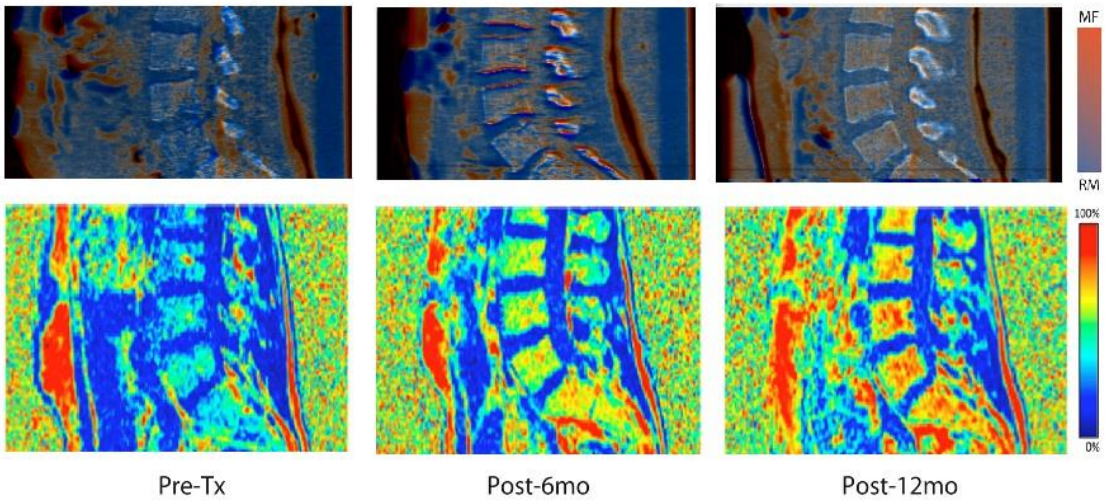

Figure 3-5. Marrow fat mapping of a representative patient using DECT and water-fatMRI. Spine marrow fat mapping: Longitudinal changes in marrow fat distribution in spine due to chemotherapy for a representative subject at a) baseline, B) 6 months and C) 12 months after treatment using DECT (top figure) and water-fat MRI (bottom figure). Changes in MF were visible within 6 months of treatment, and continued to increase at 12 months.

Figure 3-6 shows absolute differences in mcBMD in mg/cm^3 over one year by skeletal region, treatment and imaging modality. DECT-derived mcBMD was significantly different between skeletal regions ($p<0.01$), suggesting inherent skeletal heterogeneity (Figure 3-6A).

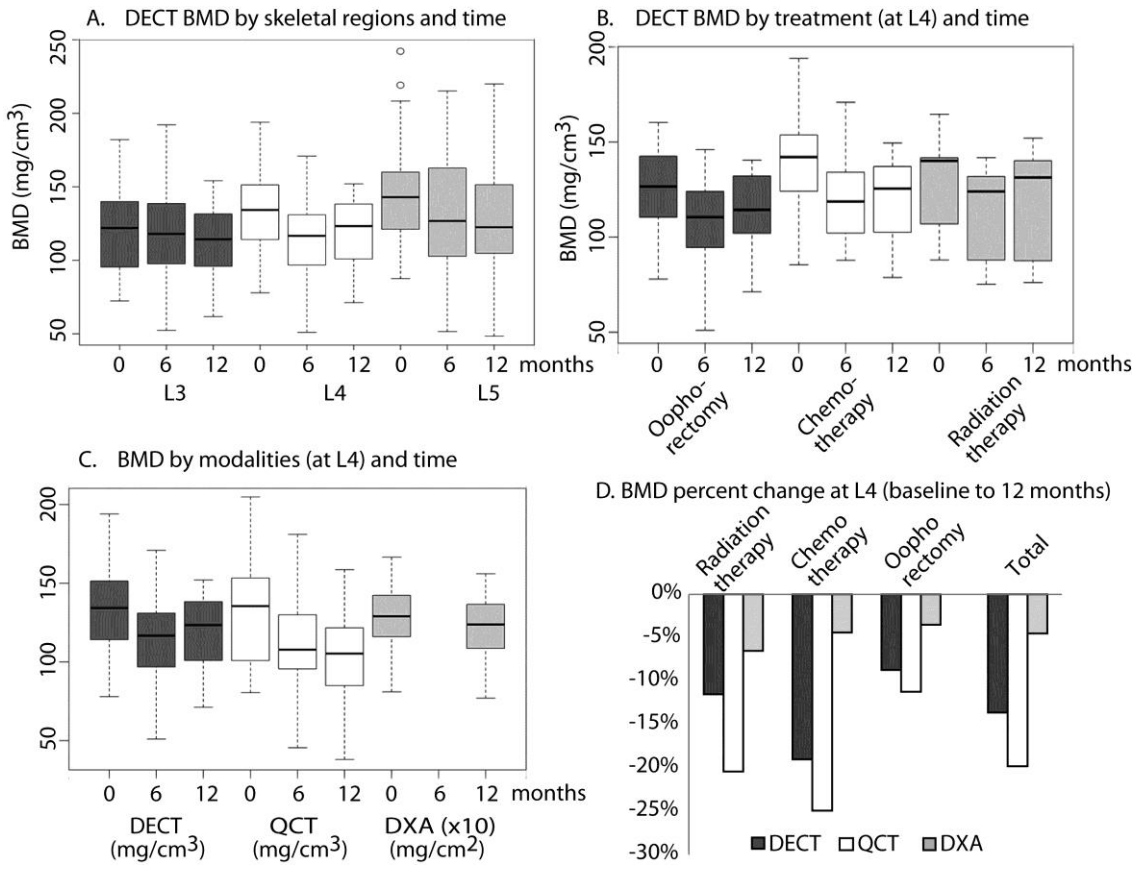

Figure 3-6. BMD changes measured by different techniques. A. DECT mcBMD by skeletal regions and time: Regions differed in mean mcBMD at baseline ($p<0.001$); L4 was higher by 12 mg/cm^3 and L5 by 25 mg/cm^3 relative to L3. mcBMD in all regions decreased over time ($p<0.02$), and change varied by region (time x region interaction $p=0.03$).The 12 month decrease in mcBMD was 7 mg/cm^3 at L3, 14 mg/cm^3 at L4, and 13 mg/cm^3 at L5. B. DECT mcBMD by treatment (at L4) and time: Mean mcBMD measured by DECT at L4 did not vary at baseline based on treatment ($p=0.42$). Chemotherapy decreased mcBMD by 23 mg/cm^3 ($p=0.01$) from 0 to 12 months. Radiation decreased mcBMD by 10 mg/cm^3 ($p=0.09$) from 0 to 12 months, and was lowest at 6 months. Oophorectomy decreased mcBMD by 8 mg/cm^3 from 0 to 12 months ($p=0.24$) and was lowest at 6 months. C &D. mcBMD by modalities (at L4) and time: The median per patient mcBMD percent decrease was 14% for DECT, 20% for QCT, and 5% for DXA ($p<0.002$ for all). The degree of decrease was larger in patients treated with chemotherapy or radiation compared to oophorectomy, and was statistically significant for QCT ($p=0.01$), but not DECT ($p=0.16$) or DXA ($p=0.29$). Note: left subfigure (c) shows absolute measurement and right subfigure (d) shows relative change in mcBMD between baseline and 12 months.

At baseline, L4 was higher by 12 mg/cm^3 and L5 by 25 mg/cm^3, relative to L3. McBMD decreased in all regions over time ($p<0.02$), but the degree of change differed among the regions (interaction $p=0.03$). The decrease in mean mcBMD from baseline to 12 months was 7 mg/cm^3 at L3, 14 mg/cm^3 at L4, and 13 mg/cm^3 at L5. Likewise, decreases in mcBMD differed by treatment. Over twelve months, L4 mcBMD decreased by 23 mg/cm^3 ($p=0.01$) with chemotherapy, by 10 mg/cm^3 with radiation therapy ($p=0.09$) and by 8 mg/cm^3 with oophorectomy ($p=0.24$, Figure 3-6B). Likewise, L5 mcBMD decreased by 26 mg/cm^3 ($p=0.01$) with chemotherapy, by 13 mg/cm^3 with radiation therapy ($p=0.44$) and by 3 mg/cm^3 with oophorectomy ($p=0.52$). One patient with a large mcBMD increase confounded the results for the radiation group at L5.

We next compared changes in L4 mcBMD by treatment and imaging (Figure 3-6C and D). Relative decreases were considered for this comparison due to a different measurement scale for DXA. The median per patient relative decrease in L4 mcBMD was 14% by DECT, 20% by QCT, and only 5% by DXA ($p<0.002$ for all). For QCT, the median decrease in L4 mcBMD was 23% with radiation or chemotherapy and 11% with oophorectomy ($p=0.01$). For DECT, the corresponding reductions were 15% with radiation or chemotherapy and 9% with oophorectomy ($p=0.16$), and for DXA, 6% and 4% ($p=0.29$) with the respective cancer treatments.

Figure 3-7 shows correlations between L4 MF and mcBMD. At baseline, there was negative correlation between MF and mcBMD (Figure 3-7A, B). The degree of correlation varied depending on imaging modality; correlation was high when MF and

mcBMD were measured using DECT and wfMRI, and lower when BMD was measured using DXA. Correlations of changes of MF and BMD due to treatment effects were substantially reduced or absent (Figure 3-7 C, D).

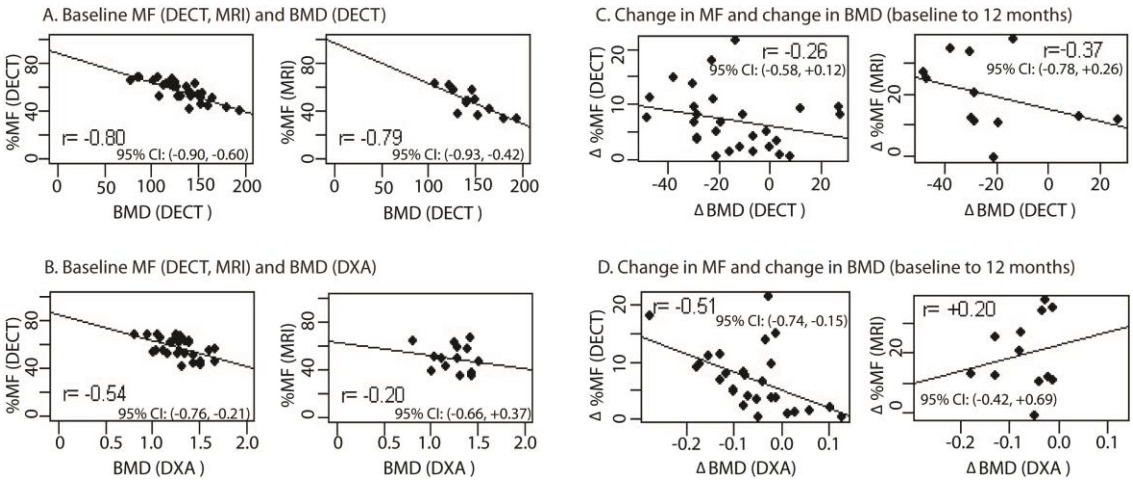

Figure 3-7. Correlation of MF and mcBMD at L4 from different modalities measuring the same patient. The panel on the left shows absolute measurements at baseline. The panel on the right shows changes from baseline to 12 months.

The impact of cancer treatment on circulating adiponectin, resistin, and body fat were also measured. The percent body fat measured by DXA for chemo-radiation treated and oophorectomy group remained same for the one year study period (p=0.29, 0.55 respectively, paired t-test). Adiponectin was 7, 10, and 13 ul/ml at 0, 6, and 12 months respectively and levels increased significantly from 0 to 12 months (p=0.0023, repeated measure one way ANOVA). We observed smaller increases in adiponectin after oophorectomy (6, 8 and 9 ul/ml at 0, 6 and 12 months, p=0.16). A weak correlation (baseline, r=0.26, 95% CI: (-0.32, +0.69) and change from baseline to 12 months r=0.24,

95% CI: (-0.36, +0.70) was observed between MF and adiponectin. Resistin levels decreased significantly after radiation and chemotherapy (7, 4 and 3 ng/mL at 0, 6 and 12 months, p=0.012). By contrast, resistin levels remained stable after oophorectomy (5, 4 and 4 ng/mL and 0, 6 and 12 months, p=0.63).

3.4. Discussion

Cancer survivors' bone health is an emerging problem, due to continued improvements in cancer survival rates worldwide. Appropriate predictive biomarkers are needed to identify patients at high risk of bone loss, permitting individualized therapy to reduce long-term fracture risk. We observed dramatic increases in MF in ovariectomized mice after radiation, without an equivalent loss of either bone or hematopoietic cellularity [67]. Since bone surfaces are generally quiescent following ovariectomy [73], and rapidly dividing cells are radiosensitive, we expected radiation to have greater adverse effects on marrow than bone. We therefore designed the current study to investigate changes in MF following treatment with radiation and chemotherapy, using oophorectomy as our control.

Age related osteoporosis is associated with a high inverse correlation between MF and mcBMD. In our study, the most striking observation was a failure to maintain a high inverse correlation between MF and mcBMD after cancer treatment. Instead, we observed rapid expansion of the MF which did not correspond to an equivalent decrease in mcBMD. Since MF and mcBMD are not inversely correlated following cancer therapy,

our study suggests that BMD and MF should be measured separately. Furthermore, DECT and not DXA might be more reliable to measure BMD in cancer survivors, until the predictive value of MF is established in predicting fractures.

To our knowledge, ours is the first study to measure and image MF in ovarian and endometrial cancer patients using DECT and wfMRI. Our study confirms that DECT can measure changes in both MF and mcBMD after cancer treatment. MF increased significantly more following radiation and chemotherapy, relative to oophorectomy (interaction $p<0.001$). We therefore conclude that increased MF in cancer patients is not due to loss of ovarian function alone. Kugel et al. measured vertebral MF using magnetic resonance spectroscopy; MF increased by <1% per year between ages 30-60 in women [74]. By contrast, cancer survivors in our study experienced large (9-32%) increases in MF over one year. Interestingly, regions demonstrated heterogeneity in MF at baseline. Additionally, changes in MF varied by both treatment and time, possibly due to differing treatment schedules for chemotherapy (several months) versus radiation (one month). In the case of radiation, the 6 to 12 month increase in MF was relatively smaller than the 0 to 6 month increase. Whether this adipogenic process continuously increases with time, or stabilizes, is of our future interest. Study participants experienced increases in serum adiponectin that were not associated with increased body fat, but were associated with increased MF. Cawthorn et al. (personal correspondence) found that MF could generate adiponectin. Future studies are needed to clarify whether serum adiponectin levels can be used to judge changes in MF associated with cancer therapies.

Our study had several limitations. The sample size was relatively small and the study period was limited to one year. Subgroup analysis was limited, as numbers in each treatment group were small. Since the field of view of second energy source was smaller than the first in DECT scanner (30 cm vs. 50 cm, respectively), one may need to be careful while deriving parameters such as MF and mcBMD. The measured MRI fat fraction used in this study included some bias from T1 and T2*, which could be corrected in future work with more sophisticated acquisition and reconstruction techniques [75]. Finally, the small number of serum samples (n=14) limited our ability to assess changes in serum adiponectin and resistin by treatment group.

3.4.1. Conclusions

In summary, we established the feasibility of DECT and WF-MRI to measure the impact of cancer treatment on MF and mcBMD. Because CT is routinely used to diagnose cancer and monitor response to therapy, DECT could characterize changes in skeletal health (MF and mcBMD) with little or no additional cost or radiation exposure. We suggest that MF and mcBMD should be considered independently, when monitoring the adverse effects of cancer therapy. Future longitudinal studies in cancer survivors are needed, to determine how long increased MF persists following cancer therapy, how changes in MF associate with changes in mcBMD, whether serum adiponectin can be used to measure changes in MF, and how MF changes correspond to risk of incident fracture.

CHAPTER 4: **VALIDATION OF MARROW FAT ASSESSMENT USING NONINVASIVE IMAGING WITH HISTOLOGIC EXAMINATION OF HUMAN BONE SAMPLES**

4.1. Introduction

Cancellous bone of a single vertebral body is heterogeneous and the density of which can vary by as much as 20% [76]. Common *in vivo* methods of assessing cancellous BMD (e.g. DXA, Quantitative Computed Tomography) integrate the density of calcified tissue with marrow density. However, marrow composition can vary from higher density hematopoietic red marrow to lower density adipocytic yellow marrow. Increased marrow fat can also alter microstructure heterogeneity of the trabecular matrix and has also been shown to influence vertebral failure patterns [77-79]. Most bone histopathology studies were limited in focus to studying osseous structures [80-82] or specific pathologic abnormalities in cancellous bone [83-85]. To our knowledge, there has been no study performed to correlate *in vivo* imaging of bone and bone marrow with coregistered histologic quantification of marrow fat.

We present here a study on the correlation between histologic examination of marrow fat fraction and clinical imaging by means of Dual Energy Computed Tomography (DECT) and Magnetic Resonance Imaging (MRI). DECT has the ability to identify marrow composition through use of basis material decomposition techniques [17]. We have already developed water-fat MRI in a previous study to measure the fat fraction signal in bone marrow [86].

4.2. Method and Materials

4.2.1. Subjects

Donors were accepted into this study as part of a larger investigation into the heterogeneity of cancellous bone. Approval was given by the Anatomy Bequest Program at the University of Minnesota. The five donors were female with a mean age of 57.5 ± 9.3 years. Each subject was diagnosed with cancer and last treated with radiation or chemotherapy within the past 6 months. The diagnoses included cancer of the cervix, breast, and epiglottis and Chronic Lymphocytic Leukemia. Potential subjects were excluded with a history of knee, hip, or shoulder replacement, obesity, or history of treatment for osteoporosis (i.e. a Bisphosphonate). Donors were received by the University of Minnesota Anatomy Bequest Program.

4.2.2. Imaging

Within 24 hours postmortem, fully intact bodies were brought to the Radiology department at the University of Minnesota Medical Center, Fairview in Minneapolis, MN. Each body was first imaged using a Siemens Somatom Definition Flash DECT scanner (Siemens Medical Solutions USA, Inc., Malvern, PA, USA). The scan utilized Dual source CT at energies of 80kVp and at 140kVp with an additional tin filter for accurate image co-registration. Each donor was scanned cephalic caudal to include the entire skeleton. 17 vertebral bodies were analyzed with both MRI and DECT and then processed for H&E examination.

For DECT, yellow marrow volume fractions (YMF) were calculated from basis material composition estimates for bone ROIs relative to manufacturer-reported basis material compositions for the CT calibration phantom (Figure 4-1E and F). The basis material composition formulas used were the same as used in Section 3.2.2. Since red bone marrow is more dense than water, values of P can range from -66% to 100%. The CT-derived estimate of MF was then normalized to the MRI scale without affecting correlation using: YMF = 0.6 * (P + 0.396).

After DECT imaging, the donor was brought to the MRI and imaged on a Siemens Magnetom 3 Tesla MRI scanner (Tim TRIO, Siemens Medical Solutions, Malvern, PA, USA). Three water-fat source images were created with TE = 2, 3, and 4 ms. Specific parameters can be found in Bolan et al. [86]. Water-fat reconstructions were produced from the three multichannel datasets using the method of Berglund et al. [87] (Figure 4-1C and D). Signal-fat fraction (sFF) images were produced and ROIs were recorded in order to ensure accurate co-registration with DECT imaging.

4.2.3. Excision, registration technique

After clinical imaging, vertebral samples were removed by the University of Minnesota Bequest program staff. Vertebral bodies were separated from the pedicles using a diamond tipped bone saw and placed in formalin. 21 individual Lumbar vertebrae were then cleaned of soft tissue to expose cortical bone.

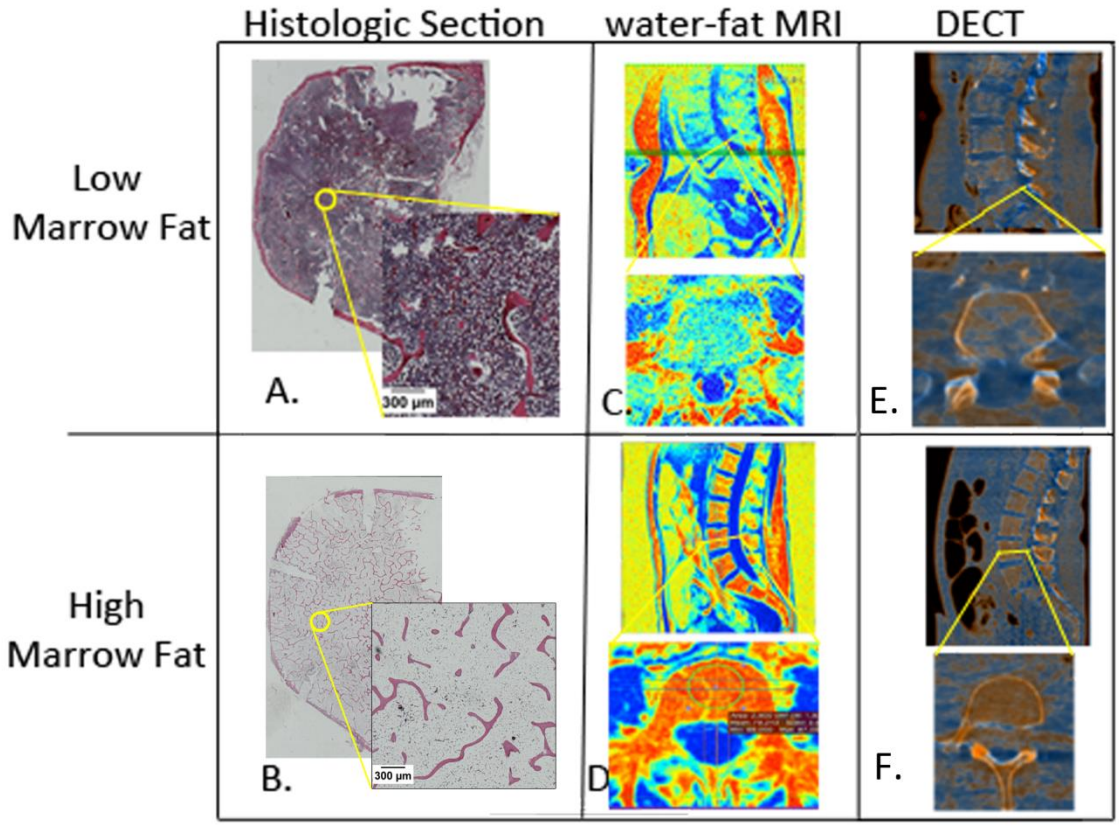

Figure 4-1. Multi-Modality Co-registration between histologic examination and *in vivo* imaging. Two vertebral bodies analyzed: top row is representative case of lower marrow fat and bottom row is higher marrow fat. A. & B. axial section of whole vertebral body with H&E staining. Void spaces of adipocytes were contoured by threshold and artifacts were removed at the discretion of the investigator. C. & D. water-fat MRI images of lumbar vertebrae and example of ROI placement. E. & F. DECT images reconstructed to highlight marrow fat intensities. For imaging modalities, red represents high marrow fat concentration.

The vertebral bodies were cut with a DELTA PEC bench band saw (Chang Type, Taiwan) to remove superior and inferior aspects and keep a 5mm section. Taking a histologic section from the center of the vertebral body ensured that the AV/TV was taken from a representative section of the imaging ROI. These sections were decalcified (Formical-2000, Decal Chemical Corp., New York, USA) (20x volume per sample) until the

cortical bone was completely demineralized. The sections were cut mid-sagittally to make left and right halves. Each vertebral half was then embedded in paraffin wax and stained by the H&E staining method. Eight vertebral bodies midsections were processed whole instead of being cut in half so that matching ROIs could be analyzed (Figure 4-1A & B).

4.2.4. Histology image tile procedure

A full digital image of each vertebrae half was produced by image tiling with a Nikon AZ100M Macro Fluorescence Scope (Nikon Corporation, Tokyo, Japan) with a color camera at 4x magnification. The cellular components of the produced images were then analyzed using ImageJ [49]. The scale was calibrated to 512 pixels/mm and the images were converted to an 8-bit gray scale. An approximately 2 mm diameter region of interest in each vertebra half was selected and areas of high artifact were avoided. A threshold was applied to identify adipocytes as void spaces remaining from the H&E staining process. Non-adipocytic void spaces, commonly seen as artifacts in H&E staining, were excluded from this selection process at the discretion of each user. Adipocyte volume per tissue volume (AV/TV) was calculated for each half. The AV/TVs for both halves were averaged together.

In order to test variability, histologic examinations were also performed at 0.5 cm superior and 0.5 cm inferior to the middle in three vertebral bodies. Also, two investigators examined the histology images for the marrow fat ratio in order to test inter-user variability.

4.3. Results

DECT-derived yellow marrow fraction estimations were calculated for all 25 lumbar vertebrae in the five donors. YMF ranged from 0.07 to 0.91 for the lowest and highest fat signal, respectively. For wfMRI-derived signal fat fraction, values could only be determined for 20 lumbar vertebrae; one subjects had poor signal to noise ratio above L5 and another had a poor signal to analyze L1. Values ranged from 0.22 for less fatty marrow to 0.79 for the highest sFF.

The AV/TV of 21 lumbar vertebrae ranged from 0.18 to 0.75 with a mean (SD) of 0.36 (0.18). Vertebral bodies take from the same cadaver showed much less diversity as seen by standard deviations of AV/TV between 0.03 and 0.07. For the three vertebrae that were analyzed at three levels within 1 cm, the average coefficient of variation between the sections was 0.08. There was a high correlation between the two users, r = 0.99.

17 vertebral bodies were scanned with both DECT and wfMRI and then processed for H&E examination. There were moderate correlations between the AV/TV and the results of DECT and wfMRI (r = 0.80 and 0.77, respectively) (Figure 4-2A). A

higher correlation was seen between the two imaging modalities with similar ROIs than with histology (r = 0.88) (Figure 4-2B).

4.4. Discussion

Current clinical practice of marrow fat assessment typically involves an invasive and painful bone marrow biopsy of the posterior iliac crest. However, this method does not give an accurate picture of the heterogeneity that is present in bone marrow throughout the body. For the first time, AV/TV quantifications taken from vertebral bodies have been correlated with results from dual energy CT (DECT) and wfMRI modalities. Both DECT and wfMRI were able to estimate yellow marrow fat fractions as validated by AV/TV in 17 coregistered samples.

Although bone marrow adipocyte parameters have been used to quantify marrow fat from trephine biopsies of the iliac crest [88-91], it is not commonly used on H&E stains of intact vertebral body cross-sections. In our small sample size, we found that inter-subject AV/TV can vary by nearly 60%, and even different intra-subject sites varied by as much as 40%. This high variability could be due to the diverse treatment effects each individual received prior to death or just a reflection of the true heterogeneous makeup of bone marrow within individuals. The technique used to estimate AV/TV is highly reproducible if proper instruction is given for estimating adipocyte grayscale threshold.

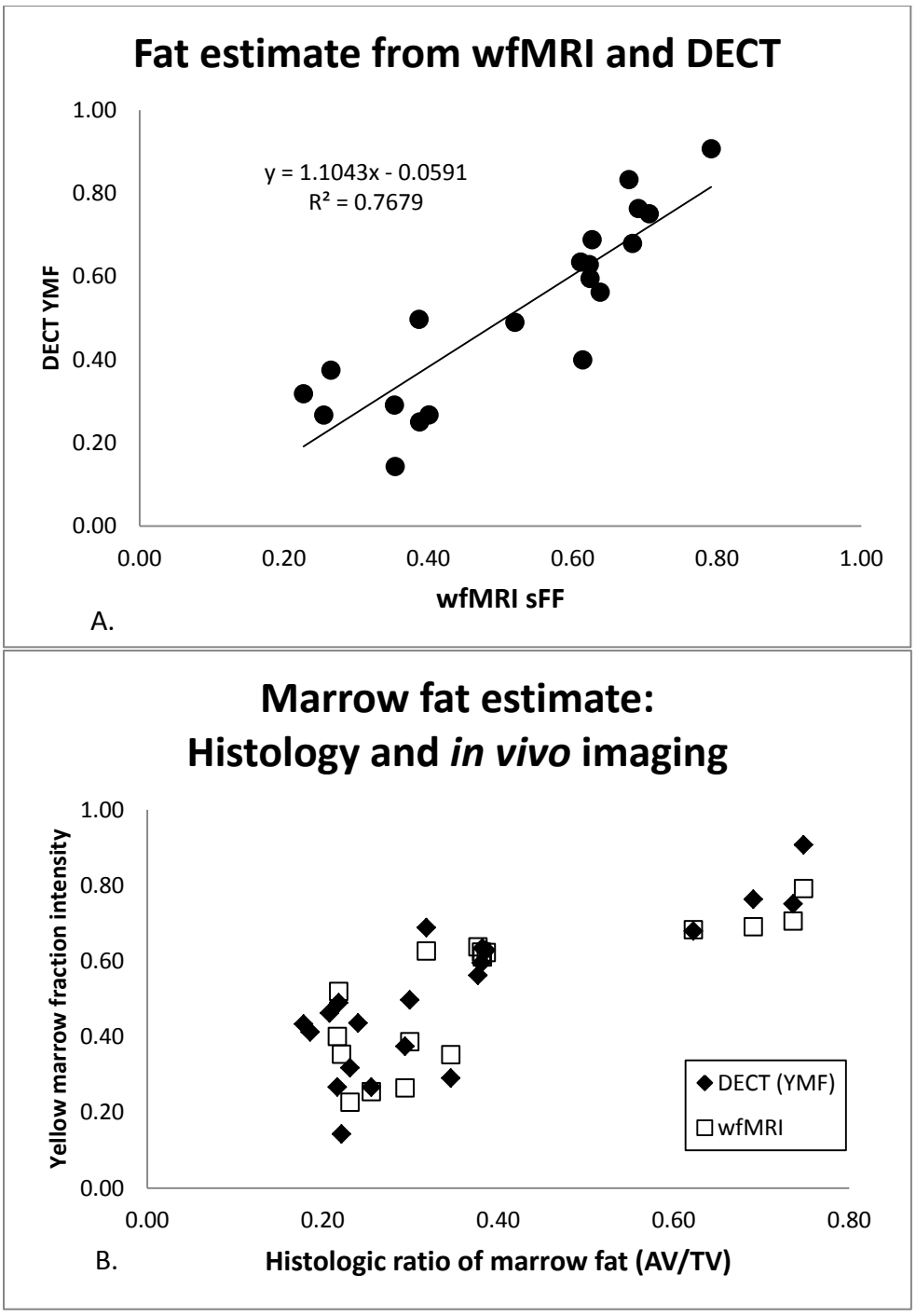

Figure 4-2. Marrow fat estimation from histology and *in vivo* imaging modalities. A) 17 vertebral bodies were imaged with DECT and MRI and then processed for H&E examination. Results of the imaging are compared with histologic adipocyte volume per tissue volume. B) Correlation between the marrow fat estimation results from two non-invasive imaging techniques.

4.4.1. Clinical implications

With the increased commercial availability of dual energy CT scanners and recent proof of acceptable dose exposure [69], DECT is becoming more prevalent in hospitals and treatment centers. The ability to measure marrow fat at any cancellous bone site could provide a pathway for studies to monitor changes, *in vivo*, using DECT. It may also be useful in radiation therapy treatment planning where targeting of active bone marrow would reduce the radiation treatment exposure to healthy tissue. DECT can easily be adapted in the treatment facilities (e.g. radiation oncology departments) where whole body PET/CTs are commonplace and single energy CT imaging is commonly performed to monitor cancer survivors.

4.4.2. Limitations

The subjects in this study were all given cytotoxic treatments within the last 6 months before death which is known to affect the bone marrow composition. Investigations into the true variation in the average human body would need this examination repeated with a more controlled population. However, this study was focused on validating marrow fat fraction estimation from *in vivo* imaging techniques. Decomposition processes may introduce some bias into the data. However, these processes are likely to be negligible, as bone marrow from recently deceased individuals is commonly transplanted to immunocompromised patients.

4.4.3. Conclusion

In conclusion, cancellous bone regions were examined by histology and co-registered *in vivo* clinical imaging. Marrow fat fraction intensities taken from imaging were validated with histologic quantification of adipocyte prevalence. This may be able to monitor bone health of individuals who have undergone cytotoxic treatment, especially the cancer survivor.

CHAPTER 5: *IN SITU* ASSESSMENT REVEALS SKELETAL-WIDE HETEROGENEITY OF HUMAN CANCELLOUS BONE

5.1. Introduction

Although skeletal health is most often clinically assessed by measuring the bone mineral density (BMD) of the lumbar spine and proximal femur, this common clinical practice assumes homogeneity between these sites and the entire skeleton. Our previous work in a mouse model has demonstrated that the skeleton is heterogeneous and has an immediate response from treatments such as radiation and chemotherapy [92]. However, no studies have been performed to assess the skeletal-wide BMD variation in humans. Several studies have shown that the majority of fractures occur outside of the axial skeleton [93-95]. According to Amin et al., fractures in the spine and proximal femur comprise only 30% of fragility fractures [96]. Therefore, a method of imaging the entire skeletal system might improve the ability to identify and treat patients at high risk of fractures.

Recently, cancellous trabecular microarchitecture within a single vertebral body was found to be heterogeneous at different sections [77]. If cancellous bone is inhomogeneous within an individual vertebrae, then heterogeneity of cancellous bone along the entire skeleton could also exist. Current methods of assessing bone health (i.e. Dual-energy X-ray absorptiometry, DXA) superimpose cortical and cancellous bone, thereby masking true cancellous bone characteristics.

For this study, we separate the term 'cancellous' bone into two regions, a calcified trabecular matrix and a marrow space containing a ratio of red to yellow bone marrow. Similar to the ratio of cancellous to cortical bone, the ratio of red to yellow bone marrow also varies from site to site [97]. As mentioned in Section 1.3, accurate BMD assessment can be problematic when using traditional methods (i.e. DXA or Quantitative Computed Tomography (QCT)) which do not correct for marrow composition [21, 98, 99]. Recent improvements in CT scanners, including dual energy, large bore, and larger couch travel, have provided accurate and efficient in investigations of the whole body, including quantification of marrow fat [100].

The primary goal of this study was to quantitatively image the entire skeleton in order to characterize the heterogeneity of cancellous bone. The secondary goal was to evaluate whether marrow-corrected BMD (mcBMD) (derived using DECT) had similar characteristics to uncorrected BMD (derived using QCT). Finally, we investigated potential differences in skeletal heterogeneity between subjects with and without a history of cancer treatment (i.e. chemotherapy).

5.2. Methods

5.2.1. Subjects

Over a 10 month period, twenty recently deceased human donors were accepted in the imaging study. All donors or their next of kin/authorizing person consented to donate her bodies to aid in anatomy education and research in accordance with the Minnesota Darlene Luther Revised Uniform Anatomical Gift Act. Donors were

all Caucasian women between the ages of 40 and 80 years old, less than 190 cm tall, and were imaged within 24 hours postmortem. The height restriction ensured that the body could fit within the longitudinal length of the CT scanner. In order to normalize mcBMD values from the 20 subjects, an age correction factor was taken from a recent investigation on the effects of age on cancellous volumetric BMD [101]. Since cancellous bone changes much more drastically with age than combined cortical and cancellous, a correction based on DXA values would not be accurate and, in fact, were less drastic than volumetric BMD correction (data not shown). The average applied age correction was approximately 10% with a standard deviation of 27%.

Two groups of donors were assessed in this study; those treated with chemotherapy (n=10) or controls (n=10) without bone afflicting conditions (e.g. not treated for cancer, hyperthyroidism, or Paget's disease). Donors with history of cancer treatment were included only if their last round of chemotherapy was less than a year before death.

5.2.2. Imaging

Within 24 hours of death, bodies were taken to the radiology department at the University of Minnesota Medical Center – Fairview for whole body dual energy CT scanning. Although the term "*in situ* imaging" is accurate for the assessment of cadavers, dual energy computed tomography (DECT) imaging can be used *in vivo.* Imaging was obtained using a Siemens® SOMATOM Definition Flash Dual Energy CT scan

(Siemens Healthcare, Forchheim, Germany) at energies of 80kVp, 500mm SFOV, and 306-308mAs for Source A, and 140kVp, 328mm SFOV and 110-150mAs with a tin filter for Source B. During imaging, subjects were placed in a supine position with arms to the side. The SOMATOM DECT unit was calibrated for both energies using the Mindways Software, Inc. (Mindways Software, Austin, TX, USA) QCTPro calibration Phantom. The table height was varied to ensure that the patient was in the center of the imaging field, regardless of body size. A calibration was performed for each table height.

5.2.3. ROI analysis

Using software developed by Mindways Software, Inc. (Austin, Texas, USA) and anatomical landmarks, regions of interest (ROIs) were placed in the same location on the 80kVp and Sn140kVp CT scans. Twenty-three cancellous bone locations were analyzed (Figure 5-1) which included: the skull, twelve sites from the spine, two from the arm, three from the hip, two from the knee, and three from the ankle/ foot.

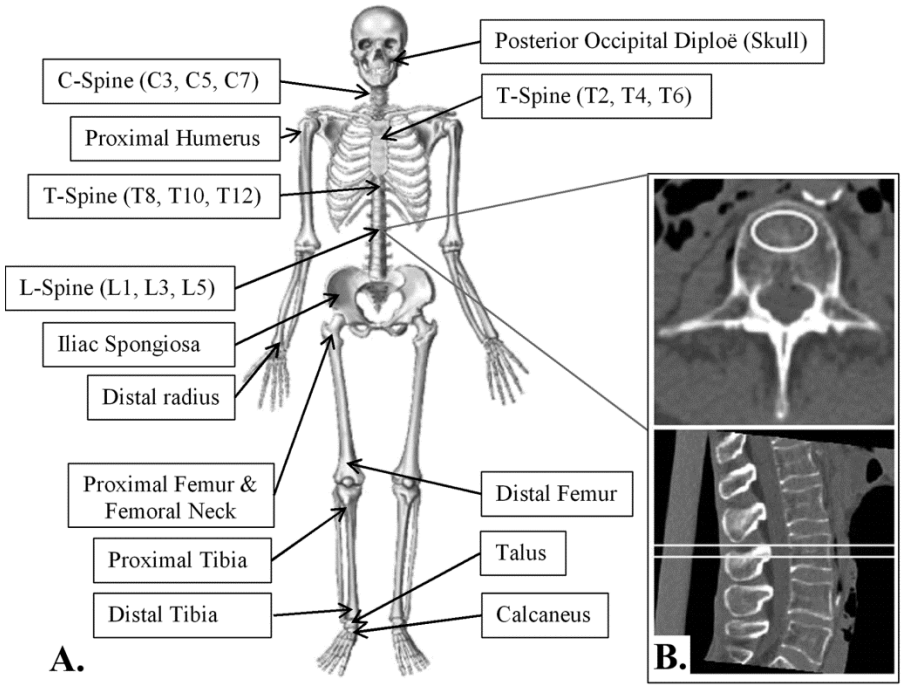

Figure 5-1. 23 Regions of Interest representing areas of analyzed cancellous bone with representative case for ROI Placement of L3

The size of each ROI depended on the bone being measured but ranged from a cylinder of 20mm^2 x 3mm for the posterior occipital diploë ("skull") to 300mm^2 x 9mm for the lumbar spine. Care was taken to exclude any area where a fracture had occurred, especially in a vertebral body. Similarly sized ROIs were placed at each skeletal site for all donors. Vertebrae were analyzed at the center of the vertebral body in the superior-inferior axis.

5.2.4. Basis Material Composition

A commercially available CT calibration phantom (Mindways Software, Inc. Austin, TX) was used in each imaging procedure. This phantom was composed of different rods of known water and K_2HPO_4 concentrations. When scanned with two

different energies in the diagnostic range, the x-ray attenuation of biologic tissue can be described by the linear combination of the x-ray attenuation properties of these two materials [17, 102]. Using the publically available XCOM database to estimate energy-dependent, mass attenuation coefficients, the average atomic composition for basis materials can be estimated [103]. The International Commission on Radiation Units and Measures has documented average atomic compositions of adipose tissue, yellow marrow, and red marrow (0.91 g/cm3, 0.93 g/cm3, and 1.03g/cm3, respectively (ICRU publication 46))[104]. When combined with XCOM, these values were used to derive the basis material compositions in our ROIs. Bone mineral density values can then be corrected for marrow composition at each skeletal site. Further details of basis material decomposition are part of another submitted manuscript.

5.2.5. Statistics

Mean QCT-derived BMD and mcBMD values were determined at each skeletal site for both control donors and donors treated for cancer. Significant differences in QCT-derived BMD and mcBMD were assessed by a paired t-test for each skeletal site. The mcBMD results for each skeletal site were correlated to every other site, by control or cancer group, using the Pearson Product-Moment Correlation Coefficient. To measure the significance of differences seen between mean mcBMD values of cancer and control donors, two sample t-tests and F-tests were performed at every skeletal site.

5.3. Results

The average age for all subjects was 62 years (range, 40-80 years). The mean (SD) height and weight for subjects was 165 cm (7 cm) and 63kg (20 kg), respectively resulting in a BMI of 23.0 (6.4 kg/m^2). Causes of death included cancer (n=11 (one cadaver was never treated)), Parkinson Disease (n=2), chronic obstructive pulmonary disease (n=2), hepatitis (n=2), sudden cerebrovascular accident (n=2), and heart failure (n=1). Location and extent of disease in the cancer-treated group included: Breast cancer (n = 3), Ovarian/endometrial cancer (n = 3), urinary tract cancer (n = 2), tumor of the epiglottis (n = 1), and recurrent Chronic Lymphocytic Leukemia (n = 1) malignancies. One subject, from the cancer-treated group, sustained a proximal femur fracture approximately one month before death but was never treated, while another donor, from the control group, had prior bilateral knee replacement and shoulder reconstructive surgery. The high density material and resulting streak artifact made assessment of those regions unattainable in those two subjects.

For the 23 skeletal sites, the average BMD using 140kVp QCT corrected for age was 145 mg/cm^3, and ranged from 835 mg/cm^3 for the skull to -52 mg/cm^3 for the proximal humerus. Differences between BMD values for 80kVp and 140kVp correlated well (r = 0.91). Figure 5-2 compares BMD results from the 140kVp QCT dataset to the marrow-corrected DECT dataset.

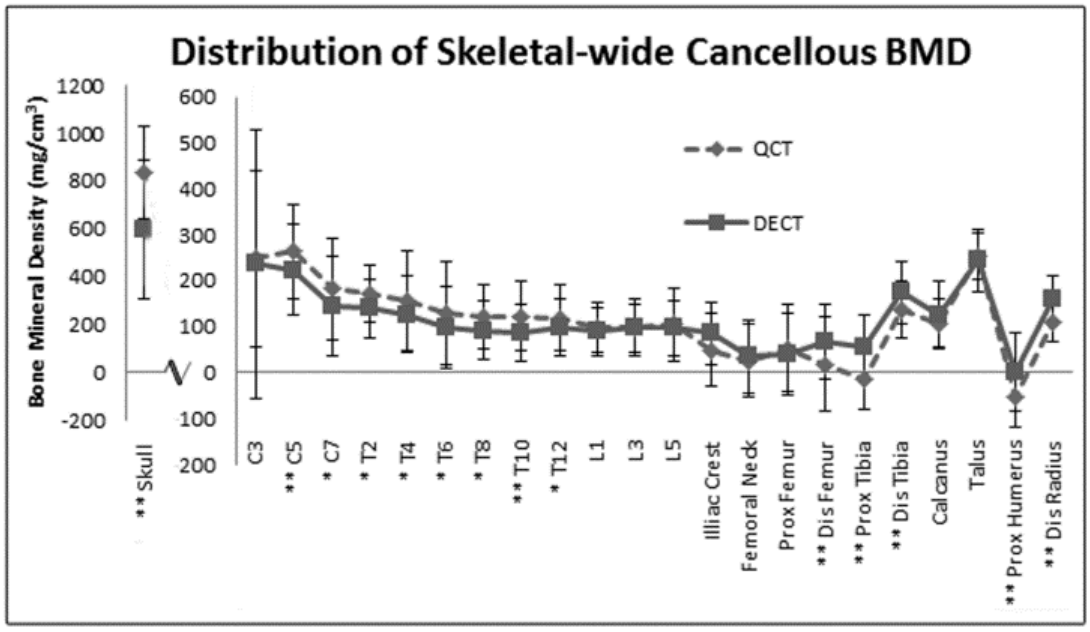

Figure 5-2. Cancellous Bone Mineral Density distribution for 23 skeletal sites (skull separately).

Notice at most vertebral sites, the BMD values are higher when marrow is left uncorrected (as assessed by QCT) than when corrected (as assessed by DECT) and vice versa for sites more caudal (e.g. tibia). At 14 of the 23 skeletal sites, the average difference between QCT-derived BMD and mcBMD was significant at the 0.10 level with a similar numbered amount of sites (12) having a Pearson correlation of $r > 0.7$. McBMD at each skeletal site also correlated well (average pairwise correlation $r > 0.6$) with other sites except for the femoral neck and proximal humerus (Figure 5-3).

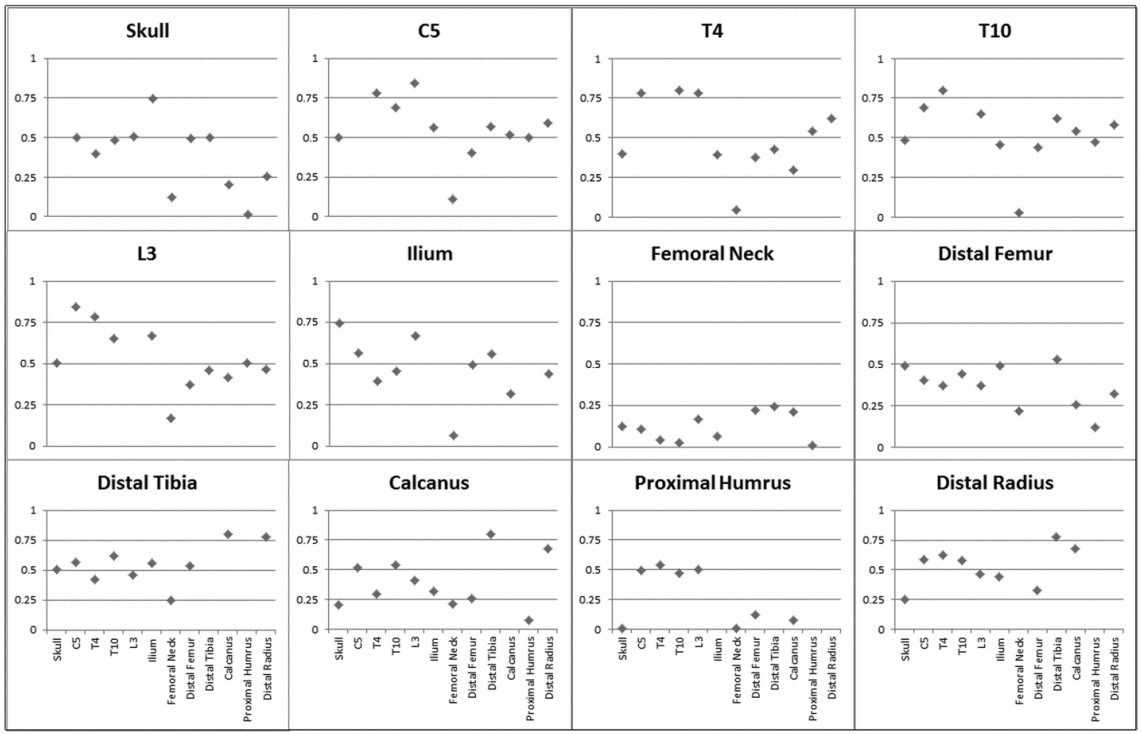

Figure 5-3. Average correlation between representative skeletal sites for marrow-corrected BMD.

These two sites were also the least dense with a mean mcBMD of 35 mg/cm^3 and 2 mg/cm^3, respectively. Excluding the skull, the average (SD) mcBMD derived by DECT was 114 mg/cm^3 (67 mg/cm^3) with the densest site being the talus (244mg/cm^3). We also observed a gradual decline in mean mcBMD in the axial skeleton from the top of the spinal column to the bottom (236 mg/cm^3 for C3; 96 mg/cm^3 for L5). Local differences in mcBMD were also seen within individual bones such as the femur and tibia. Cancellous mcBMD was lower in the proximal femur than the distal femur (39 mg/cm^3 and 66mg/cm^3, respectively), and significantly lower ($p < 0.001$) in the proximal tibia than distal tibia (54 mg/cm^3 and 174mg/cm^3, respectively).

Separating the marrow- and age-corrected results of the cancer and control groups showed intra-site mcBMD similarities. Statistical tests of differences of the mean or variance between cancer and control donors showed no mcBMD differences at most regions. The only exceptions were C7 and the ilium, which had a larger variance in the control group ($p = 0.039$ and 0.031, respectively), mostly due to a high mcBMD value in a control donor. All other tests had $p > 0.1$, suggesting that, on average, the cancer and control groups had similar mcBMD. However, a higher average pairwise correlation between other skeletal sites was seen in the controls ($r = 0.61$ and 0.33, respectively) (Figure 5-4).

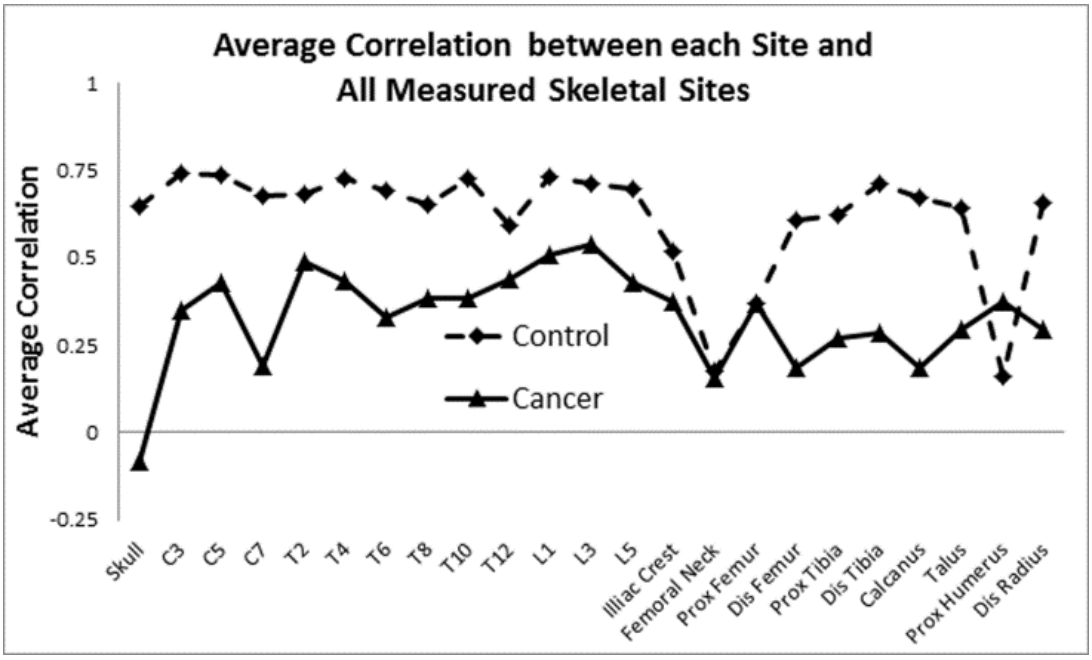

Figure 5-4. Mean correlation in mcBMD between 23 skeletal sites. Correlation coefficient was calculated for the mcBMD of each individual site vs the 22 other sites. Averages for control subjects vs cancer subjects are compared.

This shows that while control and cancer groups had similar mcBMD on average, the control group exhibited more consistent relationships among sites within individual patients. We noted that skeletal sites adjacent to each other had higher correlation in mcBMD than skeletal sites distant to one another (e.g. C3-C7 versus C3-distal tibia, respectively). More details can be found in the supplemental data.

5.4. Discussion

One of the most critical misconceptions in bone health today is the assumption that the entire skeletal system can be represented within a single biopsy or the uncorrected BMD measurements of a few sites. However, previous studies have found more than 70% of fractures occurred at locations other than the lumbar spine and hip [96, 105]. Our study documents common heterogeneity of cancellous bone throughout the skeleton, with higher bone mineral density in the cranial and caudal sections and lower density at the midline (i.e. hip and pelvis). Even individual bones had differences in mcBMD, such as seen between the proximal and distal ends of the tibia and femur. We compared our data to the fracture incidence location by Amin et al. We found a small inverse correlation between average mcBMD values for each skeletal site and fracture incidence location ($r = -0.25$). This is the first reported comparison of skeletal-wide bone mineral density heterogeneity with fraction incidence locations. Although not a high correlation, other factors, such as cortical bone integrity and structure, may also influence facture incidence.

The correlation between QCT-derived BMD and mcBMD was high even though there were significant differences between the two. The pattern of heterogeneity between the axial skeleton and bones of the limbs was apparent in both modalities. A decreased average correlation between skeletal sites suggests a disruption in mcBMD heterogeneity due to a systemic effect of cancer treatment. Correcting for marrow composition can provide a more accurate estimate of the osseous density within a bone.

There are several explanations regarding the cause of cancellous bone heterogeneity. As well as structural support for mechanical motion, the skeleton is also an optimal site for calcium and mineral storage. The trabecular matrix can rapidly store and reabsorb minerals due to a high surface area. However, as humans age the need for rapidly accessible minerals decreases while the need for structural support remains. Perhaps this explains why the young have a higher ratio of vertically to horizontally oriented trabeculae than older individuals [106]. In addition to mechanical stress, the epigenetic postcode can also affect the rate of remodeling at different cancellous sites throughout the skeleton. We suggest that heterogeneity of mcBMD in the skeleton is due to combination of each skeletal site's mechanical stress and bone cell lineage along with the person's age.

To our knowledge, this is the first study to image the entire skeleton *in vivo* and correct for marrow composition using advanced computed tomography. Higher correlation of more adjacent vertebral sites is a finding similar to a 2011 study which

imaged the thoracic and lumbar spine in over 1,000 subjects [78]. This supports the theory that skeletal sites retain a genetic postcode that unique affects different regions of the body. Previous investigations attempted to quantify skeletal heterogeneity for a few specific skeletal sites in terms of bone ash weight [107], histologic examination [108], or micro-CT [80]. However, none of these investigations presented an *in vivo* technique for assessment of cancellous bone heterogeneity.

Chemotherapy is reported to adversely affect bone and bone marrow in clinical studies [109-111]. Less correlation between control and cancer-treated groups may be due to unequal damage to different skeletal regions due to cytotoxic treatment (e.g. chemotherapy and radiation). Structural properties as well as marrow content vary across the skeletal system and may therefore have different skeletal effects from cancer treatment.

Monitoring changes to the heterogeneity of cancellous bone might identify sites with a higher rate of bone turnover that are more prone to fracture. It may provide the ability to create a predictive model to estimate what the average value of a certain bone should be, compared to the rest of the skeleton. Deviations from the predictive model in individual patients could highlight areas where local disease might be present. It might also be used to monitor changes in skeletal health resulting from chemotherapy, radiation therapy or disease progression. Although CT imaging increases radiation exposure to patients, whole body CT scans are already performed as part of a positron emission tomography (PET)/CT and during some radiation therapy treatments. To date,

such images are taken with single energy CT and only used for anatomical referencing. However, we expect PET studies to soon take advantage of reduced radiation exposure from DECT scans [112-114] and be able to monitor bone health.

5.4.1. Limitations

The present study was a feasibility study and did not have a high sample size. We limited participants to donors who had pre-arranged anatomical donation contracts with the University of Minnesota Bequest Program. This happened to result with only Caucasian women being enrolled in the study. Also, the age correction used in this study was taken from a QCT publication examining the effect of age on the thoracic and lumbar vertebrae and did not correct for marrow composition or provide different corrections for all skeletal sites. Similar errors would be apparent in DXA, but even more so since this modality does not separate the thick exterior cortical bone from the interior cancellous bone. For the cancer-treated patients, there were uncertainties in treatment regimen because of patient grade, response, etc. as it was not a controlled study. However, the goal of this publication was to be a feasibility study.

5.4.2. Bone Mineral Density Heterogeneity Index Model

A value, termed Heterogeneity Index number, can be calculated by normalizing the function of average mcBMD for each skeletal site to a single site (e.g. T2). Thus, any site could be used in a linear calculation to estimate the mcBMD of any other site. For this study, T2 was used to test accuracy of the SEDD model. Measured mcBMD values

of cancer subjects at every site excluding the skull were compared to their estimated mcBMD values calculated from only the T2 value.

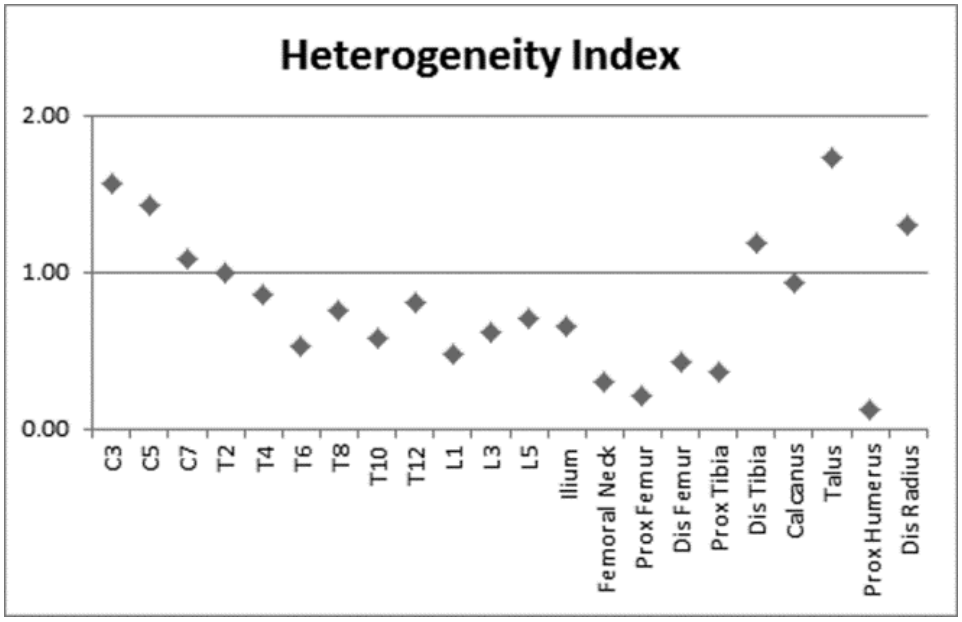

Figure 5-5. The heterogeneity index is presented for each of 22 skeletal sites (excluding the skull). Results are the average marrow corrected bone mineral density values from ten control subjects. Interestingly, heterogeneity was similar in adjacent bones. Additionally, there was greater heterogeneity in the superior versus inferior (cervical versus lumbar) spine. Heterogeneity was also higher toward the skull and feet, and lower in the mid-body.

The Heterogeneity Index normalized to T2 is shown in Figure 5-5. An empirical model was created which utilized the Heterogeneity Index to estimate the skeletal-wide bone mineral density distribution (SEDD) from just one measured site (Figure 5-6a). Results of skeletal mcBMD estimation from the 2nd Thoracic vertebrae of cancer donors using the SEDD model are compared to their measured values in Figure 5-6b. The average measured and estimated mcBMD values were correlated very well, r=0.95. T6

and L1 were the only estimated skeletal sites that were not significantly different ($p > 0.1$) from measured values and largely due to a single donor.

Bergmann et al. showed a variation in the rapidly exchangeable calcium pool between different skeletal regions. We did find a moderate correlation between their results and our heterogeneity index ($r = 0.65$). This indicates the model of bone remodeling may have similarities with cancellous mcBMD as measured by DECT. However, their method was limited by the technology of the day and could not separate cancellous bone from cortical, much less individual bones.

The SEDD model has the potential to be a clinically relevant prognostic tool. Monitoring changes to the heterogeneity of cancellous bone might identify sites with a higher rate of bone turnover that are more prone to fracture. It may provide the ability to estimate what the average value of a certain bone should be compared to the rest of the skeleton. The SEDD model could highlight areas where local disease might be present. It might also be used to monitor changes in skeletal health resulting from chemotherapy, radiation therapy or disease progression. Although CT imaging does increase radiation dose to patients, whole body CT scans are already performed as part of a positron emission tomography (PET)/CT and during some radiation therapy treatments. To date, such images are only used for anatomical referencing and not for monitoring bone health.

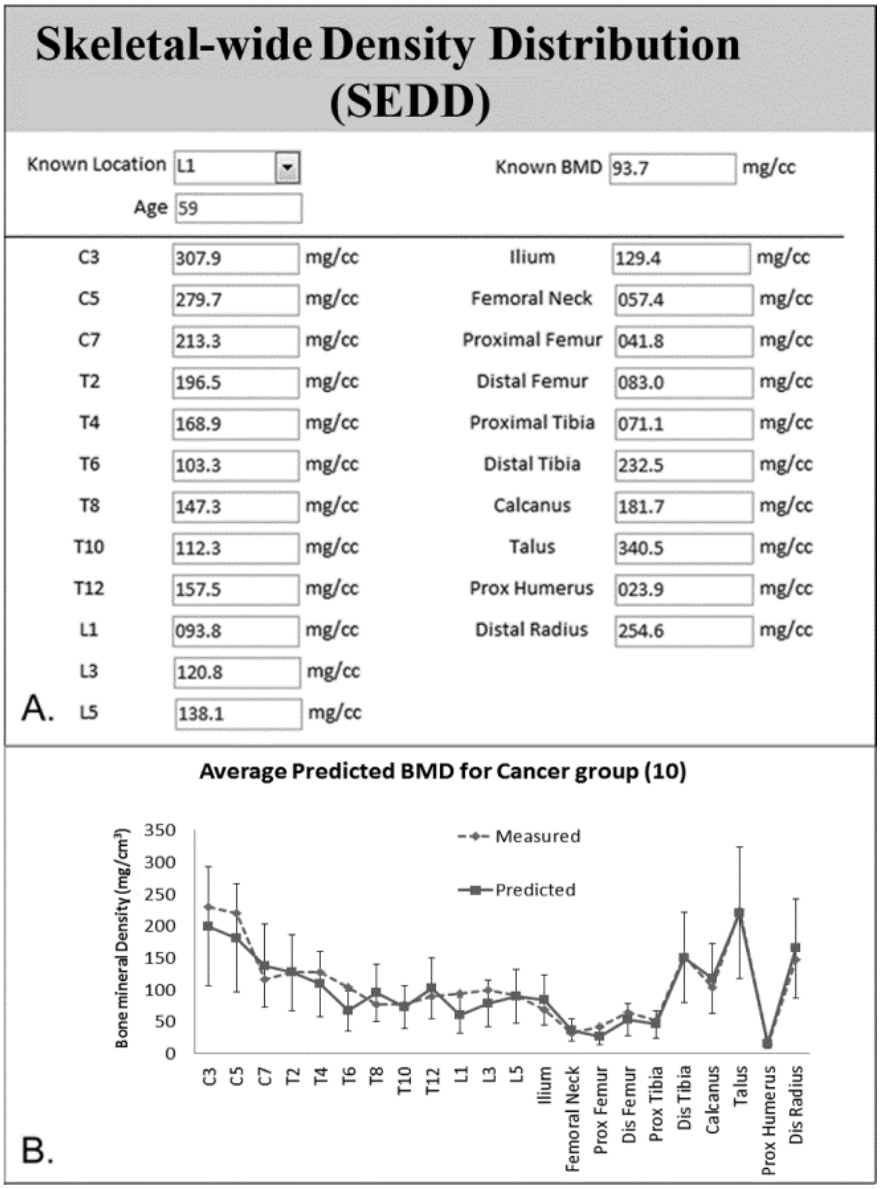

Figure 5-6. Prediction of marrow-corrected cancellous Bone Mineral Density (mcBMD) values from a single measured value. A) Application of the skeletal-wide estimated density distribution (SEDD) model. Using the relationship between the average cancellous mcBMDs from all clinical sites of control subjects, a model was developed to estimate mcBMD for the entire skeleton from just one site. All values were corrected for age and marrow composition. If given a measured (known mcBMD) value of any test site (Known location), mcBMD values of 22 skeletal sites can be estimated. B) 10 cancer-treated donors were imaged with whole-body DECT using the SEDD model. The measured mcBMD value of the L1 from 10 cancer treated donors was used to estimate the 21 other skeletal sites. Mean predicted (95% confidence level) and measured values

(SD) are shown. Only the T2 and L1 had significant differences between measured and estimated mcBMD ($p < 0.1$, t-test). A high correlation was seen between the average predicted and measured values for the donors ($r = 0.95$).

Although Samelson et al. only imaged the lower thoracic and lumbar vertebrae, we found their observed difference between the trabecular BMD of the T-spine and L-spine was within 3% to our SEDD model (94% vs 91%, respectively) [101]. However, their study did not correct for marrow composition. We further wanted to test our model using images from a DECT feasibility study. The abdomen and pelvis of 27 subjects enrolled in a clinical trial were imaged using DECT [115]. L5 and femoral neck mcBMD values were predicted from measured L3 values (Figure 5-6). The average predicted mcBMD was accurate to within 7% and 19% of the measured value for L5 and the femoral neck, respectively. A better correlation was seen between measured and predicted L5 than femoral neck (0.50 and 0.12, respectively).

5.4.3. Conclusion

Bone mineral density varies among cancellous bone sites along the entire skeleton. With the ability to correct for marrow composition, DECT imaging of the entire human body can accurately assess cancellous mcBMD heterogeneity. The trend of cancellous BMD among skeletal sites was similar for QCT and DECT. However, marrow correction did reveal dynamic differences in some skeletal sites. No significant differences were seen between mean mcBMD values for control donors and those treated for cancer, although correlation between skeletal sites was weaker in the cancer

group. These findings suggest potential for developing a skeletal heterogeneity model in further prospective studies, which could predict individual mcBMD values based on sites elsewhere in the skeleton, and identify abnormalities in patients who deviate from the model.

CHAPTER 6: **CONCLUSION**

6.1. Summary and general conclusions

Skeletal health is becoming a critical subject with the aging and cancer survivor population. Fractures cause a large economic burden and their effect can range from restricted lifestyle to death. An important area of research involves developing new biomarkers in order to assess the health of bones. Methods of assessing bone health *in vivo* have the potential to monitor changes at critical locations without the need for invasive biopsies or large mouse populations.

In this work, several modern modalities were explored and utilized in order to investigate the relationship between bone marrow, BMD, and their heterogeneity throughout the whole mammalian body. A major strength of *in vivo* imaging in pre-clinical and clinical trials is highlighted in the ability to repeatedly measure the same site for treatment effects in the body. To that aim, it is necessary to characterize each modality in terms of imaging parameters and operating costs. The modalities in this document are relatively new techniques. Therefore, there is not much literature regarding parameters for pre-clinical *in vivo* imaging or utilizing DECT for longitudinal studies. Therefore, the work presented here aims to provide information on the effect of bone afflicting disorders both locally and systemically.

When working with the murine model, it is possible to measure simulated treatment conditions and monitor changes that would be experienced by a patient

undergoing cancer treatment. Optimized micro-CT parameters provide quality images that are sufficient for examining longitudinal changes in the trabecular bone of mice.

Micro-CT can also be useful in monitoring both local and distal skeletal sites in response to radiation injury [116]. This technique may permit investigations into the multi factorial communication pathways between the two active tissue components in skeletal metabolism. After dual isotope analysis, there appears to be some functional skeletal heterogeneity among marrow and calcified tissues. Exposure to localized radiation causes different longitudinal changes in marrow metabolism and mineral remodeling both in the exposed area and in the abscopal skeleton.

Technological advancements in dual energy CT have made it a modality capable of simultaneously quantifying the two compartments of cancellous bone (i.e. the calcified trabecular matrix and the marrow compartment). However, in order to prove marrow composition, it is necessary to confirm DECT with co-registered histologic examination of cancellous bone. We have provided marrow fat fraction intensities taken from both DECT and commonly accepted water-fat MRI. Results from both modalities had a strong relationship with histologic quantification of adipocyte prevalence ($r > 0.75$). DECT has the ability to monitor the proliferation marrow fat without the need for invasive biopsies or an expensive wfMRIs.

Utilization of DECT and wfMRI in our clinical trial confirms that DECT can measure changes in both MF and mcBMD after cancer treatment. We found that MF

increased significantly more following radiation and chemotherapy, relative to treatment with an oophorectomy alone. Therefore, it can be concluded that loss of ovarian function alone cannot explain the increased MF in cancer patients. We also challenge current dogma and showed that the cancer survivors in our study experienced large increases (9-32%) in MF over one year.

Another dogma being challenged with this work is the assumption that the entire skeletal system can be represented within a single biopsy or the BMD measurements of a few sites. We have shown that cancellous bone is heterogeneous throughout the skeleton with assessment of the whole body using DECT imaging. A higher bone mineral density was seen in the cranial and caudal sections and lower density at the midline (i.e. hip and pelvis). Even individual bones had differences in marrow-corrected BMD, such as seen between the proximal and distal ends of the tibia and femur. We compared our data to the fracture incidence location and found a small inverse correlation between average marrow-corrected BMD values for each skeletal site and fracture incidence location ($r = -0.25$). This is the first reported comparison of skeletal-wide bone mineral density heterogeneity with fraction incidence locations.

6.2. Potential applications

6.2.1. Murine Study

The use of micro-CT/PET may be useful for monitoring local and distal skeletal sites in response to radiation injury. Using each mouse as its own control would significantly decrease the need for an inordinate number of mice. Combined with the

ability to image multiple mice in each scan, micro-CT/PET can be reasonably priced and still provide detailed information on both local injury to bone as well as the abscopal response from distant skeletal sites. Our initial work did find some functional skeletal heterogeneity among marrow and bone tissues. Molecular and biochemical mechanisms could still be further investigated.

6.2.2. Human Study

In our studies, we suggest that MF and mcBMD should be considered independently, which DXA and single energy quantitative computed tomography cannot do. Separating MF and mcBMD should be done especially when monitoring the adverse effects of cancer therapy. Future longitudinal studies in cancer survivors are needed in order to 1) determine how long increased MF persists following cancer therapy, 2) how changes in MF associate with changes in mcBMD, 3) whether serum adiponectin can be used to measure changes in MF, and 4) how MF changes correspond to risk of incident fracture.

Monitoring MF longitudinally with use of DECT can also become a significant area of research for investigators using MF as an early biomarker for osteoporosis. Monitoring the natural progression of red to yellow marrow as one ages could be used to alert healthcare providers if marrow composition is excessive for a given skeletal site.

Another future application of the work in this dissertation is monitoring the skeletal-wide heterogeneity of cancellous bone to identify sites with an unusually higher

rate of bone loss. Whole body DECT may able to create a predictive model to estimate what the average value of a certain skeletal site should be, compared to the rest of the skeleton. Deviations from the predictive model in individual patients could highlight areas where local disease might be present.

BIBLIOGRAPHY

1. Prevention, C.f.D.C.a. *Falls Among Older Adults: An Overview*. 2013 9/20/2013 [cited 2014 4/1/2014]; Available from: www.cdc.gov/homeandrecreationalsafety/falls/adultfalls.html.
2. Stevens, J.A., et al., *The costs of fatal and non-fatal falls among older adults.* Inj Prev, 2006. **12**(5): p. 290-5.
3. Nordin, B.E., *The definition and diagnosis of osteoporosis.* Calcif Tissue Int, 1987. **40**(2): p. 57-8.
4. Bernard, J.L., *[Diagnosis of osteoporosis].* Soins, 1991(554): p. 7-14.
5. *Assessment of fracture risk and its application to screening for postmenopausal osteoporosis. Report of a WHO Study Group.* World Health Organ Tech Rep Ser, 1994. **843**: p. 1-129.
6. Riggs, B.L., L.J. Melton, 3rd, and W.M. O'Fallon, *Drug therapy for vertebral fractures in osteoporosis: evidence that decreases in bone turnover and increases in bone mass both determine antifracture efficacy.* Bone, 1996. **18**(3 Suppl): p. 197S-201S.
7. Hodgson, S.F., et al., *Rates of cancellous bone remodeling and turnover in osteopenia associated with primary biliary cirrhosis.* Bone, 1993. **14**(6): p. 819-27.
8. Lloyd, E., et al., *Surface to volume ratios of bone determined by computer analysis of microradiographs.* Nature, 1968. **218**(5139): p. 365-6.
9. Kanis, J.A., *Osteoporosis*1994, Oxford ; Cambridge, Mass.: Blackwell Science. x, 254 p.
10. Bergmann, P., T. Paternot, and A. Schoutens, *Regional measurement of bone calcium accretion rate and exchangeable pool with a whole-body counter: method and studies in subjects without bone disease.* Calcif Tissue Int, 1983. **35**(1): p. 21-8.
11. Rawlinson, S.C., et al., *Adult rat bones maintain distinct regionalized expression of markers associated with their development.* PLoS One, 2009. **4**(12): p. e8358.
12. Bolan, P.J., et al., *Water–fat MRI for assessing changes in bone marrow composition due to radiation and chemotherapy in gynecologic cancer patients.* Journal of Magnetic Resonance Imaging, 2013.
13. Flohr, T., et al., *First performance evaluation of a dual-source CT (DSCT) system.* European Radiology, 2006. **16**(2): p. 256-268.
14. Ricci, C., et al., *Normal age-related patterns of cellular and fatty bone marrow distribution in the axial skeleton: MR imaging study.* Radiology, 1990. **177**(1): p. 83-8.
15. Moore, S.G. and K.L. Dawson, *Red and yellow marrow in the femur: age-related changes in appearance at MR imaging.* Radiology, 1990. **175**(1): p. 219-23.
16. Kricun, M.E., *Red-yellow marrow conversion: its effect on the location of some solitary bone lesions.* Skeletal Radiol, 1985. **14**(1): p. 10-9.
17. Goodsitt, M.M., et al., *The composition of bone marrow for a dual-energy quantitative computed tomography technique. A cadaver and computer simulation study.* Invest Radiol, 1994. **29**(7): p. 695-704.
18. International Commission on Radiological Protection. Task Group on Reference Man., *Report of the Task Group on Reference Man : a report*. ICRP publication1975, Oxford ; New York: Pergamon Press. xix, 480 p.

19. Blake, G.M., et al., *Effect of increasing vertebral marrow fat content on BMD measurement, T-Score status and fracture risk prediction by DXA.* Bone, 2009. **44**(3): p. 495-501.
20. Mazess, R.B., *Errors in measuring trabecular bone by computed tomography due to marrow and bone composition.* Calcif Tissue Int, 1983. **35**(2): p. 148-52.
21. Gluer, C.C. and H.K. Genant, *Impact of marrow fat on accuracy of quantitative CT.* J Comput Assist Tomogr, 1989. **13**(6): p. 1023-35.
22. Kalender, W., E. Klotz, and C. Suess, *Vertebral bone mineral analysis: an integrated approach with CT.* Radiology, 1987. **164**(2): p. 419-423.
23. Griffith, J.F., et al., *Vertebral bone mineral density, marrow perfusion, and fat content in healthy men and men with osteoporosis: dynamic contrast-enhanced MR imaging and MR spectroscopy.* Radiology, 2005. **236**(3): p. 945-51.
24. Yeung, D.K., et al., *Osteoporosis is associated with increased marrow fat content and decreased marrow fat unsaturation: a proton MR spectroscopy study.* J Magn Reson Imaging, 2005. **22**(2): p. 279-85.
25. Georgiou, K., B. Foster, and C. Xian, *Damage and Recovery of the Bone Marrow Microenvironment Induced by Cancer Chemotherapy-Potential Regulatory Role of Chemokine CXCL12/Receptor CXCR4 Signalling.* Current Molecular Medicine, 2010. **10**(5): p. 440-453.
26. Sacks, E., et al., *Bone marrow regeneration following large field radiation. Influence of volume, age, dose, and time.* Cancer, 2006. **42**(3): p. 1057-1065.
27. Rosen, C., et al., *Marrow fat and the bone microenvironment: developmental, functional, and pathological implications.* Critical reviews in eukaryotic gene expression, 2009. **19**(2): p. 109.
28. Schellinger, D., et al., *Bone marrow fat and bone mineral density on proton MR spectroscopy and dual-energy X-ray absorptiometry: their ratio as a new indicator of bone weakening.* AJR Am J Roentgenol, 2004. **183**(6): p. 1761-5.
29. Stevens, S.K., S.G. Moore, and I.D. Kaplan, *Early and late bone-marrow changes after irradiation: MR evaluation.* AJR Am J Roentgenol, 1990. **154**(4): p. 745-50.
30. McKinstry, C.S., et al., *Bone marrow in leukemia and aplastic anemia: MR imaging before, during, and after treatment.* Radiology, 1987. **162**(3): p. 701-7.
31. Sacks, E., et al., *Bone marrow regeneration following large field radiation. Influence of volume, age, dose, and time.* Cancer, 1978. **42**(3): p. 1057-1065.
32. Casamassima, F., et al., *Hematopoietic bone marrow recovery after radiation therapy: MRI evaluation.* Blood, 1989. **73**(6): p. 1677.
33. Rubin, P., et al., *Bone marrow regeneration and extension after extended field irradiation in Hodgkin's disease.* Cancer, 1973. **32**(3): p. 699-711.
34. Siegel, R., et al., *Cancer treatment and survivorship statistics, 2012.* CA: A Cancer Journal for Clinicians, 2012. **62**(4): p. 220-241.
35. Spowage, A.C., et al., *Development of characterisation methodologies for macroporous materials.* Journal of Porous Materials, 2006. **13**(3-4): p. 431-438.
36. Ritman, E.L., *Molecular imaging in small animals - Roles for micro-CT.* Journal of Cellular Biochemistry, 2002. **39**: p. 116-124.

37. Mulder, L., J.H. Koolstra, and T.M. VanEijden, *Accuracy of MicroCT in the Quantitative Determination of the Degree and Distribution of Mineralization in Developing Bone.* Acta Radiologica, 2004. **7**: p. 769-777.
38. Kinney, J.H., N.E. Lane, and D.L. Haupt, *In vivo, three-dimensional microscopy of trabecular bone.* J Bone Miner Res, 1995. **10**(2): p. 264-70.
39. Holdsworth, D.W. and M.M. Thornton, *Micro-CT in small animal and specimen imaging.* Trends in Biotechnology, 2002. **20**(8): p. S34-S39.
40. Peyrin, F., et al., *Micro-CT examinations of trabecular bone samples at different resolutions: 14, 7 and 2 micron level.* Technol Health Care, 1998. **6**(5-6): p. 391-401.
41. Du, L.Y., et al., *A quality assurance phantom for the performance evaluation of volumetric micro-CT systems.* Phys Med Biol, 2007. **52**(23): p. 7087-108.
42. Moya, U. and M. Brandan, *Parameterization of X-ray spectra appropriate for microCT scanners.* Nuclear Instruments and Methods in Physics Research: Part A, 2010. **613**: p. 152-155.
43. Khodaverdi, *Investigation of Different MicroCT Scanner Configurations by GEANT4 Simulations.* IEEE transactions on nuclear science, 2005. **52**(1): p. 188-192.
44. Shrimpton, P.C., D.G. Jones, and B.F. Wall, *The influence of tube filtration and potential on patient dose during x-ray examinations.* Phys Med Biol, 1988. **33**(10): p. 1205-12.
45. Duerinckx, A.J. and A. Macovski, *Polychromatic streak artifacts in computed tomography images.* J Comput Assist Tomogr, 1978. **2**(4): p. 481-7.
46. Storer, J., *Relation of lifespan to brain weight, body weight, and metabolic rate among inbred mouse strains.* Experimental Gerontology, 1967. **2**(3): p. 173-182.
47. Bouxsein, M.L., et al., *Guidelines for assessment of bone microstructure in rodents using micro-computed tomography.* J Bone Miner Res, 2010. **25**(7): p. 1468-86.
48. Magota, *Performance characterization of the Inveon preclinical small-animal PET/SPECT/CT system for multimodality imaging.* European Journal of Nuclear Medicine and Molecular Imaging, 2011. **38**: p. 742-752.
49. National Rasband, W.S., *ImageJ*, 1997-2011, U.S. National Institutes of Health: Bethesda, Maryland, USA.
50. Lenox, M., *Transmission Measurements using Iterative Conebeam Reconstruction on the Inveon DPET*, in *IEEE Nuclear Science Symposium Conference Record*2008. p. 4711-4717.
51. Cao, G., et al., *A dynamic micro-CT scanner based on a carbon nanotube field emission x-ray source.* Phys Med Biol, 2009. **54**(8): p. 2323-40.
52. Rossmann, K., *Point spread-function, line spread-function, and modulation transfer function. Tools for the study of imaging systems.* Radiology, 1969. **93**(2): p. 257-72.
53. Hui, S.K., et al., *Skeletal remodeling following clinically relevant radiation-induced bone damage treated with zoledronic acid.* Calcif Tissue Int, 2012. **90**(1): p. 40-9.
54. Ford, N.L., M.M. Thornton, and D.W. Holdsworth, *Fundamental image quality limits for microcomputed tomography in small animals.* Med Phys, 2003. **30**(11): p. 2869-77.
55. Thurner, P., F. Beckmann, and B. Muller, *An Optimization procedure for spatial and density resolution in hard X-ray micro-computed tomography.* Nuclear Instruments and Methods in Physics Research: Part B, 2004. **225**: p. 599-603.

56. Kapur, J.N., P.K. Sahoo, and A.K.C. Wong, *A New Method for Gray-Level Picture Thresholding Using the Entropy of the Histogram.* Computer Vision Graphics and Image Processing, 1985. **29**(3): p. 273-285.
57. Sahoo, P., C. Wilkins, and J. Yeager, *Threshold selection using Renyi's entropy.* Pattern Recognition, 1997. **30**(1): p. 71-84.
58. Visualization Sciences Group, F. *Avizo, 3D Analysis Software for Scientific and Industrial data*. 2014 June 13th, 2014]; Wherever three-dimensional data sets need to be processed, in materials science, geosciences, environmental or engineering applications, Avizo offers abundant state-of-the-art features within an intuitive workflow and easy-to-use graphical user interface.]. Available from: http://www.vsg3d.com/avizo/overview.
59. Laperre, K., et al., *Development of micro-CT protocols for in vivo follow-up of mouse bone architecture without major radiation side effects.* Bone, 2011. **49**(4): p. 613-22.
60. Jiang, Y., et al., *Application of micro-CT assessment of 3-D bone microstructure in preclinical and clinical studies.* J Bone Miner Metab, 2005. **23 Suppl**: p. 122-31.
61. Meganck, J.A., et al., *Beam hardening artifacts in micro-computed tomography scanning can be reduced by X-ray beam filtration and the resulting images can be used to accurately measure BMD.* Bone, 2009. **45**(6): p. 1104-16.
62. Baxter, N., et al., *Risk of pelvic fractures in older women following pelvic irradiation.* JAMA, 2005. **294**(20): p. 2587.
63. Guise, T., *Bone loss and fracture risk associated with cancer therapy.* The Oncologist, 2006. **11**(10): p. 1121-1131.
64. Ensrud, K.E., et al., *Body size and hip fracture risk in older women: a prospective study.* The American journal of medicine, 1997. **103**(4): p. 274-280.
65. Chen, Z., et al., *Fracture risk among breast cancer survivors: Results from the Women's Health Initiative Observational Study.* Archives of Internal Medicine, 2005. **165**(5): p. 552.
66. Tokumaru, S., et al., *Insufficiency fractures after pelvic radiation therapy for uterine cervical cancer: an analysis of subjects in a prospective multi-institutional trial, and cooperative study of the Japan Radiation Oncology Group (JAROG) and Japanese Radiation Oncology Study Group (JROSG).* Int J Radiat Oncol Biol Phys, 2012. **84**(2): p. e195-200.
67. Hui, S.K., et al., *The Influence of Therapeutic Radiation on the Patterns of Bone Marrow in Ovary-Intact and Ovariectomized Mice.* PLoS One, 2012. **7**(8): p. e42668.
68. Alvarez, R.E. and A. Macovski, *Energy-selective reconstructions in X-ray computerized tomography.* Phys Med Biol, 1976. **21**(5): p. 733-44.
69. Johnson, T.R., et al., *Material differentiation by dual energy CT: initial experience.* European Radiology, 2007. **17**(6): p. 1510-1517.
70. Berger, M.J., et al., *XCOM: Photon cross sections database.* NIST Standard Reference Database, 1998. **8**: p. 87-3597.
71. Photon, E., *Proton and Neutron Interaction Data for Body Tissues.* ICRU Report, 1992. **46**.
72. Liang, K.-Y. and S.L. Zeger, *Longitudinal data analysis using generalized linear models.* Biometrika, 1986. **73**(1): p. 13-22.

73. Boyce, R., et al., *Sequential histomorphometric changes in cancellous bone from ovariohysterectomized dogs.* Journal of Bone and Mineral Research, 1990. **5**(9): p. 947-953.
74. Kugel, H., et al., *Age-and sex-specific differences in the 1H-spectrum of vertebral bone marrow.* Journal of Magnetic Resonance Imaging, 2001. **13**(2): p. 263-268.
75. Reeder, S.B., et al., *Quantitative assessment of liver fat with magnetic resonance imaging and spectroscopy.* Journal of Magnetic Resonance Imaging, 2011. **34**(4): p. 729-749.
76. Banse, X., et al., *Inhomogeneity of human vertebral cancellous bone: systematic density and structure patterns inside the vertebral body.* Bone, 2001. **28**(5): p. 563-71.
77. Wegrzyn, *Role of Trabecular Microarchitecture and Its Heterogeneity Parameters in the Mechanical Behavior of Ex Vivo Human L3 Vertebrae.* Journal of Bone and Mineral Research, 2010. **25**(11): p. 2324-2331.
78. Hayashi, T., et al., *Analysis of bone mineral density distribution at trabecular bones in thoracic and lumbar vertebrae using X-ray CT images.* J Bone Miner Metab, 2011. **29**(2): p. 174-85.
79. Rosen, C.J., et al., *Marrow fat and the bone microenvironment: developmental, functional, and pathological implications.* Crit Rev Eukaryot Gene Expr, 2009. **19**(2): p. 109-24.
80. Engelke, K., et al., *High spatial resolution imaging of bone mineral using computed microtomography. Comparison with microradiography and undecalcified histologic sections.* Invest Radiol, 1993. **28**(4): p. 341-9.
81. Bromley, R.G., et al., *Quantitative histological study of human lumbar vertebrae.* J Gerontol, 1966. **21**(4): p. 537-43.
82. Grote, *Intervertebral Variation in Trabecular Microarchitecture Throughout the Normal Spine in Relation to Age.* Bone, 1995. **16**(3): p. 301-308.
83. Bassett, L.W., et al., *Ischemic necrosis of the femoral head. Correlation of magnetic resonance imaging and histologic sections.* Clin Orthop Relat Res, 1987(223): p. 181-7.
84. Zanetti, M., et al., *Bone marrow edema pattern in osteoarthritic knees: correlation between MR imaging and histologic findings.* Radiology, 2000. **215**(3): p. 835-40.
85. Saadat, E., et al., *Diagnostic performance of in vivo 3-T MRI for articular cartilage abnormalities in human osteoarthritic knees using histology as standard of reference.* Eur Radiol, 2008. **18**(10): p. 2292-302.
86. Bolan, P.J., et al., *Water-fat MRI for assessing changes in bone marrow composition due to radiation and chemotherapy in gynecologic cancer patients.* J Magn Reson Imaging, 2013.
87. Berglund, J. and J. Kullberg, *Three-dimensional water/fat separation and T2* estimation based on whole-image optimization--application in breathhold liver imaging at 1.5 T.* Magn Reson Med, 2012. **67**(6): p. 1684-93.
88. Syed, F.A., et al., *Effects of estrogen therapy on bone marrow adipocytes in postmenopausal osteoporotic women.* Osteoporos Int, 2008. **19**(9): p. 1323-30.
89. Cohen, A., et al., *Abdominal fat is associated with lower bone formation and inferior bone quality in healthy premenopausal women: a transiliac bone biopsy study.* J Clin Endocrinol Metab, 2013. **98**(6): p. 2562-72.

90. Cohen, A., et al., *Increased marrow adiposity in premenopausal women with idiopathic osteoporosis.* J Clin Endocrinol Metab, 2012. **97**(8): p. 2782-91.
91. Thiele, J., et al., *Histomorphometry of bone marrow biopsies in primary osteomyelofibrosis/-sclerosis (agnogenic myeloid metaplasia)--correlations between clinical and morphological features.* Virchows Arch A Pathol Anat Histopathol, 1989. **415**(3): p. 191-202.
92. Yagi, M., et al., *Whole Body Micro-PET/CT System Reveals Functional Heterogeneity and Early Local and Systemic Changes Following Targeted Radiation to the Murine Caudal Skeleton.* Calcif Tissue Int, 2014. **In Press**.
93. Jensen, G.F., C. Christiansen, and I. Transbol, *Fracture frequency and bone preservation in postmenopausal women treated with estrogen.* Obstet Gynecol, 1982. **60**(4): p. 493-6.
94. Baron, J.A., et al., *Basic epidemiology of fractures of the upper and lower limb among Americans over 65 years of age.* Epidemiology, 1996. **7**(6): p. 612-8.
95. Court-Brown, C.M. and B. Caesar, *Epidemiology of adult fractures: A review.* Injury, 2006. **37**(8): p. 691-7.
96. Amin, S., et al., *Trends in fracture incidence: a population-based study over 20 years.* J Bone Miner Res, 2014. **29**(3): p. 581-9.
97. Liney, G.P., et al., *Age, gender, and skeletal variation in bone marrow composition: a preliminary study at 3.0 Tesla.* J Magn Reson Imaging, 2007. **26**(3): p. 787-93.
98. Kuiper, J.W., et al., *Accuracy and the influence of marrow fat on quantitative CT and dual-energy X-ray absorptiometry measurements of the femoral neck in vitro.* Osteoporos Int, 1996. **6**(1): p. 25-30.
99. Yu, E.W., et al., *Simulated increases in body fat and errors in bone mineral density measurements by DXA and QCT.* J Bone Miner Res, 2012. **27**(1): p. 119-24.
100. Liu, X., et al., *Quantitative imaging of element composition and mass fraction using dual-energy CT: three-material decomposition.* Med Phys, 2009. **36**(5): p. 1602-9.
101. Samelson, E.J., et al., *QCT measures of bone strength at the thoracic and lumbar spine: the Framingham Study.* J Bone Miner Res, 2012. **27**(3): p. 654-63.
102. Johnson, T.R., et al., *Material differentiation by dual energy CT: initial experience.* Eur Radiol, 2007. **17**(6): p. 1510-7.
103. Berger, M.J., et al., *XCOM: Photon Cross Section Database.* NIST Standard Reference Database, 1998. **8**: p. 87-3597.
104. Photon, E., *Proton and Neutron Interaction Data for Body Tissues.* IRCU, 1992. **Report 46**.
105. Melton, L.J., 3rd, C.S. Crowson, and W.M. O'Fallon, *Fracture incidence in Olmsted County, Minnesota: comparison of urban with rural rates and changes in urban rates over time.* Osteoporos Int, 1999. **9**(1): p. 29-37.
106. Snyder, B.D., et al., *Role of trabecular morphology in the etiology of age-related vertebral fractures.* Calcif Tissue Int, 1993. **53 Suppl 1**: p. S14-22.
107. Ingalls, N.W., *Observations on bone Weights.* American Journal of Anatomy, 1931. **48**(1): p. 45-98.
108. Amling, M., et al., *Heterogeneity of the skeleton: comparison of the trabecular microarchitecture of the spine, the iliac crest, the femur, and the calcaneus.* J Bone Miner Res, 1996. **11**(1): p. 36-45.

109. Powles, T.J., et al., *Oral clodronate and reduction in loss of bone mineral density in women with operable primary breast cancer.* J Natl Cancer Inst, 1998. **90**(9): p. 704-8.
110. Wei, J.T., et al., *Androgen deprivation therapy for prostate cancer results in significant loss of bone density.* Urology, 1999. **54**(4): p. 607-11.
111. Love, R.R., et al., *Effects of tamoxifen on bone mineral density in postmenopausal women with breast cancer.* N Engl J Med, 1992. **326**(13): p. 852-6.
112. Yeh, B.M., et al., *Dual-energy and low-kVp CT in the abdomen.* AJR Am J Roentgenol, 2009. **193**(1): p. 47-54.
113. Kerl, J.M., et al., *Dose levels at coronary CT angiography--a comparison of Dual Energy-, Dual Source- and 16-slice CT.* Eur Radiol, 2011. **21**(3): p. 530-7.
114. Noh, J., J.A. Fessler, and P.E. Kinahan, *Statistical sinogram restoration in dual-energy CT for PET attenuation correction.* IEEE Trans Med Imaging, 2009. **28**(11): p. 1688-702.
115. Arentsen, L., et al., *Multimodality Imaging to measure and map Treatment Effect on Marrow Fat Distribution and it's relation with BMD: Results of a Pilot Study in cancer Survivors*, in *American Society for Bone and Mineral Research*2013, Journal of Bone and Mineral Research: Baltimore, Maryland USA.
116. Hui, S.K., et al., *The Influence of Therapeutic Radiation on the Patterns of Bone Remodeling in Ovary-Intact and Ovariectomized Mice.* Calcified Tissue International, 2013: p. 1-13.
117. Frost, M.L., et al., *Differences in regional bone perfusion and turnover between lumbar spine and distal humerus:< sup> 18</sup> F-fluoride PET study of treatment-naïve and treated postmenopausal women.* Bone, 2009. **45**(5): p. 942-948.
118. Hui, S.K., et al., *Longitudinal assessment of bone loss from diagnostic computed tomography scans in gynecologic cancer patients treated with chemotherapy and radiation.* American Journal of Obstetrics and Gynecology, 2010. **203**(4): p. 353.e1-e7.
119. Chityala, R., et al., *Segmentation and Visualization of a Large, High-Resolution Micro-CT Data of Mice.* Journal of Digital Imaging, 2013: p. 1-7.
120. Huchet, A., et al., *Plasma Flt-3 ligand concentration correlated with radiation-induced bone marrow damage during local fractionated radiotherapy.* International Journal of Radiation Oncology* Biology* Physics, 2003. **57**(2): p. 508-515.
121. Nielsen, O.S., A. Munro, and I. Tannock, *Bone metastases: pathophysiology and management policy.* Journal of Clinical Oncology, 1991. **9**(3): p. 509-524.
122. Bianco, P., *Minireview: The Stem Cell Next Door: Skeletal and Hematopoietic Stem Cell "Niches" in Bone.* Endocrinology, 2011. **152**(8): p. 2957-2962.
123. Fowler, J., *Development of radiobiology for oncology-a personal view.* Physics in Medicine and Biology, 2006. **51**(13): p. R263-R286.
124. Higashi, T., et al., *Evaluation of the early effect of local irradiation on normal rodent bone marrow metabolism using FDG: preclinical PET studies.* Journal of Nuclear Medicine, 2000. **41**(12): p. 2026-2035.
125. Czernin, J., N. Satyamurthy, and C. Schiepers, *Molecular Mechanisms of Bone 18F-NaF Deposition.* Journal of Nuclear Medicine, 2010. **51**(12): p. 1826.
126. Wu, H.-M., et al., *In vivo quantitation of glucose metabolism in mice using small-animal PET and a microfluidic device.* Journal of Nuclear Medicine, 2007. **48**(5): p. 837-845.

127. Hawkins, R.A., et al., *Evaluation of the skeletal kinetics of fluorine-18-fluoride ion with PET.* Journal of Nuclear Medicine, 1992. **33**(5): p. 633-642.
128. Ritman, E.L., et al., *Micro-CT imaging of structure-to-function relationship of bone microstructure and associated vascular involvement.* Technology and Health Care, 1998. **6**(5): p. 403-412.
129. Turner, C.H., et al., *Variation in bone biomechanical properties, microstructure, and density in BXH recombinant inbred mice.* Journal of Bone and Mineral Research, 2001. **16**(2): p. 206-213.
130. Poncin, G., et al., *Characterization of spontaneous bone marrow recovery after sublethal total body irradiation: importance of the osteoblastic/adipocytic balance.* PloS one, 2012. **7**(2): p. e30818.

7. APPENDIX

7.1. Further investigation into functional heterogeneity using Dual Isotope micro-PET/CT

The following sections describe a study that can be used as a future direction of skeletal heterogeneity in terms of the bone mineral matrix, marrow composition, and the balance of bone remodeling. The structural changes, such as those seen in the micro-CT studies above, reflect functional changes that can be measured through functional imaging (e.g. PET).

Skeletal damage and response to treatments are regionally variable [12, 117, 118], however, published reports have investigated only specific bone regions and fail to take a comprehensive approach. Our recent mouse micro-computed tomography (micro-CT) study revealed the potential for anatomical heterogeneity in the whole skeleton [119]. Other non-invasive options for hematopoietic and skeletal assessment include measuring plasma concentrations of Flt-3 ligand [120] and ^{45}Ca assays for bone remodeling [116]. However, these methods only provide a measure of global damage. Characterization of regional marrow and bone metabolism are required to understand local and global tissue environments and treatment responses with emphasis on regions at risk for the development of metastatic disease and pathologic fractures [121].

Advancing the care of cancer patients requires the development and validation of appropriate experimental systems to ensure that animal studies accurately simulate clinical applications of radiotherapy based on radiobiologically relevant dose selection

[67, 116]. Monitoring the local and systemic changes in bone remodeling and skeletal damage resulting from local radiation will be beneficial for optimizing potential interventions proceeding cancer therapy. Furthermore, a recent study strongly supports bidirectional co-regulation of marrow and bone at the microenvironment level [122]. Thus, a comprehensive approach to understanding the integrated response of both marrow and bone tissue to radiation damage is necessary. Taking advantage of novel non-invasive micro-CT guided micro-positron emission tomography (PET) in a hybrid system and dual tracers (^{18}F labeled fluoro-2-deoxy-2-D-glucose (FDG), ^{18}F labeled sodium fluoride (NaF)), we investigated functional heterogeneity of the whole skeleton and then examined the early effects of a clinically relevant local radiation application on local and systemic marrow and bone in an *in vivo* longitudinal study.

7.2. Methods and Materials

Six 16 week-old healthy BALB/c female mice (19.7±1.8 g, Harlan Sprague Dawley, Inc., Madison, WI, USA) were used for this study. All rodents were kept in a standard vivarium and were fed regular mouse diet and water ad libitum. All mice were fasted for at least 1.5 hours before isotope injection.

The XRad 320 Biological Irradiator (Precision X-Ray, Inc., North Branford, CT, USA) was used for all irradiation procedures. Under anesthesia (IP injection with ketamine/xynazine cocktail), a specially designed lead shield (4 mm thickness) was placed over the body, to limit exposure to only the hind limbs (Figure 7-1A). Total dose

delivered(16 Gy single fraction) and skeletal volume irradiated were equivalent to pelvic irradiation based on normalized total dose (NTD) [123] as previously described by Hui et al with details of verifications [67, 116].

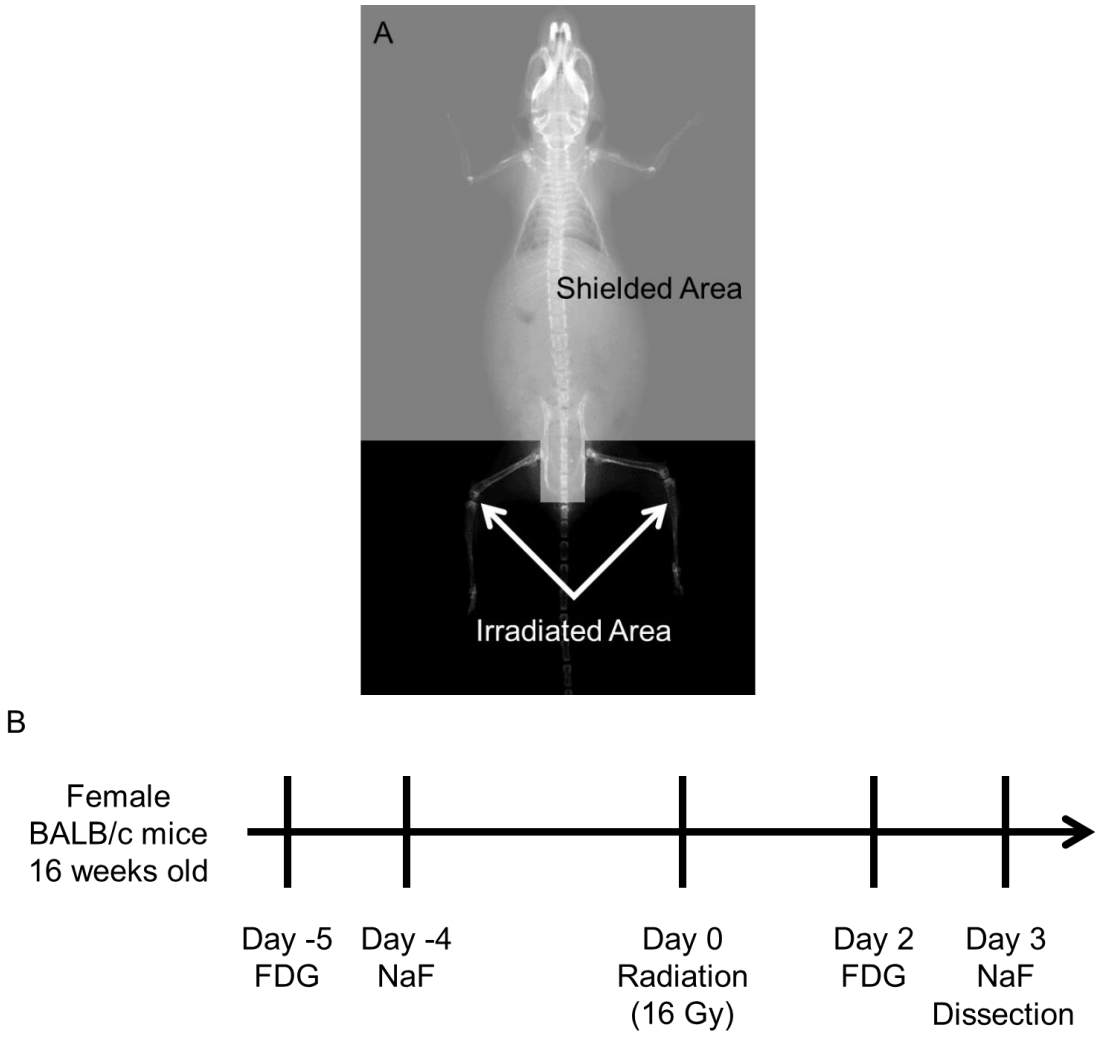

Figure 7-1 (A) Shielding designed to deliver radiation to the hind limbs. (B) Schematic of the experimental design. Micro-PET/CT acquisition was performed serially with FDG and NaF before and after the radiation to the same mice. Mice were dissected on day 3 after the radiation.

PET acquisition was performed serially on days -5 and +2 with FDG for marrow metabolism [124] and days -4 and +3 with NaF for bone metabolism [125] relative to radiation treatment in the same mice (B). The Inveon^{TM} (Siemens Medical Solutions, Knoxville, TN, USA) was used to scan the region from skull to tibia. The isotopes were injected intravenously via the tail vein. The mean dose of FDG and NaF in 100 µl solution were 18.9±1.6 and 18.8±2.7 MBq, respectively, and measured with an Atomlab 100 (Biodex Medical, Shirley, NY, USA), that had been cross-calibrated with the scanner. The scan (list-mode data acquisition) was started at 30 minutes post-injection under anesthesia using the manufacture's recommended acquisition settings. For scanning, anesthesia was maintained at 1.5-3% isoflurane in 1 l/min O_2 via nose cone. During the scan, the mouse was monitored with a dedicated respiration monitor (BioVet, Spin Systems Pty Ltd., Brisbane, Australia). A dedicated warming pad and infrared thermometer were also used to maintain body temperature. Legs were taped to minimize the movement.

The bone VOIs (volume of interest) were first drawn on the CT image and later exported to the PET image. VOIs were identified semi-automatically using the segmentation feature based on a 3D region-growing algorithm and manual modification to minimize variations. There are eight regions; skull, mandible, humerus, cervical spine, thoracic spine (5th-10th), lumbar spine (1st-3rd), femur and tibia (40 slices from knee joint). The activity concentrations in the PET image and blood activity concentrations

were corrected for radiotracer decay (109.77 minutes) back to the tracer injection time. Whole blood and plasma activities approached steady-state at 60 minutes after injection (FDG: [126], NaF: [127]). Thus, whole blood can be used as a surrogate for plasma activity. A recovery coefficient was not applied. The activity ratios of skeletal regions to blood were calculated as bone-to-blood ratios. There is no unit of uptake of tracer because the value is calculated as a ratio of bone uptake activity (kBq/ml) to blood activity (kBq/ml). Heterogeneity described varying uptake distribution of a tracer among skeletal sites in this study.

7.3. Results

Figure 7-2 shows whole body scans of FDG (A and B) and NaF (C and D) uptake before and after radiation, demonstrating functional heterogeneity and radiation effect.

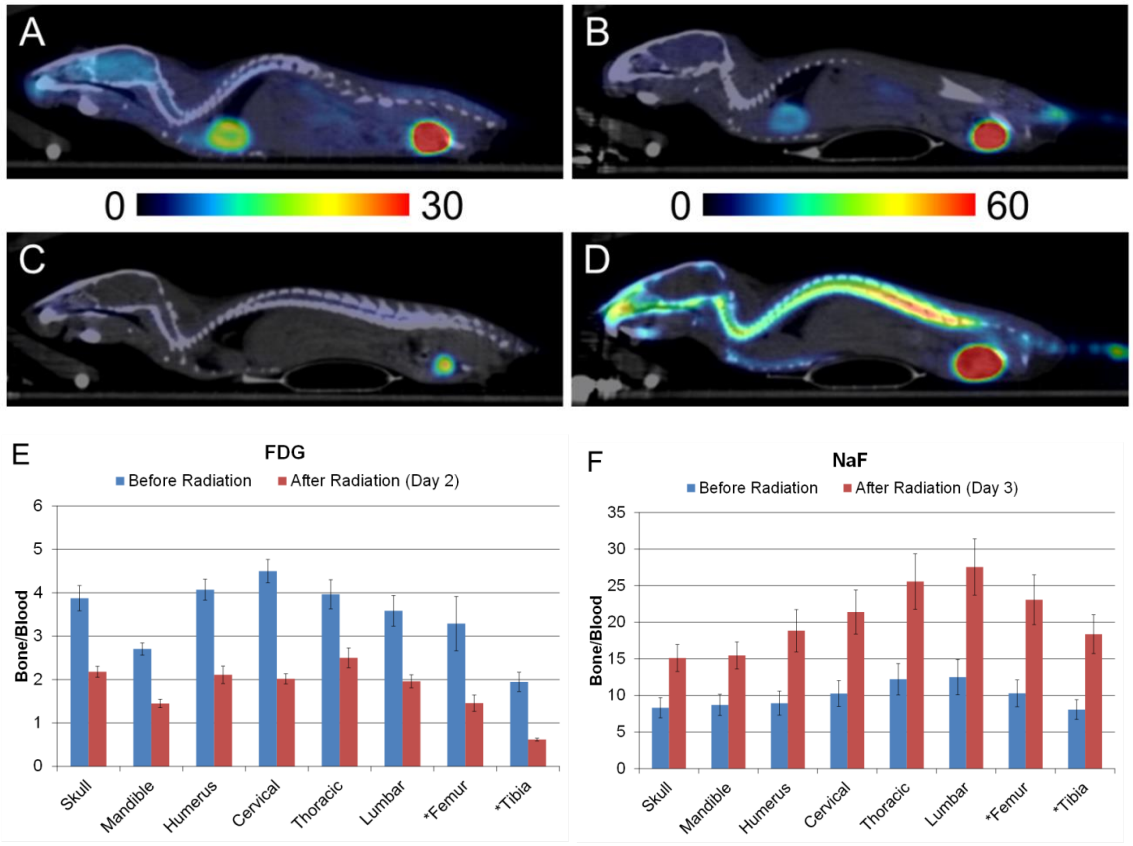

Figure 7-2. FDG uptake before(A) and after radiation(B). NaF uptake before radiation(C) and after radiation(D). Constant maximum and minimum intensities are set in the images for each tracer. (E) FDG uptake before (blue bars, $p<0.0001$) and after (red bars, $p=0.0002$) radiation is significantly different among bone regions. (F) NaF uptake before (blue bars, $p<0.0001$) and after (red bars, $p=0.0003$) radiation is significantly different. Star(*) indicates irradiated bony region.

FDG and NaF uptake are significantly different among bone regions (blue bars in Figure 7-2 E and F, $p<0.0001$ for FDG and NaF). Cervical and lumbar vertebrae had the highest uptake in both FDG and in NaF, respectively. Tibia exhibited the lowest uptake of both.

Radiation exposure to the hind limbs was 16.98±1.58 Gy. Visually, there was differential tracer uptake (Figure 7-2). Quantitatively, the degree of uptake after radiation exposure differed among the regions ($p=0.0002$, Figure 7-2 E). Irradiated region, especially the tibia, demonstrated significantly reduced FDG uptake at 32% of pre-radiation levels. Thoracic vertebrae were higher and tibia was lower compared with an overall average reduction ($p<0.01$, Figure 7-2 E). Figure 7-3 A shows FDG uptake averaged over all bone regions, demonstrating that radiation decreased FDG uptake overall ($p<0.0001$) on day 2 after radiation. Despite individual variability, uptake after radiation was approximately 50% of pre-radiation levels (Figure 7-3 A). Figure 7-3 B shows the difference in FDG uptake of individual mice before and after radiation. All mice show a similar response pattern with high activity in the skull and spine but with large variations (coefficient of variation) between individuals. In contrast, radiation significantly suppressed metabolic activity in the entire skeleton in all subjects with minimal individual variation.

Red bars in Figure 7-2 F show NaF uptake following radiation. In individual mice, the NaF uptake averaged over all regions increased by a factor of 2.2. The degree of uptake after radiation differed among the regions ($p=0.0003$, Figure 7-2). The mandible and skull exhibited less variation from the averaged value ($p<0.01$, Figure 7-2). The lumbar spine and the irradiated regions (i.e. femur and tibia) appeared to have higher variation ($p<0.1$, Figure 7-2). NaF uptake significantly increased among all the regions on

day 3 after radiation (p=0.0314, Figure 7-3 C). Individual variation in NaF uptake was greater than for FDG. Three mice exhibited large increases (>2.0); two mice had moderate increases, and one slightly decreased. The uptake trend was similar before and after radiation (Figure 7-3 D).

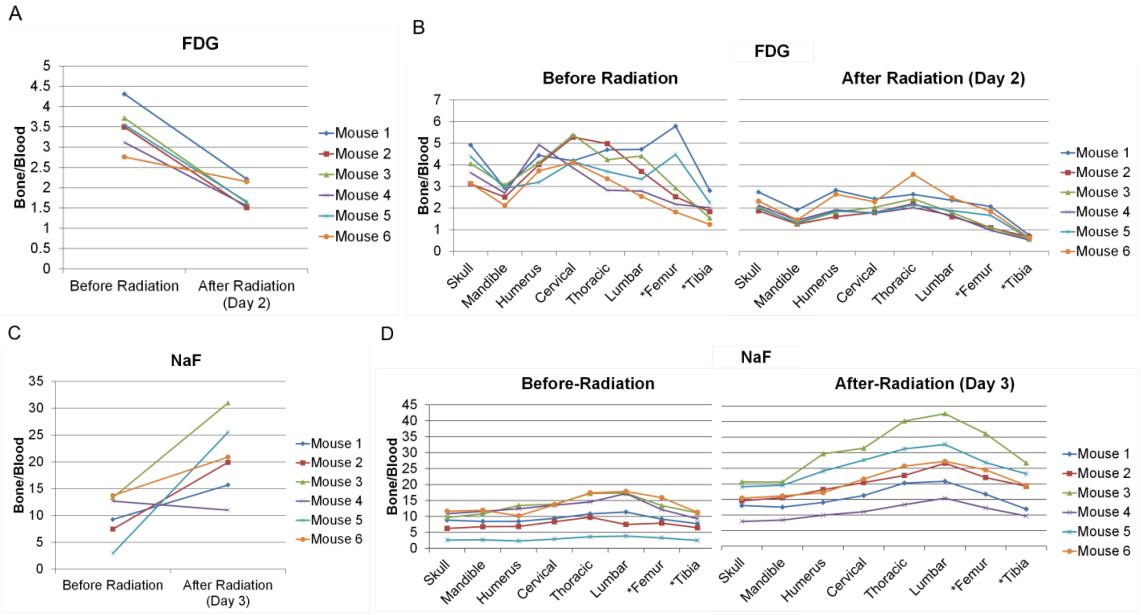

Figure 7-3. Radiation response pattern on individual mouse marrow and bone metabolism. (A) Radiation decreases FDG uptake over all regions (p<0.0001) on day 2 after radiation. (B) FDG uptake before and after radiation among eight different bone regions. (C) Radiation significantly increased NaF uptake among all the regions on day 3 after the radiation (p=0.0314). (D) NaF uptake before and after radiation among the bony regions. Star(*) indicates irradiated bony region.

	FDG			NaF		
Skeletal regions	Ratio before/after (day 2) radiation	95% CI lower	95% CI upper	Ratio before/after (day 3) radiation	95% CI lower	95% CI upper
Skull	0.57	0.44	0.72	1.9‡	1.0	3.6
Mandible	0.53	0.42	0.68	1.9‡	1.0	3.6
Humerus	0.51	0.40	0.65	2.3	1.2	4.3
Cervical	0.45	0.35	0.57	2.2	1.2	4.2
Thoracic	0.63†	0.49	0.80	2.2	1.2	4.2
Lumbar	0.55	0.43	0.71	2.4	1.3	4.5
*Femur	0.46	0.36	0.59	2.4	1.3	4.5
*Tibia	0.32†	0.25	0.42	2.4	1.3	4.5
Overall average	0.50	0.41	0.60	2.2	1.1	4.5
Radiation effect to whole skeleton	< 0.0001			0.0314		
Radiation x skeletal region interaction	0.0002			0.0003		

*Irradiated region.

Model contrasts:

†For FDG, thoracic spine had a higher ratio and tibia had a lower ratio compared to the overall average ($p<0.01$).

‡ For NaF, mandible and skull had a lower ratio compared to the overall average ($p<0.01$).

For NaF, lumbar spine, femur, and tibia had a marginally higher ratio compared to the overall average ($p<0.1$).

Table 7-1. Estimated change due to radiation. FDG averaged over all regions is expected to decrease to 50% of its pre-radiation level. This effect varied by region, and was particularly low for the tibia, where post-radiation FDG was 32% of its pre-radiation level. The NaF level averaged over all regions is expected to increase by a factor of 2.2 following radiation. However, this increase varied by region, from a factor of 1.9 in the skull and mandible to a factor of 2.4 in the femur and tibia. The wide confidence intervals are the result of variable effects seen in different mice (see 7-3 C).

7.4. Discussion

Longitudinal non-invasive functional imaging with dual isotope micro-PET/CT following local irradiation in BALB/c mice revealed regional heterogeneity in marrow and bone metabolic function. Regional changes in marrow metabolic and mineral remodeling with a concurrent abscopal effect early following radiation at a variety of sites were observed longitudinally. This is the first report to characterize functional heterogeneity and changes from medically relevant radiation exposure in the whole skeleton. The application of dual isotope strategies allowed monitoring both local and distant effects on the entire skeleton following targeted radiation, including the simultaneous functional assessment of two distinct but interdependent tissues (i.e. marrow and bone). This technique may permit investigations into the multi factorial communication pathways between the two active tissue components in skeletal metabolism.

Heterogeneity in bone uptake by FDG and NaF indicates functional differentiation among skeletal regions, suggesting metabolic differences at distinct bone sites. This heterogeneity could be due to structural and functional differences [128, 129]. A greater trabecular network and less marrow volume in the spinal bones may lead to greater cross sectional area with a consequently higher metabolic activity. Understanding regional functional differences in the skeleton may therefore be crucial for: a) mapping sections of the skeleton to identify the regions that are most affected by

disease or clinical intervention rather than random selection of skeletal regions to assay, b) beginning to understand the role that local and whole body skeletal environments may play while interacting with systemic endocrine and immune elements, and c) developing treatment plans and evaluating the resulting response to disease management that incorporate factors such as skeletal site and bone marrow composition.

FDG and NaF uptake of the irradiated region were significantly affected by treatment in the current investigation. Radiation decreased FDG uptake, likely indicating decreased bone marrow metabolism since the absolute number of bone marrow cells and their activity may affect FDG uptake [124]. This is in conformity with our previous report of a significant reduction in bone marrow cellularity by day 3 after radiation [67].

Radiation may also lead to long term impairment in skeletal structure and function. Our previously reported study found diminished bone structure in long-term follow up after radiation [116]. Furthermore, there are likely biochemical and physical interactions between the bone surface (namely quiescent osteoblasts) and the adjacent marrow which may influence the radiation effects [130]. Dual isotope micro-PET/CT could be a tool to develop a comprehensive understanding of radiation-induced effects on skeletal metabolism by investigating the temporal (short- and long-term) and spatial (local vs distant) effects of radiation on bone structure and function.

There are challenges to performing longitudinal studies in preclinical model. Repeated scans of the same animal impact anesthetic tolerance. Careful management of anesthetic delivery and plane of anesthesia are essential steps to maintain quality of data integrity. Damage to the tail vein due to repeated injections should be avoided by varying injection sites. Single time point evaluations and radiation doses may have demonstrated a small set of cytokines that are activated after radiation. Further studies with additional time points and radiation doses will clarify the role of other pro- and anti-inflammatory cytokines in skeletal damage.

7.5. Conclusions

Non-invasive longitudinal imaging with dual isotope micro-PET/CT is feasible and allows the investigation of simultaneous changes in marrow and bone metabolic function. This technique may be useful for monitoring local and distal skeletal sites in response to radiation injury. There appears to be some functional skeletal heterogeneity among marrow and bone tissues. We observed temporally-related longitudinal changes in marrow metabolic and mineral remodeling locally and systemically in response to local radiation injury.